X-ray spectroscopy of X-ray binaries

Der Naturwissenschaftlichen Fakultät
der Friedrich-Alexander-Universität
Erlangen-Nürnberg
zur
Erlangung des Doktorgrades

Dr. rer. nat.

vorgelegt von

Ralf Ballhausen

aus Nürnberg

Als Dissertation genehmigt
von der Naturwissenschaftlichen Fakultät
der Friedrich-Alexander-Universität Erlangen-Nürnberg

Tag der mündlichen Prüfung:	9. März 2021
Vorsitzender des Promotionsorgans:	Prof. Dr. Wolfgang Achtziger
Gutachter:	Prof. Dr. Jörn Wilms
	Dr. Randall Smith

Abstract

This thesis describes the spectroscopic analysis of X-ray observations of X-ray binaries, i.e., systems composed of an accreting compact object and a stellar companion. These systems are characterized by their strong gravity, strong magnetic fields, as well as particle and radiation densities. Among the many fascinating physical processes connected to these extreme conditions, I focus on the reprocessing of the continuous X-ray radiation forming in the direct vicinity of the compact source by the circumstellar and circumbinary matter and the diagnostics of this matter by means of X-ray spectroscopy.

After a brief review of accretion processes in X-ray binaries as the original sources of the X-ray radiation, I describe the X-ray observatories used to collect the data analyzed in this work. I give an overview of some of the fundamental processes of matter-radiation interaction, for example absorption and fluorescence by dust grains and neutral and ionized material, that can be used as diagnostic tools in X-ray spectroscopy. The main subject of this thesis is the analysis of observational data of two prominent X-ray binaries, IGR J16318−4848 and Her X-1.

IGR J16318−4848 is one of the most heavily obscured X-ray binaries known to astrophysicists, which makes it an ideal target to study X-ray absorption. However, its absorption column density is so high that many spectroscopic features that are usually employed to infer properties of the absorber are not observable and the X-ray spectrum below 10 keV is completely dominated by a strong Fe K edge and fluorescence complex. Previous observations with *INTEGRAL*, *XMM*-Newton, *Suzaku*, and *Hitomi* have raised questions about the structure and geometry of the absorber, based on constraints on the emission line flux, the line profile, and corresponding ionization states. This thesis describes a simultaneous *XMM*-Newton and *NuSTAR* observation of IGR J16318−4848 that allowed constraints to be placed on the broadband continuum as well as the fluorescence complex. The empirical spectral modeling of these features is in agreement with previous analyses reported in the literature. With the aim of constructing a self-consistent model of the continuum and edge absorption, as well as the fluorescence emission, I compare a photoionized gas absorber built from a large set of `XSTAR` calculations with an olivine dust absorber. Although the nature of the

dust cannot be constrained with CCD-based spectroscopy, the dust absorption model, also supported by previous infrared observations, provides an overall more accurate description of the data. The assumptions of the dust absorption model are validated by Monte Carlo simulations of photon propagation through an olivine absorber, which also clearly indicate a spherical absorber geometry.

The second source considered in this thesis, Her X-1, is one of the best-studied X-ray sources with an almost fifty year long history of X-ray observations and yet, it still remains enigmatic in many aspects of its X-ray binary nature. Its time variability is characterized by three distinct periodicities, associated with the neutron star's rotation, the binary orbit, and a ∼35 day superorbital period of the precessing accretion disk. The warping of the outer rim of the disk, in combination with an almost edge-on perspective, makes this system a unique candidate to study the different zones of the accretion disk, its atmosphere and corona while they pass through the line of sight to the observer. In this thesis, I compare four *XMM*-Newton observations closely monitoring the turn-on phase of the superorbital cycle, i.e., the accretion disk moving out of the line of sight and unveiling the central source. The X-ray continuum is well described by the superposition of three major components, one significantly absorbed by the disk and a second one scattering via the accretion disk corona into the line of sight, but identical in spectral shape to the incident component. A third component is supposed to form in the accretion disk corona itself. The evolution of the X-ray continuum is in agreement with this picture of the opening line of sight as the effective absorption of the direct component decreases gradually and progresses to dominate the total spectrum. The presence of previously observed broad emission features around ∼1 keV and ∼6.5 keV is confirmed; the physical origin of these features is, however, still debated.

The high-resolution RGS spectra show a wealth of absorption and emission lines, among others of He- and H-like nitrogen, oxygen, and neon. All He α triplets are characterized by strong intercombination lines and very weak resonance and forbidden lines. While the ratios of these lines are in general very powerful probes of plasma density and temperature, their quantitative interpretation in Her X-1 is limited by the non-spherical plasma geometry. Line ratios of absorption lines of H-like ions further indicate a complex multi-component plasma or significant ionization gradient. Modeling of the accretion disk, its atmosphere and corona will therefore require careful consideration of geometrical effects and self-consistent treatment of the ionization structure.

Finally, in light of the upcoming launches of the micro-calorimeter missions *XRISM* and *Athena*, future prospects on high-resolution X-ray spectroscopy of X-ray binaries are outlined and put in context with the results about IGR J16318−4848 and Her X-1 obtained thus far.

ZUSAMMENFASSUNG

In dieser Arbeit befasse ich mich mit der spetroskopischen Analyse von Beobachtungen von Röntgendoppelsternen, also Systemen, die aus einem kompakten Objekt bestehen, das Material von einem Begleitstern akkretiert. Diese Systeme zeichnen sich durch ihre starke Gravitation, Magnetfelder sowie Teilchen- und Strahlungsdichten aus. Unter der Vielzahl der faszinierenden physikalischen Prozesse im Zusammenhang mit diesen extremen Bedingungen konzentriere ich mich auf die Reprozessierung der von dem kompakten Objekt ausgehenden, kontinuierlichen Röntgenstrahlung durch das umgebende Material und die Untersuchung dieses Materials mit Hilfe von Röntgenspektroskopie.

Nach einem kurzen Überblick über Akkretion als treibenden Prozess der Röntgenemission in Röntgendoppelsternen beschreibe ich die Röntgenobservatorien die zur Datenaufnahme in dieser Arbeit verwendet wurden. Ich gebe einen Überblick über einige fundamentale Prozesse der Licht-Materie-Wechselwirkung, wie beispielsweise Absorption und Fluoreszenz von Staubkörnern, sowie neutralen und ionisierten Gasen, die mit Hilfe von Röntgenspektroskopie untersucht werden können, um Rückschlüsse über ein astrophysikalisches System zu gewinnen. Der Hauptteil dieser Arbeit widmet sich der Analyse von Beobachtungsdaten der zwei markanten Röntgendoppelsterne IGR J16318−4848 und Her X-1.

IGR J16318−4848 ist eines der am stärksten absorbierten Röntgendoppelsternsysteme die wir kennen. Obwohl diese Voraussetzungen es zu einem idealen Studienobjekt für Röntgenabsorption macht, sind durch seine extreme Absorptionssäulendichte viele spektroskopische Merkmale, die normalerweise häufig für die Untersuchung des absorbierenden Materials herangezogenen werden, in IGR J16318−4848 nicht zugänglich und das Röntenspektrum unterhalb von 10 keV wird vollständig von einer tiefen Fe K-Absoptionskante und einem starken Fe K-Fluoreszenzkomplex dominiert. Frühere Beobachtungen des Emissionslinienflusses, der Linienprofile und des zugehörigen Ionisationszustandes mit *INTEGRAL*, *XMM*-Newton, *Suzaku* und *Hitomi* haben Fragen über die Struktur und Geometrie des Absorbers aufgeworfen. Diese Arbeit beschäftigt sich mit einer simulatenen Beobachtung von IGR J16318−4848 mit *XMM*-Newton und

NuSTAR, mit deren Hilfe sich die Kontinuumsabsorption sowie der Fluoreszenzkomplex genau bestimmen lassen. Die empirische Modellierung der Absorptionskomponenten und Emissionslinien zeichnet ein ähnliches Bild wie frühere in der Literatur beschriebene Analysen. Vor dem Ziel, ein selbstkonsistentes Modell der Kontinuums- sowie Kantenabsorption und Fluoreszenzemission aufzustellen, vergleiche ich einen photoionisierten, gasförmigen Absorber auf der Grundlage von zahlreichen `XSTAR` Simulationen mit einem Olivinstaubabsorber. Obwohl die spektrale Auflösung der CCD-Daten eine Bestimmung der Zusammensetzung und Struktur des Staubes nicht zulässt, liefert das Staubabsorptionsmodell, das auch durch frührere Infrarotbeoachtungen gestützt wird, doch insgesamt eine bessere Beschreibung der Beobachtungsdaten. Die dem Staubmodell zugrunde liegenden Annahmen werden durch Monte-Carlo-Simulationen des Strahlungstransports durch einen Olivinabsorber bestätigt, die zudem deutlich auf eine sphärische Verteilung des absorbierenden Materials um die Röntgenquelle hinweisen.

Her X-1 ist eine der meistuntersuchten Röntgenquellen mit einer fast fünfzigjährigen Beobachtungsgeschichte und doch bleibt sie in vielerlei Hinsicht noch immer rätselhaft. Ihre Zeitvariabilität ist durch drei charakteristische Perioden gekennzeichnet, die jeweils durch die Rotation des Neutronensterns, die Orbitalperiode des Doppelsternsystems und eine circa 35-tägige, superorbitale Präzession der Akkretionsscheibe verursacht werden. Der aufgestülpte äußere Rand der Akkretionsscheibe in Kombination mit einem sehr flachen Blickwinkel auf die Scheibe machen dieses System zu einem ausgezeichneten Kandidaten, um die verschiedenen Zonen der Akkretionsscheibe, ihrer Atmosphäre und Korona zu studieren, während sie sich durch die Sichtlinie des Beobachters bewegen. In dieser Arbeit untersuche ich vier Beobachtungen mit *XMM*-Newton, die den Verlauf des "turn-on" des Superorbitalzyklus abdecken, also des Moments, in dem sich der Rand der Akkretionsscheibe aus der Sichtlinie des Beobachters bewegt und den Blick auf den Neutronenstern freigibt. Das Röntgenkontinuum wird gut durch die Überlagerung drei wesentlicher Komponenten beschrieben. Eine, die durch den Scheibenrand stark absorbiert wird, einer weiteren, die in ihrer spektralen Form identisch zu der einfallenden Komponente ist, jedoch über den Umweg über die Korona der Akkretionsscheibe in die Sichtlinie gestreut wird und eine dritte, die durch Vorgänge in der Korona selbst entsteht. Die zeitliche Entwicklung des Röntgenkontinuums entspricht dem Bild der sich aus der Sichtlinie bewegenden Akkretionsscheibe, in dem die Absorption der direkten Komponente stetig abnimmt, während ihr Beitrag zum Gesamtspektrum immer stärker überwiegt. Zwei breite Emissionskomponenten, eine bei ~1 keV und ~6.5 keV, die schon früher in der Literatur bereichtet werden, werden auch in diesen Spektren beobachtet; ihr physikalischer Ursprung bleibt aber weiterhin Gegenstand zahlreicher Diskussionen.

Die hochaufgelösten RGS Spektren zeigen eine Vielzahl von Absorptions- und Emissionslinien, darunter He- und H-artiger Stickstoff, Sauerstoff und Neon. Die He α-Tripletts all dieser Ionen sind durch starke Interkombinationslinien und sehr schwache

Resonanzlinien, sowie verbotenen Linien gekennzeichnet. Das Verhältnis dieser Linien, das in der Regel Aussagen über die Plasmadichte und -temperatur erlaubt, lässt sich in Her X-1 aufgrund der nicht-sphärischen Plamsageometrie nur sehr eingeschränkt interpretieren. Die Linienverhältnisse von wasserstoffartigen Ionen deuten darüber hinaus auf ein komplexes Multikomponentenplasma, beziehungsweise einen starken Ionisationsgradienten hin. Die Modellierung der Akkretionsscheibe, ihrer Atmosphäre und Korona erfordert daher die Berücksichtiung der speziellen Plasmageometrie, sowie eine selbst-konsistente Behandlung der Ionisationsstruktur.

Vor dem Hintergrund der bevorstehenden Starts der Mikrokalorimetermissionen *XRISM* und *Athena* in den nächsten Jahren gebe ich zum Abschluss einen Ausblick auf zukünftige Möglichkeiten hochaufgelöster Spektroskopie von Röntgendoppelsternen, speziell im Zusammenhang mit den bisherigen Erkenntnissen über IGR J16318−4848 und Her X-1.

Contents

If our eyes were as sensitive to X-rays as they are to light-rays, a discharge-apparatus in operation would appear to us like a light burning in a room moderately filled with tobacco smoke; perhaps the colors of the direct rays and of those coming from the particles of air might be different. The question as to whether the rays emitted by a body which is receiving radiation are of the same kind as those which are incident, or, in other words, whether the cause of these rays is diffuse reflection or a process like fluorescence, I have not yet been able to decide.

— Wilhelm Conrad Röntgen, 1897

1

The Janus face of X-ray absorption

Like so many ground-breaking discoveries, X-ray radiation was discovered by accident. Wilhelm Conrad Röntgen was experimenting with cathode rays when he suddenly observed gleams of fluorescent light on a barium-platino-cyanide screen in his laboratory in Würzburg when the tubes were discharged. His attention immediately focused on these new kind of rays, which he termed X-rays, and he soon discovered their interaction with air and other materials (Röntgen 1895, 1896, 1897).

Over the course of the following years more and more discoveries about the nature of X-rays were made and in the 1920s and 30s, atmospheric gases (N_2, O_2, Ar) were studied extensively regarding their absorptivity for X-rays (see, e.g., Hewlett 1921, Kurtz 1928, Dershem & Schein 1931, Spencer 1931, for just a few selected examples). In 1935, Ernst Müller concluded that *"The detection of [extraterrestrial] radiation of $\lambda > 0.4$ Å should not yet be possible with our current tools. Radiation of $\lambda < 0.4$ Å, however, must be detectable at altitudes reachable with balloons [...]"*[1]. However, it was only about 15 years later that the first detection of X-rays of extraterrestrial origin was possible. These very first experiments were performed with V-2 rockets that had been captured by the Americans at the end of World War II, equipped with Geiger-Müller counters, and launched to the outer layers of the Earth's atmosphere. The successful detection of solar X-rays in 1949[2] and the discovery of the first X-ray source outside the solar

[1] Own translation from original article *Die Schwächung extraterrestrischer Röntgenstrahlen in der Atmosphäre*, Müller 1935.

[2] Experiments to observe solar UV and X-ray emission started already in 1946 (Baum et al. 1946), however, in 1949 X-rays in the 1–8 Å band were detected for the first time. See Friedman (1959) for a review of the early rocket experiments.

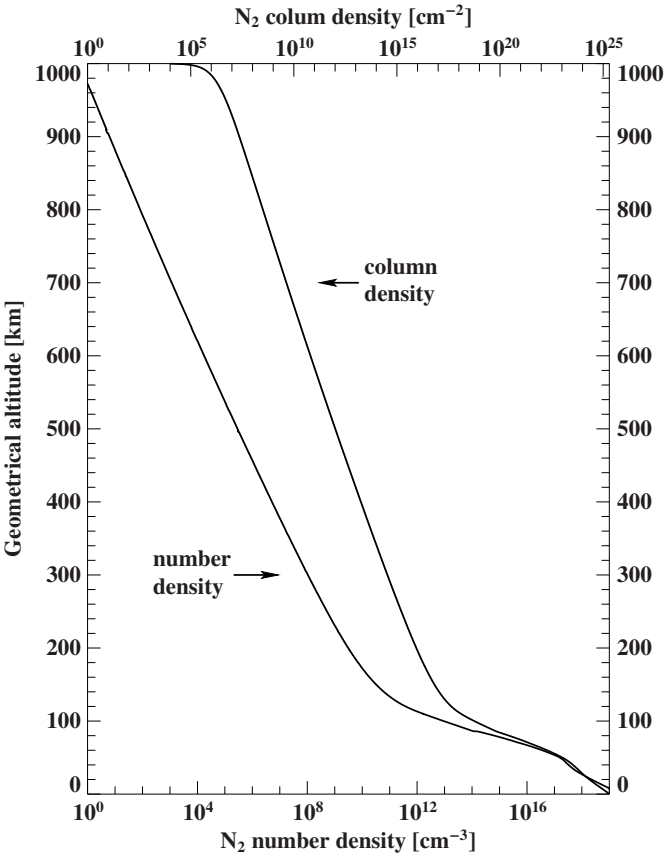

Fig. 1.1: Number density N_{N_2} and column density n_{N_2} of molecular nitrogen for the US Standard Atmosphere 1976 model as a function of altitude Z. Note that N_{N_2} is the column density *above* a given altitude obtained by integrating n_{N_2} from Z to 1000 km (limit of the atmosphere model).

system, Sco X-1 in 1962 (Giacconi et al. 1962), marked the beginning of the new era of X-ray astronomy.

X-ray observations of astrophysical sources are only possible with satellite- or balloon-borne observatories because the Earth's atmosphere is highly opaque to X-rays. Figure 1.1 shows the number density of molecular nitrogen n_{N_2} as a function of altitude and the N_{N_2} column density toward an extraterrestrial source for the US Standard Atmosphere 1976[3]. The column density of N_2 at the ground is $\sim 2 \times 10^{25}$ cm^{-2} and decreases to $\sim 10^{12}$ cm^{-2} at 500 km which is roughly the orbit of *NuSTAR* or *Swift*. Note that while nitrogen is the most abundant element in the Earth's atmosphere, its total X-ray absorptivity is also immensely increased by its other constituents, in particular molecular and atomic (at higher altitudes) oxygen, ozone, and water vapor.

It is also the interaction of X-rays with atoms and molecules, however, that yields the wealth of the diagnostic power of X-ray spectroscopy. A nitrogen atom in the Earth's atmosphere is an obstacle that has to be overcome by launching X-ray observatories to outer space, making them very limited in size and mass, and highly expensive and challenging in construction and operation. On the other hand, the same nitrogen atom in

[3]U.S. Standard Atmosphere, 1976, U.S. Government Printing Office, Washington, D.C., 1976.

a supernova remnant or an accretion disk corona, on the other hand provides valuable information about its environment. The transitions the atom makes upon interaction with incident X-ray photons or ambient electrons tell us about the ionization states, temperatures, and densities of its surroundings.

By means of X-ray spectroscopy, we can study collisional and photoionized plasmas in the vicinity of compact objects like neutron stars or black holes, absorption of X-rays in the Interstellar Medium (ISM), learning as much about the X-ray sources as about the ISM itself. It further allows for studying large structures around X-ray sources like accretion disks or tori in X-ray binaries and Active Galactic Nuclei, or density and temperature structures of hot and cold gas in galaxy clusters. Obviously, X-ray spectroscopy as a field does not only serve its own purposes. The interpretation of astrophysical spectra is closely connected to our understanding of atomic physics, (quantum)-electrodynamics, and chemistry, both in theory and experiment. Naturally, all of these fields provide feedback, tests and, benchmarks to one another.

In this thesis, I focus on X-ray spectroscopy of X-ray binaries, and in particular on the surrounding material giving rise to source-intrinsic absorption and fluorescence. The understanding of this material, its density, ionization state, and composition is closely related to stellar and binary evolution and the dynamics of mass transfer in these systems.

The two individual sources studied here – despite both being X-ray binaries – show quite different behavior in their properties regarding absorption, fluorescence and reprocessing of X-rays in their surroundings. IGR J16318−4848 is an X-ray binary in the Norma arm of our Galaxy that is among the most obscured X-ray binaries we know. X-ray absorption in this source has a two-sided character. The intrinsic absorption is so extreme that the source is basically invisible in X-rays below 4 keV, making several very powerful diagnostic spectral features such as absorption edges of common elements like oxygen or silicon inaccessible. However, the strong obscuration of the source gives rise to very distinctive spectral features that challenge common absorption models. The reward of pushing these models to their limits are strong constraints on the properties of the absorbing material.

The other source is the famous neutron star binary Her X-1. This source is highly variable and some of this variability originates from absorbing material moving in and out of the line of sight. Depending on the time of the observation, we can see the unobscured neutron star or different components of the absorbing material, making Her X-1 an ideal target to study accretion disk absorption, disk coronae, and outflows.

This thesis is structured as follows: Chapter 2 gives a brief overview of general properties of X-ray binaries. Chapter 3 summarizes some basic concepts of X-ray spectroscopy. The main X-ray instruments used in this thesis, *XMM*-Newton and *NuSTAR*, are introduced in Chapter 4. Chapters 5 and 6 present the spectroscopic analysis of IGR J16318−4848 and Her X-1, respectively, and Chapter 7 summarizes the main conclusions and outlines possible future work.

By all its characteristics this model, obtained only from the analysis of the data of observations without any a priori hypothesis about the nature of the source, corresponds to a neutron star in a state of accretion. If the identification of the optical object similar to an old nova with the X-ray source is correct, then the natural and very efficient supply of gas for such a accretion is a stream of gas, which flows from a secondary component of a close binary system toward the primary component which is a neutron star.

— Iosif Samuilovich Shklovsky, 1967

2

X-ray Binaries in a Nutshell

X-ray binaries are some of the most extreme objects in the astronomical sky. In this thesis, the absorbing and fluorescing material in X-ray binaries is studied, thus this chapter will give an introductory overview of their properties. For further reading, a good introduction into compact X-ray sources is given by Tauris & van den Heuvel (2006). An excellent textbook on accretion physics, especially gas dynamics and accretion disks has been published by Frank et al. (2002). Hilditch (2001) is a standard reference for close binary systems, not only specific to X-ray binaries but in particular for orbital motion and related mechanics and mass exchange.

2.1 The first bright X-ray sources

With the discovery of the first bright X-ray sources outside the solar system in the 1960s, quite naturally an active discussion about the origin of the intense X-ray radiation began. Shklovsky (1967) proposed mass accretion in a close binary to be the driving energy source in Sco X-1. Soon after, with the discovery of a periodic variation of the radial velocity of the optical companion in Cyg X-1 (Bolton 1972) and (almost at the same time) of regular eclipses and cyclic variations of the pulse period in Cen X-3 (Schreier et al. 1972b) and SMC X-1 (Schreier et al. 1972a), the binary nature of these sources was unambiguously confirmed.

Stellar binaries, where two stars are gravitationally bound and orbit their common

center of mass have long been known[1]. X-ray binaries, however, are characteristic in the sense that a significant transfer of mass happens between the two components. The *donor*, in most cases a young or evolved main sequence star transfers mass onto the *accretor*, a compact object with a strong gravitational field. As transferred matter falls onto the compact object, potential energy is released and powers the generation of X-ray radiation.

The upper limit of the luminosity that a binary can produce at a certain mass accretion rate is given by the potential power released by the mass transfer. For simplicity this is often approximated by the gravitational potential at the surface (or event horizon in case of black hole) with respect to infinity and referred to as *accretion luminosity*

$$L_{\mathrm{acc}} = \frac{GM_*\dot{M}}{R_*} \,, \tag{2.1}$$

where G is the gravitational constant, M_* and R_* are the mass and radius of the compact object and $\dot{M}$ is the mass accretion rate. The radius of the compact object, R_*, in particular for black holes, leaves some room for interpretation. By characterizing the compact object by its Schwarzschild radius, $r_{\mathrm{g}} = 2GM_*/c^2$, instead of its mass, Eq. 2.1 becomes

$$L_{\mathrm{acc}} = \frac{1}{2}\frac{r_{\mathrm{g}}}{R_*}\dot{M}c^2 = \eta\dot{M}c^2 \,. \tag{2.2}$$

Here, η is the so-called *accretion efficiency*. It expresses which fraction of the rest energy of the accreted material (per time) can be released by the free fall in the gravitational potential. Assuming $R_* = r_{\mathrm{g}}$ for black holes, accretion could be as efficient as $\eta_{\mathrm{max}} = 0.5$. It must be expected, however, that in reality, the emitted luminosity is significantly smaller and rough estimates for η are of the order of 10% for black holes and 15% for neutron stars (Frank et al. 2002). More detailed discussions on the accretion efficiency of black holes, including the effect of black hole spin and observational results, can be found, e.g., Thorne (1974), Gruzinov (1998), and Davis & Laor (2011).

According to Eq. (2.1) the accretion luminosity scales indefinitely with the mass accretion rate. However, the radiation exerts a pressure on the infalling matter that stops the accretion when the radiation force balances the gravitational force. This limit is called *Eddington limit* and the corresponding *Eddington luminosity*, L_{Edd}, for spherical

[1] Visual binary stars have been known at least since the middle of the 17$^{\mathrm{th}}$ century. One of the earliest examples is Mizar (ζ Ursae Majoris) that can be resolved by eye but it was unclear whether its components were bound by gravitation or just coincidentally aligned. Empirical support of the binary nature of stellar systems was the discovery of the periodic eclipses of Algol (β Persei) in 1783 (the variability of this system was already known before, though) and unambiguously confirmed by the calculation of the orbit of ξ Ursae Majoris in 1827, based on periodic variations of the relative distance of its components measured by William Herschel (see, e.g., Niemela 2001 for a brief review and Heintz 1978 for extensive reading).

symmetric accretion of pure, fully ionized hydrogen is

$$L_{\mathrm{Edd}} = \frac{4\pi}{\sigma_{\mathrm{T}}} G M_* m_{\mathrm{p}} = 1.3 \times 10^{38} \left(\frac{M}{M_\odot} \right) \mathrm{erg\,s^{-1}} \,, \tag{2.3}$$

where σ_{T} is the Thomson cross section, G the gravitational constant, M_* the mass of the compact object and m_{p} the proton mass (see, e.g., Frank et al. 2002, for a derivation). The Eddington limit is rather to be interpreted as an order of magnitude estimate than a strict limit. There are several observations of X-ray sources exceeding their Eddington luminosity, often referred to as super-Eddington accretion, which is often an effect of anisotropy induced, for example, by the strong magnetic field of neutron stars on the accretion geometry and photon-electron interactions (see, for example, Sect. 2.3.1).

Today we know that the majority of bright galactic X-ray sources are binary systems. The most common classifications are by mass or spectral type of the optical companion, or the nature of the compact object. The first mostly determines the mass transfer mechanism, the second how the released potential energy is converted into radiation.

2.2 Classification by donor

There is no strict mass limit at which a distinction between low and high mass X-ray binaries is made. Typically, Low Mass X-ray binaries (LMXB) are considered to have donor masses of less than $1 M_\odot$ while High Mass X-ray binaries (HXMB) are those with $>10 M_\odot$ masses. Some authors therefore also speak of intermediate mass binaries for those systems with donor stars of a few solar masses, like, e.g., Her X-1, but these are rather few in number.

2.2.1 Low mass X-ray binaries

In Low Mass X-ray binaries, the mass transfer happens mostly via *Roche lobe* overflow. Roche lobes are the regions around the two objects circumscribed by the gravitational equipotential line of the first Lagrange point L_1 (see Fig. 2.1). If the donor star fills its Roche lobe, matter can flow over into the Roche lobe of the compact object via L_1. This results in a rather steady supply of matter that builds up in an accretion disk around the compact object until its angular momentum is dissipated.

A simple, though very successful model of accretion disks is the *viscous thin disk* or *α-disk* model. It assumes a geometrically thin, optically thick disk in the orbital plane of the binary system. The gas in the disk rotates nearly on Keplerian orbits with orbital velocity

$$\Omega = \left(\frac{GM}{R^3} \right)^{1/2} \,. \tag{2.4}$$

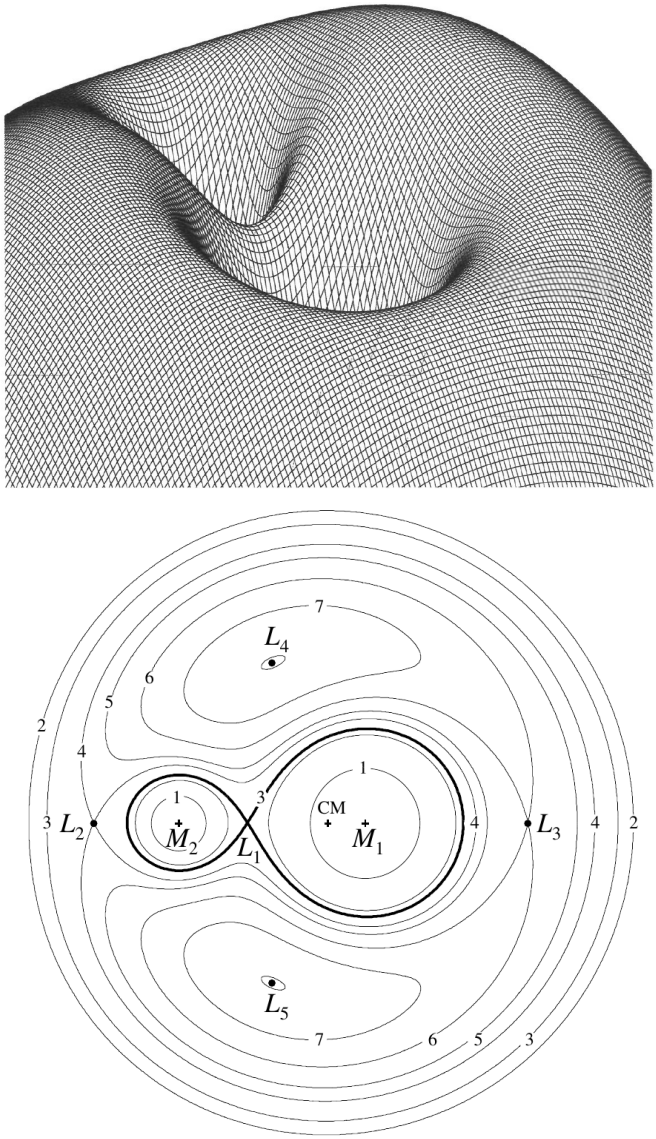

Fig. 2.1: *Top:* Roche potential in the orbital plane of a binary system, illustrating the potential wells of the two objects. The lower potential at large distances from the masses is due to centrifugal forces. Modified from Hilditch (2001). *Bottom:* Orbital plane with equipotential lines for a binary system with mass ratio 4:1. L_1–L_5 mark the Lagrange points and CM the center of mass. The *Roche lobes* are circumscribed by the equipotential line at the level of the L_1, indicated here by the thick black line. Modified from Frank et al. (2002).

Assuming isothermal gas and basically no mass flow in vertical direction gives a hydrostatic density distribution

$$\rho(R, z) = \rho_0(R) \exp\left(-\frac{z^2}{2H^2}\right) , \tag{2.5}$$

with the radial density profile $\rho_0(R)$ at $z = 0$ and the *scale height*

$$H = \frac{c_\mathrm{s}}{\Omega} , \tag{2.6}$$

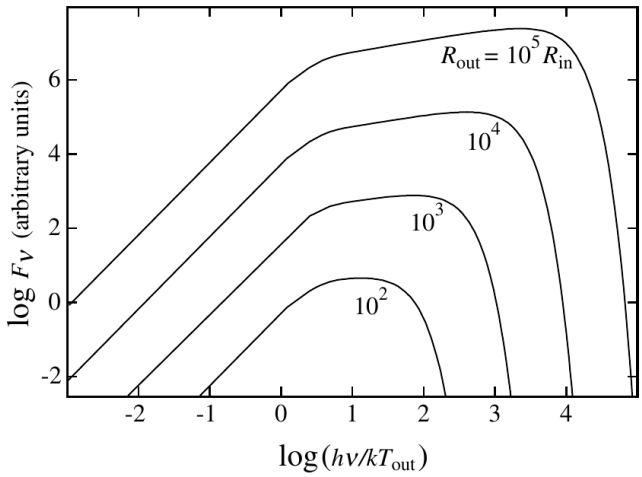

Fig. 2.2: Spectra of a steady, optically thick accretion disk for different ratios of R_{out}/R_{in}. Modified after Frank et al. (2002).

where c_s is the speed of sound. The radial structure of the disk can be determined by solving conservation equations of mass and angular momentum assuming the transport of angular momentum is mediated by viscous torques between adjacent Kepler orbits (see, e.g., Frank et al. 2002). The nature of the viscosity of the gas forming the disk is, however, not yet fully understood (see, e.g., Spruit 2014 for a discussion of some possible mechanisms). A common way to parameterize the uncertainty of the viscous processes is introducing an additional parameter α, originally proposed by Shakura & Sunyaev (1973)

$$\nu = \alpha c_s H \,, \tag{2.7}$$

to scale the maximum viscosity expected from turbulences on length scales of H.

Since the disk is assumed to be optically thick, the radiation emitted from the disk will locally have a blackbody spectrum corresponding to the local temperature $T(R)$. In the case of a steady disk, the temperature profile can be derived by comparing the locally dissipated angular momentum to the Stefan-Boltzmann law and is found to be (e.g., Pringle 1981)

$$T(R) = \left[\frac{3GM\dot{M}}{8\pi R^3 \sigma_{ST}} \left(1 - \sqrt{\frac{R_*}{R}} \right) \right]^{1/4} \,, \tag{2.8}$$

where σ_{st} is the Stefan-Boltzmann constant and R_* is the radius of the compact object. Figure 2.2 shows the total emitted spectra found by integration over the disk radius for different ratios of inner and outer radii.

Introducing additional simplifying assumptions (e.g., the temperature dependence of the mean optical depth) Frank et al. (2002) find the ratio of the disk height to radius at $R \gg R_*$

$$H/R \propto \alpha^{-1/10} R^{1/8} \,. \tag{2.9}$$

One important consequence of the disk widening at outer radii is that it can be illuminated

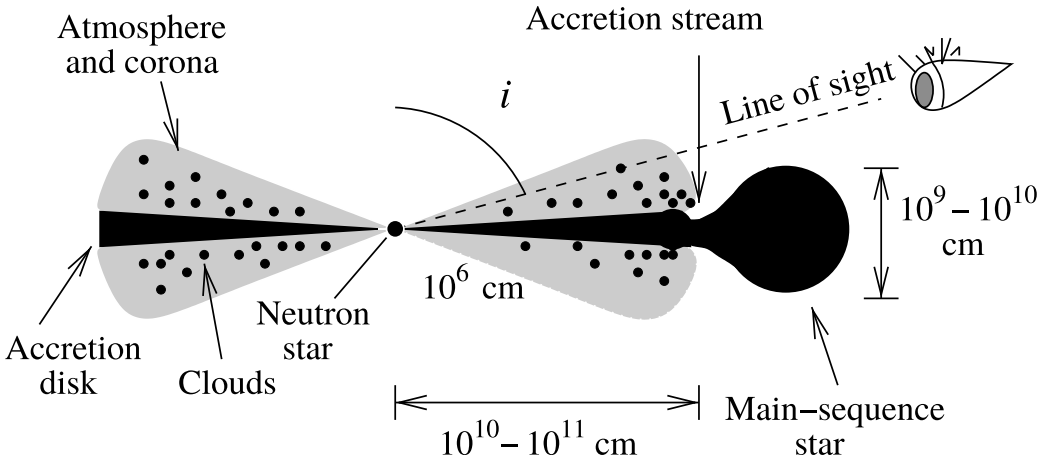

Fig. 2.3: Schematic of an neutron star LMXB system with accretion disk and corona. Modified after Jimenez-Garate et al. (2002b).

efficiently by the central X-ray source. The X-ray irradiation introduces an additional heating term in the thermal balance and can evaporate material from the disk surface which then forms an accretion disk corona (ADC)[2] that is optically thin. This idea was already proposed by Shakura & Sunyaev (1973). First empirical evidence for ADCs came from periodic partial eclipses of the X-ray sources that cannot be explained by obscuration by the companion or its stellar wind (White et al. 1981, White & Holt 1982). Since then, the vertical structure of the accretion disk (which is neglected in the standard thin disk model) and the proprieties of illuminated accretion disk surfaces and coronas has been studied by various authors (e.g., Meyer & Meyer-Hofmeister 1982, Ko & Kallman 1991, Raymond 1993, Ko & Kallman 1994, Jimenez-Garate et al. 2002b). Figure 2.3 shows a schematic illustration of a neutron star LMXB with an accretion disk sandwiched by an accretion disk corona. Observations of spectroscopic signatures of ADCs in both neutron star and black hole binaries like emission lines from a hot, optically thin plasma have for example been reported by Jimenez-Garate et al. (2005), Schulz et al. (2009), and King et al. (2015).

2.2.2 High mass X-ray binaries

In the general picture of High Mass X-ray binaries, the massive, early-type star does not fill its Roche lobe but instead loses mass via its stellar wind. The compact object then accretes from the stellar wind rather than from an accretion disk. The concept

[2]Other possible heating mechanisms like turbulent or convective heating of the ADC are also discussed in the literature, e.g., by Icke (1976).

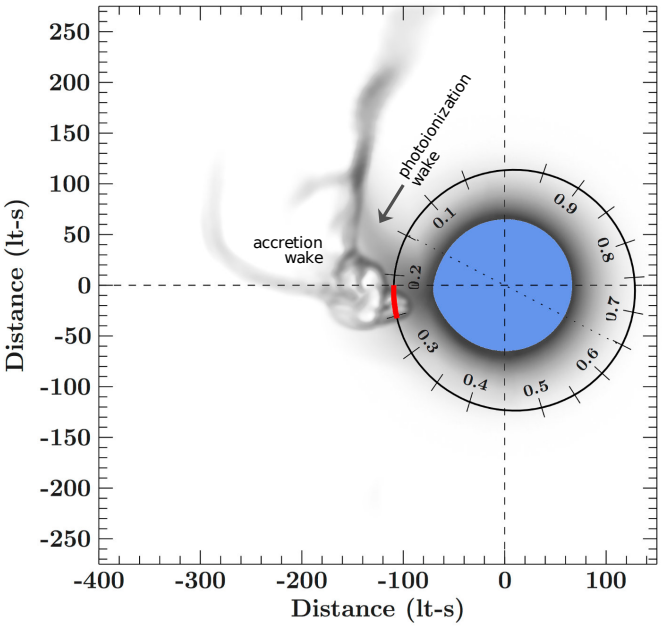

Fig. 2.4: To-scale illustration of the High Mass X-ray binary Vela X-1. The optical companion is shown in blue. The black, solid line indicates the orbit of the neutron star. The background shows an indicative image of the variable large-scale structures that are formed through the interactions of the neutron star with the stellar wind of the mass donor. This image is an artistic impression based on simulations published in Manousakis (2011). Modified after Grinberg et al. (2017).

of quasi-spherical accretion was first studied by Hoyle & Lyttleton (1939) and Bondi & Hoyle (1944), who at that time did not consider X-ray binaries but accretion of the interstellar medium by stars. It can, however, still be a reasonable approximation in some binaries[3] or a starting point to develop more sophisticated models. In general, wind accretion is a highly complex process and constitutes an own field of research, because winds are very often highly inhomogeneous (i.e., 'clumpy'), the mass loss can be variable and the accretion and X-ray emission provide feedback to the system. An illustration of the binary dimensions of the High Mass X-ray binary Vela X-1, together with simulations of the large scale structures of the wind interacting with the neutron star is shown in Fig. 2.4.

Another example of hydrodynamic simulations of the density fluctuations of the wind of a massive star is shown in Fig. 2.5. Observationally, these inhomogeneities of the wind manifest themselves as highly variable absorption columns, multi-phase plasmas and highly variable accretion rates (see, e.g., for some examples Grinberg et al. 2017, Hirsch et al. 2019). A very good review on wind accretion is given by Shakura et al. (2015) and general wind properties of massive stars in binaries are discussed by Martínez-Núñez et al. (2017).

A bit of a special case are Be X-ray binaries (BeXRBs), where the optical companion is a B-type star that is fast rotating and looses mass that accumulates in a circumstellar disk. This disk exhibits strong Hα lines in emission, hence the 'e'. In these systems, the compact object can accrete from the Be disk with an efficiency that is often highly

[3]See, e.g., Edgar (2004) for a review on applications and limitations of Bondi-Hoyle-Lyttleton accretion.

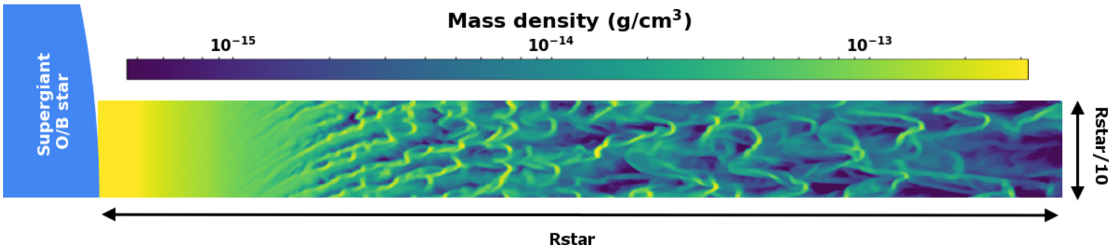

Fig. 2.5: Logarithmic color map of the mass density in the wind at a given time, once the flow has reached a statistically steady state. Modified after El Mellah et al. (2018).

dependent on orbital phase and gives rise to a transient behavior. Comprehensive reviews on BeXRBs are given by Ziolkowski (2002) and Reig (2011).

2.3 Classification by accretor

So far we have looked at a classification of X-ray binaries by the mass of the donor star which affects the type of the mass transfer. Obviously, X-ray binaries can also be distinguished by the nature of the compact object. This will be most crucial once the matter has been gravitationally captured and affects the processes that convert the potential energy into radiation.

2.3.1 Neutron star binaries

Neutron stars are compact remnants of a supernova Type II explosion and consist of nuclear material stabilized by gravity and quantum mechanical degeneracy pressure. Mass estimates roughly range from 1–2 $M_\odot$, although very often the *Chandrasekhar limit* of 1.4 $M_\odot$, the maximum mass that can be stabilized by electron degeneracy pressure, is taken as the canonical neutron star mass. The radius is believed to be of the order of 10–15 km. Although the equation of state of neutron star material is still unknown, the general assumption (also supported by empirical evidence) is that neutron stars have a solid crust and a geometrically very thin layer of atmosphere. Neutron stars have rotation periods of milliseconds up to several minutes.

The processes that lead to the formation of X-ray radiation are now to some extend dependent on the mass accretion rate and the magnetic field of the neutron star. In highly magnetized neutron stars (B~10^{12} G or larger), the accreted material is funneled to the magnetic poles of the neutron star where at sufficiently high mass accretion rates accretion columns form where the matter decelerates and emits Compton-upscattered bremsstrahlung, cyclotron, and blackbody emission (illustrated in Fig. 2.6). The emerging spectra have powerlaw-like shapes with some sort of high-energy cutoff. Additional spectral features which are frequently observed are Cyclotron Resonant Scattering Features (CRSFs or “cyclotron lines”). These originate from the transitions of elec-

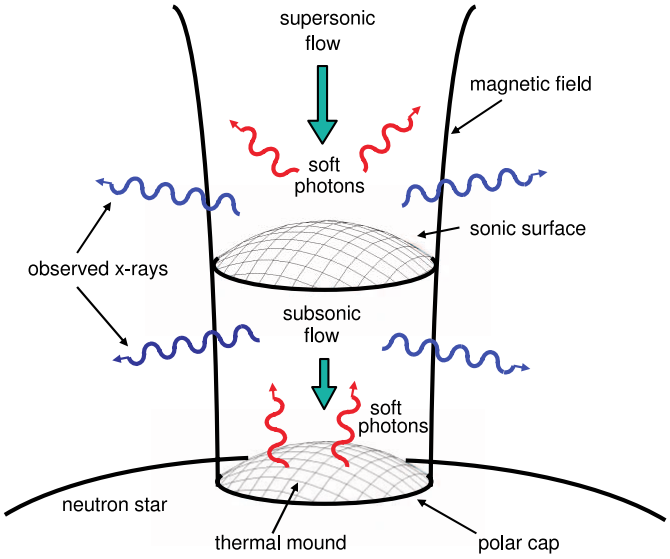

Fig. 2.6: Illustration of matter decelerating to rest in an accretion column. At the bottom a thermal mound forms that emits blackbody radiation. Further sources of radiation are bremsstrahlung and cyclotron emission. This seed radiation is Compton scattered in the hot accretion flow and leaves the column mostly through the side walls. Modified after Becker & Wolff (2007).

trons between so-called Landau levels, i.e., discrete energy states resulting from the quantization of the momenta of the electrons perpendicular to the magnetic field. The hydrodynamical structure of the accretion column and the formation of the X-ray spectrum at all accretion rates is a field of active research. High accretion rates are discussed, e.g., by Basko & Sunyaev (1975), Lyubarskii (1986), Becker & Wolff (2007), Postnov et al. (2015), West et al. (2017a) and West et al. (2017b).

At lower mass accretion rates, the accretion column is expected to shrink down to a thin mound on the polar caps of the neutron star. This process is associated with significant spectral transitions (see Fig. 2.7 and Ballhausen et al. 2017, Tsygankov et al. 2019a,b). The very localized and anisotropic X-ray emission from the columns or the caps gives rise to X-ray pulsations.

In weakly magnetized neutron stars, the accreted matter is not as much directed toward the magnetic poles but instead builds up an atmosphere that is in hydrostatic equilibrium. If the internal energy of this atmosphere exceeds a certain threshold, thermonuclear bursts, so-called "type I bursts", can ignite (see, e.g., Bildsten 2000 for a general review and Galloway et al. 2008 for a comprehensive summary of observational data). In quiescence, crust cooling can be observed mainly as soft, thermal radiation (e.g., Rutledge et al. 1999, Turlione et al. 2015, Wijnands et al. 2017).

2.3.2 Black hole binaries

Black holes do not have a surface that accreted matter can fall onto, heat up, and cool down radiatively. In fact, no information about accreted material can reach the observer once it has passed the event horizon. Yet, black hole binaries are bright X-ray sources and the first confirmed X-ray binary, Cyg X-1, immediately indicated a lower mass of

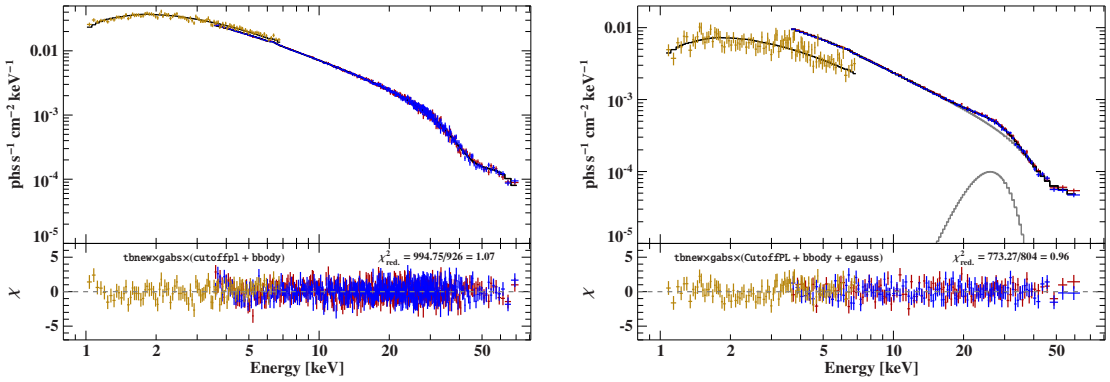

Fig. 2.7: *NuSTAR* (red, blue) and *Swift*/XRT (gold) spectra of the Be/X-ray binary A 0535+26 at $\sim 1.5 \times 10^{36}$ erg s^{-1} (*left*) and $\sim 5 \times 10^{35}$ erg s^{-1} (*right*). During the brighter observation, the spectrum has the exponentially cutoff powerlaw shape observed in many neutron star HMXB and also in this source over several orders of magnitude of luminosity. Toward lower luminosities, a secondary emission feature starts to form. The absorption feature at ~45 keV is a CRSF. Modified after Ballhausen et al. (2017).

the compact object of 3 $M_\odot$ (Bolton 1972), thus ruling out a neutron star system.

The X-ray radiation is originating from the material in the vicinity of the black hole. While the spectral and timing properties of black hole binaries come in very many different flavors, some similarities are frequently observed. The spectrum typically consists of two components: a hard powerlaw-like part and a soft thermal part. Many sources show transitions between states where one of these components clearly dominates the X-ray spectrum. In the *soft* or *high* state (referring to the spectral shape or the source flux, respectively) the corresponding X-ray spectrum is associated with the multi-temperature thermal radiation, especially from the inner region, of the optically thick, geometrically thin accretion disk (Shakura & Sunyaev 1973).

The origin of the powerlaw component that governs the *hard* or *low* state is less well understood. It is generally associated with Comptonization in a hot, optically thin corona (e.g., Shapiro et al. 1976) or relativistic jets; a connection which is also supported by radio observations (e.g., Fender et al. 2004, Wilms et al. 2007, Fender et al. 2009, and references therein). Additionally, a lot of sources show a reflected component of the powerlaw-like incident spectrum off the accretion disk and strong, relativistically broadened iron fluorescence lines (e.g., Fabian et al. 1989, Miller et al. 2004, Blum et al. 2009). Figure 2.8 shows an example spectrum with a reflection hump around ~25 keV.

Over the course of an outburst, many sources show an interesting behavior of these spectral states with luminosity. In so-called hardness intensity diagrams which show the total source flux as a function of spectral hardness, many sources show a characteristic q-shaped track (see Fig. 2.9). The states and transitions are also connected with timing properties, in particular the occurrence of quasi-periodic oscillations (QPOs) which can reach kHz frequencies. A comprehensive review of observational properties of black hole binaries is for example given by Remillard & McClintock (2006).

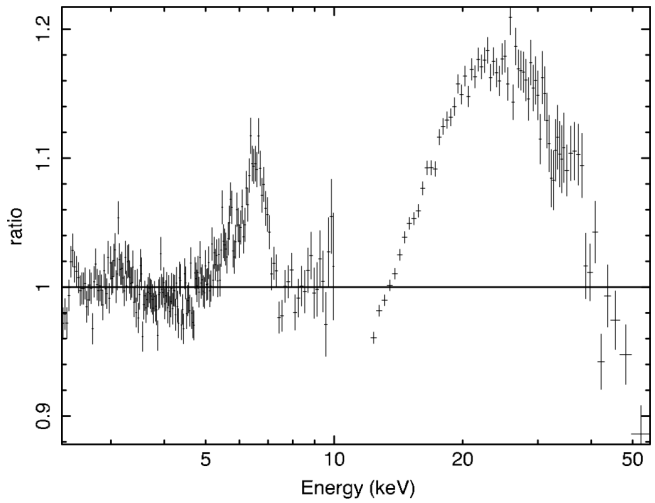

Fig. 2.8: Ratio-residuals of a fit of an absorbed broken powerlaw to the *Suzaku* spectrum of black hole binary GRS 1915+105 with a relativistically broadened iron line around 6.4 keV and a reflection hump around ~25 keV. Modified after Blum et al. (2009).

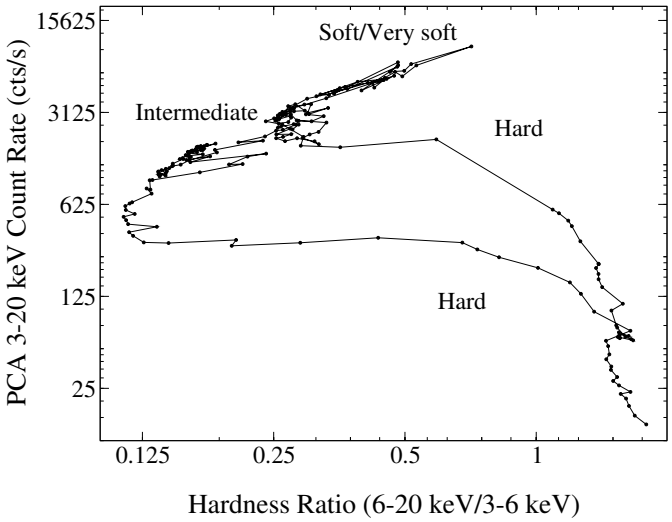

Fig. 2.9: Hardness-intensity diagram of the black hole binary GRO J1655−40 during its 2005 outburst. Modified after Debnath et al. (2008).

The quality of the secondary γ-radiation shows no sudden change from that of the primary. There is simply a gradual softening the more the secondary radiation is deflected from its original direction. The gradual softening is the same for every radiator.

— David C. H. Florance, 1910

3 Some Fundamentals of X-ray Spectroscopy

3.1 Basic photoabsorption and fluorescence

Soon after his discovery of X-rays, Röntgen found that they are absorbed by matter (in his very early experiments he used plates of different metals like aluminum, iron, platinum, and lead) and that hard X-rays are more penetrating than soft X-rays[1], which already allowed for a discrimination of different X-ray energies. The derivation of the absorption law is based on the assumption, that the absorbed intensity in an infinitesimal layer or slice of absorbing material is proportional to the incident intensity

$$\mathrm{d}I = -I\mathrm{d}\tau \,, \tag{3.1}$$

where $\mathrm{d}\tau$ is the infinitesimal *optical depth* of the absorbing medium. Equation (3.1) is easily integrated to the *Beer-Lambert law*

$$I(\tau) = I_0 \exp(-\tau) \,, \tag{3.2}$$

[1] Röntgen himself already used the expressions *soft* and *hard* to characterize X-ray tubes of lower and higher gas pressures which required different voltages to trigger the discharge.

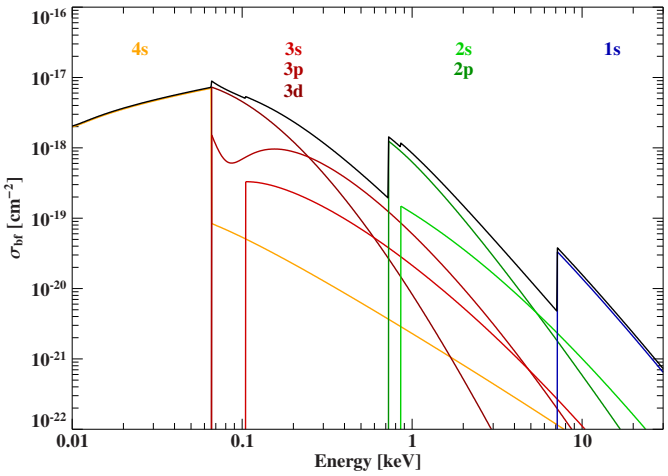

Fig. 3.1: Total (black) and partial (colored) photo-absorption cross sections of iron (Verner & Yakovlev 1995).

with incident intensity I_0. The optical depth is related to the absorption cross section σ and geometry of the absorber:

$$\tau = \int_0^l \mathrm{d}x\, \sigma\, n = \langle\sigma\rangle\, N\,, \tag{3.3}$$

where l is the depth of the absorber along the line of sight, n is the particle volume density. In this simple picture (i.e., ignoring secondary effects like, e.g., heating of the absorber or re-emission of radiation), the distribution of the matter along the line of sight has no effect and is therefore conveniently condensed into a column density, N, with an effective cross section $\langle\sigma\rangle$.

The dominant process of interaction of X-rays with atoms is photoabsorption (also called bound-free absorption), where a photon transfers all its energy to the atom, leading to an excitation or ionization of the atom. While the photoabsorption cross sections for hydrogen like atoms have been calculated analytically already in the beginning of the 20$^{\text{th}}$ century (e.g., Stobbe 1930), multi-electron systems generally require numerical methods. A description of these methods and a compilation of cross sections can be found in, e.g., Verner et al. (1993) and Verner & Yakovlev (1995). For illustration, Fig. 3.1 shows the partial and total photo-absorption cross section for iron for energies from 10 eV to 30 keV. In general, the photoabsorption cross section has approximately an E^{-3} dependence (e.g., Rybicki & Lightman 1986), at least for inner-shell electrons. The *absorption edges* correspond to the sudden onset of absorption by a specific energy level as soon as the photon energy exceeds this level energy.

Figure 3.1 also illustrates nicely that if the photon is above the threshold energy of an absorption edge, photoabsorption will happen predominantly at the corresponding shell. In other words, at for example 10 keV, the partial photo-absorption cross section of the K-shell (1s) is roughly an order of magnitude higher than that of the L-shell (2s and 2p).

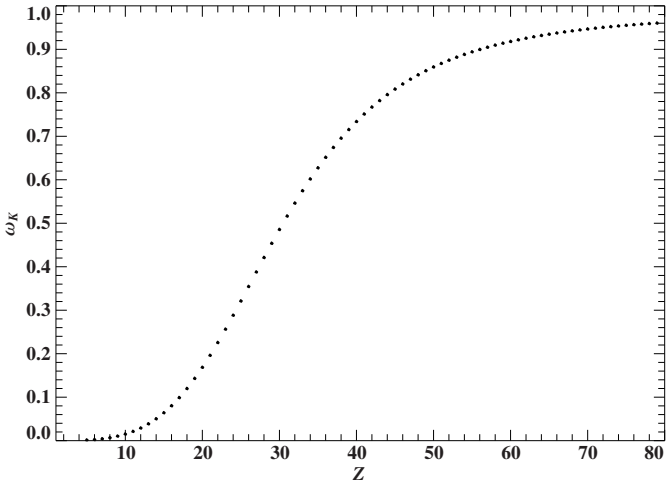

Fig. 3.2: Fluorescence yield ω_K for a K-shell vacancy as function of atomic number Z as described semi-empirically by Eqs. (12) and (14) in Hubbell et al. (1994).

Adopting the notation from Liedahl (1999), the photoionization of an atom A of charge state i can be expressed as

$$A_i + h\nu \rightarrow A_{i+1}^{**} + e \qquad \text{(photoionization)} \; . \tag{3.4}$$

The vacancy in the core shells is then mostly filled by an Auger-Meitner transition (Meitner 1922, Auger 1926, often only called Auger effect), also referred to as autoionization

$$A_{i+1}^{**} \rightarrow A_{i+2}^{*} + e \qquad \text{(autoionization)} \; , \tag{3.5}$$

or radiative de-excitation,

$$A_{i+1}^{**} \rightarrow A_{i+1}^{*} + h\nu' \qquad \text{(fluorescence)} \; , \tag{3.6}$$

the latter giving rise to fluorescence or characteristic secondary radiation. The probability of the radiative de-excitation is expressed in the *fluorescence yield*. A comprehensive review on Auger-Meitner probabilities and fluorescence yields including tabulated values can be found in, e.g., Bambynek et al. (1972) or Hubbell et al. (1994). It is important to note how the fluorescence yield increases with atomic number Z (see Fig. 3.2). For example, the fluorescence yield of silicon is ~4% while that of iron is already ~35%. This is one reason why we observe K-shell fluorescence lines at very different strengths even for elements that have similar abundances.

3.2 Photoabsorption in neutral gas

The careful treatment of X-ray absorption is a crucial part of every single analysis of an X-ray spectrum, either because the physical properties of the absorbing medium are the scientific objective, or because, for example, foreground absorption by the ISM

attenuates the primary spectrum and has to be corrected for before studying the source spectrum. Equations (3.2) and (3.3) determine in principle how absorption acts on a given source spectrum, however, in astrophysical sources a number of difficulties arise. First, the chemical composition of the absorber is not precisely known, so the effective absorption cross section in Eq. (3.3) depends on the assumption of element abundances. Second, while this is an excellent approximation in most cases, the *line of sight* is not a ray in the mathematical sense, but, because of the physical extent of the source and the detector, an extremely small solid angle element that can contain different absorption column densities. For example, this will be the case if an absorber in the vicinity of the source has a density structure (e.g., "clouds") that cannot be resolved but leads to the superposition of differently absorbed source spectra. This phenomenon is commonly known as *partial covering* absorption. Third, there might be secondary contributions to the observed spectrum such as, for example, reflection from a disk that adds spectral features which are very difficult to disentangle from the absorption by transmission, especially given that the true source spectrum is generally unknown.

In most cases, element abundances have to be assumed, at least for the majority of the constituents of the absorbing medium. X-ray data analysis packages such as `xspec`/`isis` or `SPEX` contain pre-defined abundance tables but also allow users to specify their own abundance tables. For a given set of elemental abundances, the effective absorption cross section per hydrogen atom is then given by

$$\sigma_{\rm eff} = \sum_Z A_Z \sigma_Z \,, \tag{3.7}$$

where A_Z is the abundance of element with atomic number Z relative to hydrogen, and σ_Z the corresponding absorption cross section. In X-ray astronomy, the total absorption is then quantified by the equivalent hydrogen column density, i.e., the number of hydrogen atoms per unit area in the line of sight. Figure 3.3 shows the energy dependence of a neutral gas absorber of ISM composition (Wilms et al. 2000) with a hydrogen column density of $N_{\rm H} = 10^{21}\,{\rm cm}^{-2}$.

It is important to note that this number is only meaningful if the assumed element abundances are specified. Figure 3.4 shows how much each element contributes to the total optical depth at 1.0 keV and 6.4 keV, respectively (example calculation, again for abundances of Wilms et al. 2000 and photoabsorption cross sections of Verner et al. 1996). Interestingly, hydrogen, despite its immense abundance, only contributes moderately to X-ray absorption above 1 keV.

3.3 Partial covering

In the case of a structured medium or more complex geometry, different fractions of the X-ray radiation pass through absorbers of different optical depths. This scenario

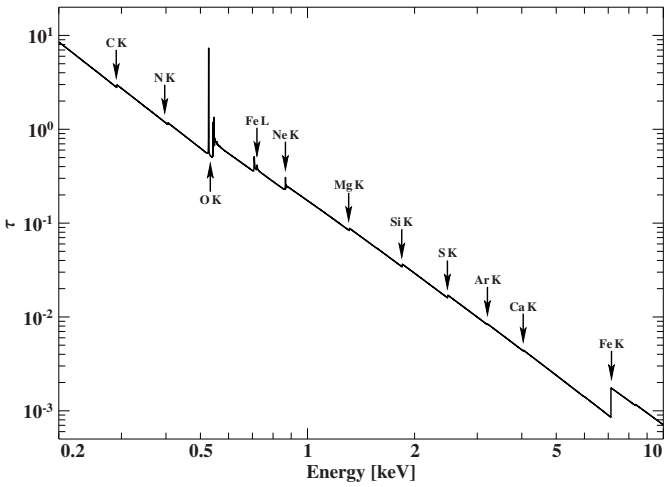

Fig. 3.3: Optical depth τ of an absorber of hydrogen column density of $10^{21}\,\mathrm{cm}^{-2}$ with elemental abundances of Wilms et al. (2000) and cross sections of Verner & Yakovlev (1995) as a function of energy with most prominent absorption edges marked.

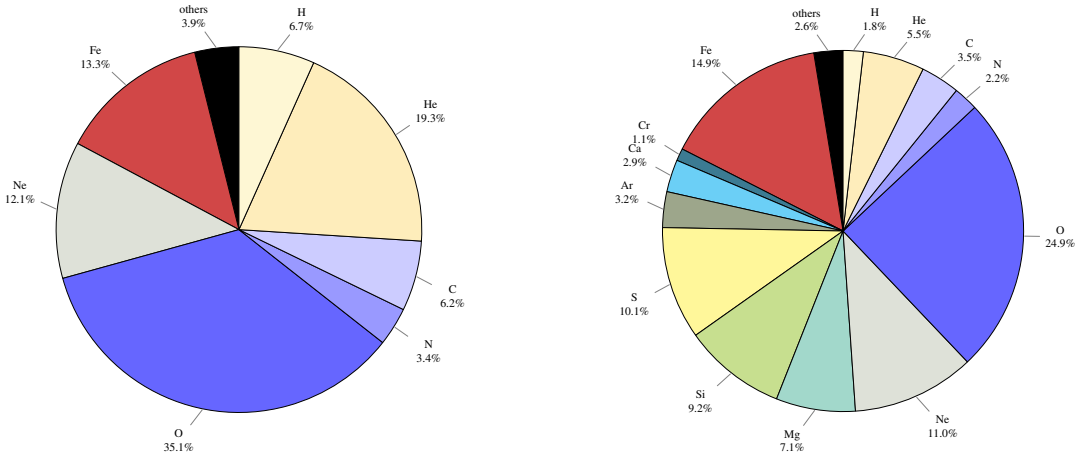

Fig. 3.4: Pie charts of the contribution of elements up to $Z = 30$ to the total optical depth at 1.0 keV (left) and 6.4 keV (right), according to abundances of Wilms et al. (2000) and photoabsorption cross sections of Verner et al. (1996). For display purposes, elements which contribute less than 1% have been subsumed in "others".

is illustrated in Fig. 3.5. While the optical depth is linear in the column density, the absorption is not, so for two absorbers of τ_1 and τ_2 the observed spectrum will be modified as

$$I_{\mathrm{obs}} = I_0 \left[f_{\mathrm{pcf}} \exp(-\tau_1) + \left(1 - f_{\mathrm{pcf}}\right) \exp(-\tau_2) \right] , \tag{3.8}$$

where the covering fraction, f_{pcf}, weighs the individual contributions. This leads to characteristic spectral features like a soft excess or a medium hump, depending on the individual optical depths and the covering fraction. As an example, Fig. 3.6 shows a partially absorbed spectrum with a covering fraction, f_{pcf}, of 0.7, that consists of an absorbed powerlaw with column densities of $10^{22}\,\mathrm{cm}^{-2}$ and $10^{23}\,\mathrm{cm}^{-2}$ (30% and 70%,

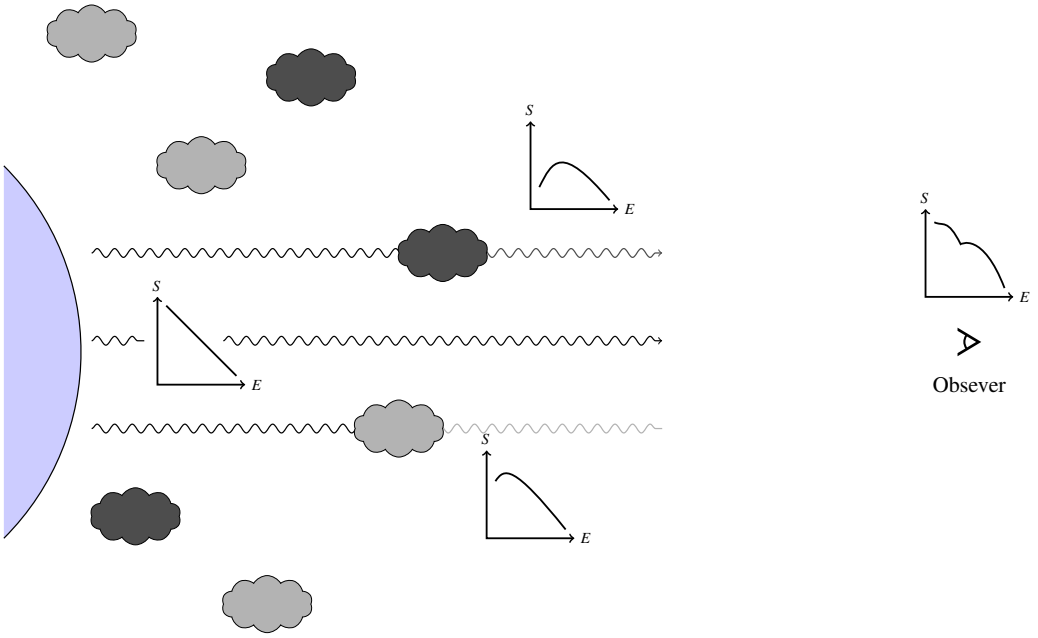

Fig. 3.5: Illustration of a partial covering absorber. The structure of the absorber cannot be resolved by the observer, who instead sees a superposition of differently absorbed spectra. In this schematic example the observed spectrum consists of an unabsorbed, a moderately and a strongly absorbed component.

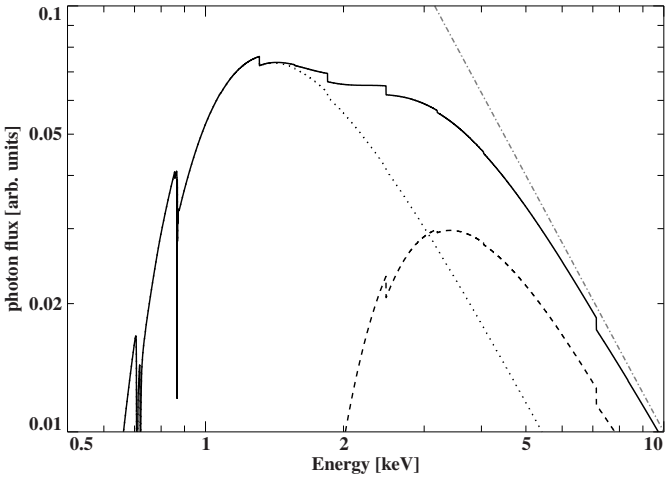

Fig. 3.6: Example of a partially absorbed spectrum with covering fraction, f_{pcf}, of 0.7 (black solid line). The gray, dotted-dashed line shows the incident powerlaw spectrum. The dotted and dashed lines show the absorbed spectrum for hydrogen column densities of $10^{22}\,\mathrm{cm}^{-2}$ and $10^{23}\,\mathrm{cm}^{-2}$, respectively, and abundances of Wilms et al. (2000).

respectively). Many of the previous considerations, and especially Eq. 3.7, only apply to absorption by a neutral, gaseous medium, which is, however, still a fair assumption in most cases.

3.4 Ionized absorbers

In an ionized absorber, the situation becomes much more complex: The incident radiation is absorbed and the deposited energy changes the temperature and ionization state of the absorber. However, the ionization state influences the absorption characteristics of the medium itself. Recombination processes cannot be neglected (otherwise there would be no equilibrium solution until the last atom is ionized) which introduces another source of energy re-distribution.

In particular, the most important physical processes determining the state of the plasma are photoionization and collisional ionization, radiative and dielectronic recombination, charge transfer as well as bremsstrahlung and Compton scattering. Photoionization constitutes the main source of *heating*, i.e., energy is transferred from the photon field to the electron plasma, while recombination, collisional ionization, and bremsstrahlung allow for *cooling* of the plasma. Compton scattering provides in principle a mechanism for both heating and cooling, depending on the energy distribution of the radiation field and the electron temperature, although in most cases of photoionized plasmas, its net effect will be heating of the plasma. Ionization balance requires that for each ion species the rate of ionization equals the rate of recombination while thermal equilibrium requires equal heating and cooling rates for the gas at each point.

The photoionization rate $\alpha_{\mathrm{bf}}^{\mathrm{phot}}$ for a given ion is calculated by integration of the photoionization cross sections for its production over the (local) incident spectrum. Following Halpern & Grindlay (1980),

$$\alpha_{\mathrm{bf}}^{\mathrm{phot}} = \int_{E_{\mathrm{min}}}^{\infty} \sigma_{\mathrm{bf}}^{\mathrm{phot}}(E) \frac{F(E)}{E} \mathrm{d}E \,, \tag{3.9}$$

where σ_{bf} is the bound-free (photoabsorption) cross section and $F(E)$ is the incident spectral energy distribution. Consequently the heating rate is mostly a function of the radiation field.

Radiative recombination, i.e., the capture of a free electron by an ion and radiative release of its binding and kinetic energy is the inverse process of photoionization. The free-bound (radiative recombination) cross section σ_{fb} is connected to the bound-free cross section via the *Milne relation* (Milne 1924)

$$\frac{\sigma_{\mathrm{fb}}}{\sigma_{\mathrm{bf}}} = \frac{g_{\mathrm{b}}}{g_{\mathrm{f}}} \left(\frac{h\nu}{m_{\mathrm{e}} v c} \right)^2 \,, \tag{3.10}$$

which can be derived from detailed balance arguments in thermal equilibrium and where g_{f} and g_{b} are the statistical weights of the free and bound states. The radiative

recombination rate is then

$$\alpha_{\mathrm{fb}}^{\mathrm{rr}} = n_{\mathrm{e}} \int_0^\infty \sigma_{\mathrm{fb}}^{\mathrm{rr}} f(v) v \mathrm{d}v \,, \tag{3.11}$$

where n_{e} is the electron density and $f(v)$ the velocity distribution of the electrons (Mewe 1999).

The collisional excitation and ionization rate is obtained by a similar integration, this time over the velocity distribution,

$$\alpha_{ij}^{\mathrm{coll}} = n_{\mathrm{e}} \int_{v_0}^\infty \sigma_{ij}^{\mathrm{coll}} f(v) v \mathrm{d}v \,, \tag{3.12}$$

with collisional excitation or ionization cross section $\sigma_{ij}^{\mathrm{coll}}$ for transitions $i \rightarrow j$ (Mihalas 1978).

Dielectronic recombination, i.e., the radiationless capture of a free electron and simultaneous excitation of a bound electron, is the most complex process since it involves the change of quantum states of two electrons. Relevant discussions of the calculation of rate coefficients can be found in Shore (1969), Jacobs et al. (1979), and Liedahl (1999).

Finally, Compton scattering and bremsstrahlung do not change the ionization balance but constitute additional heating and cooling processes. The Compton heating rate per electron for an electron plasma with Maxwellian distribution with temperature T_{e} can be described as

$$\Gamma_{\mathrm{e}}^{\mathrm{C}} = \sigma_{\mathrm{T}} \frac{8\pi h}{m_{\mathrm{e}} c^4} \left[h \int_0^\infty \nu^4 \eta(\eta + 1) \mathrm{d}\nu - 4kT_{\mathrm{e}} \int_0^\infty \eta \nu^3 \mathrm{d}\nu \right] , \tag{3.13}$$

with

$$\eta = \frac{c^3}{8\pi h \nu^3} u_\nu \,,$$

where u_ν is the specific energy density of the radiation (Levich & Syunyaev 1971, Halpern & Grindlay 1980). The cooling rate per electron due to bremsstrahlung off an ion with charge Z and number density n_Z is

$$\Gamma_{\mathrm{e}}^{\mathrm{ff}} = \frac{32\pi e^6 Z^2}{3^{3/2} h m c^3} \left(\frac{2\pi k T_{\mathrm{e}}}{m} \right)^{1/2} g_{\mathrm{ff}} n_Z \ \mathrm{erg\,cm^{-3}\,s^{-1}} \,, \tag{3.14}$$

where g_{ff} is the Gaunt factor for free-free emission (Osterbrock 1989).

Note that the heating terms, photoionization and Compton scattering, strongly depend on the incident radiation field, whereas the cooling processes of the plasma are mainly dependent on the electron density and plasma temperature. In thermal equilibrium, the temperature is therefore not a free parameter but forced to fulfill the coupled ionization

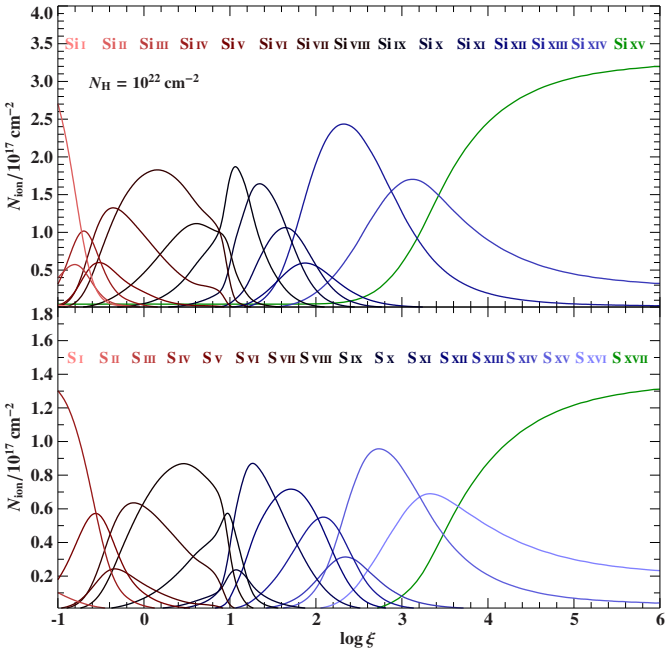

Fig. 3.7: Column densities of individual ionization states of silicon (top) and sulfur (bottom), calculated by the author with `XSTAR` specifically for the incident spectral energy distribution of Cyg X-1, as a function of $\log \xi$. Modified after Hirsch et al. (2019) where also details on the model assumptions are given.

and thermal balance conditions. As an additional consequence, the ionization state of the plasma that depends on the heating and cooling rates, i.e., the incident radiation field and the electron density, becomes a function of the *ionization parameter*

$$\xi = \frac{L}{nR^2} \,, \tag{3.15}$$

where L is the total luminosity, n the particle density and R the distance to the source to scale the geometrical dilution of the incident radiation (Tarter et al. 1969). Solving the coupled rate equations at each location for several thousands of atomic transitions is a very complex problem. In most applications of X-ray spectroscopy it is therefore generally advisable to use either public, pre-calculated photoionization models or apply dedicated software to calculated customized photoionization models rather than attempting to solve the radiative transfer problem in an own implementation. There are of course exceptions to this very general recommendation, for example when a physical process which is normally negligible is explicitly required. Such a case will be discussed in Chapter 5 where Compton scattering off bound electrons is studied quantitatively.

Frequently used public codes to calculate ionization equilibrium for a given plasma under X-ray irradiation are `XSTAR` (Kallman & Bautista 2001) and `CLOUDY` (Ferland et al. 2017) that both have a decade-long history of development and optimization. They allow for the calculation of ion populations and emitted and absorbed spectra. Physical parameters that can be set by the user (although some of them are connected with respect to each other) are the volume and column density, pressure and temperature

of the absorber, its size, the (innermost) ionization parameter, geometry and chemical composition as well as the incident spectral energy distribution. As an example, Fig. 3.7 shows an `XSTAR` calculation of the ion populations of silicon and sulfur as a function of $\log \xi$ for the broadband spectral energy distribution of Cyg X-1 to study the impact of the UV radiation of the optical donor on the ionization structure and to compare the calculated ion fractions against observed equivalent widths of the corresponding absorption lines (see Hirsch et al. 2019 for details).

3.4.1 Pre-calculated photoionization models

The solution of the radiative transfer of the incident radiation in an ionized absorber is in most cases computationally very expensive. On-the-fly calculations of the absorbed and emitted radiation in the course of spectral fitting are therefore hardly feasible. For this reason, several pre-calculated photoionization models exist, for example in tabulated spectra or ion populations for a certain parameter grid that allow for a fast calculation of resulting spectra. These models have the advantage of being very fast and simple to use, but of course have limited flexibility regarding the model assumptions (e.g., the incident spectral shape) and the set and resolution of the parameters.

A few examples of frequently used photoionization models is given below. Neither this list nor the description of the individual models is complete but only intended to give an overview.

`warmabs` and associated models, `photemis`, `windabs`, `multabs`, and `hotabs` are part of the `XSTAR` code distributed with `HEAsoft`. Unlike classical table models, they do not consist of a set of tabulated spectra but contain tables of ion populations that are used to calculate the resulting outcome semi-analytically. The advantage of this approach is that the model is not limited to a specific spectral range and resolution and that changes in elemental abundance can be easily accounted for by scaling the individual element populations. For illustration, Fig. 3.8 shows the optical depth for an absorber of column density of 10^{21} cm^{-2}, so comparable to Fig. 3.3, in the `warmabs` model for different ionization parameters $\log \xi$.

Disadvantages are still the run-time, which is much less of course than for a full calculation of the ionization equilibrium but still larger than for models containing tabulated spectra. The biggest physical limitations are first that population tables represent the ionization balance of an optically thin plasma irradiated with a powerlaw spectrum of photon index $\Gamma = 2$, which is appropriate, for example, for black hole binaries in the soft state but not necessarily for neutron star binaries which tend to have much harder spectra. Applying this model out of the box to sources with very different spectral shape is therefore no longer self-consistent and introduces systematic effects that cannot be easily quantified. The `warmabs` model allows, however, for the usage of user-supplied ion population files which can be calculated for arbitrary incident spectra. Second, the ion populations are always pre-calculated for an optically very thin plasma and later

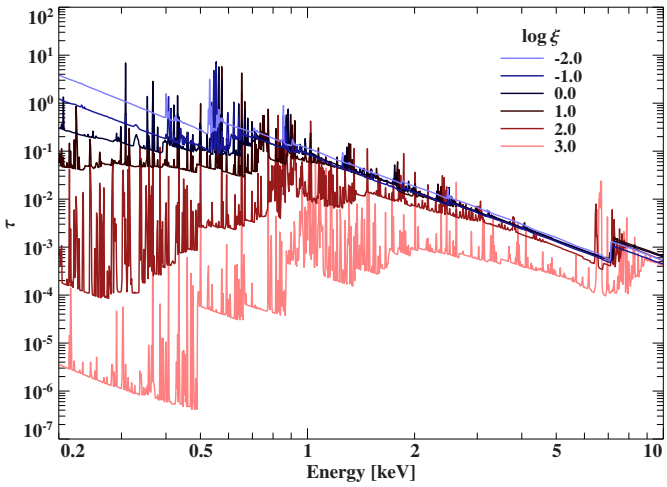

Fig. 3.8: Optical depth τ in the `warmabs` model scaled up to a column density of 10^{21} cm^{-2} and density 10^{12} cm^{-3} for different ionization parameters $\log \xi$.

scaled up to higher column densities. The model therefore assumes a constant ionization parameter along the line of sight. This is not appropriate, however, for large optical depths where a strong gradient of ionization parameter is expected (compare to Fig. 3.9).

Reflection from ionized slab-like absorbers can be modeled, for example with `xillver` (García & Kallman 2010, García et al. 2011, 2013) that also serves as the core of the radiative transfer calculation in the relativistic reflection code `relxill` (Dauser et al. 2010, 2013, García et al. 2014, Dauser et al. 2014). `xillver` also relies on `XSTAR` calculations of ionization equilibrium for an incident powerlaw of photon index $\Gamma = 2$ and a density $n_e = 10^{15}$ cm^{-3}. The `isis`/`xspec` table model `reflionx` (Ross & Fabian 1993, Ross et al. 1999, Ross & Fabian 2005, and references therein) also includes the effect of different incident photon indices on the ionization balance.

3.4.2 Customized photoionization models

Pre-calculated photoionization, while having the great advantage of being user-friendly and rather fast, always come with a set of assumptions that were made during the initial calculation. If these are not valid for a given source, it might be necessary to calculate a photoionization model specifically tailored to its physical properties.

For comparison with the pre-calculated `warmabs` model, Fig. 3.9 shows a full `XSTAR` calculation of the optical depth of an absorbing medium with the composition of the `warmabs` model and irradiated by the same incident powerlaw spectrum used to calculate the `warmabs` ion population files, however, directly for a column density of 10^{21} cm^{-2}. Comparing these optical depths to the corresponding ones of the `warmabs` model (see Fig. 3.8), the average optical depth at the same value of $\log \xi$ in the full photoionization calculation is higher because of the ionization gradient along the line of sight even at moderate column densities. In this particular example of $N_H = 10^{21}$ cm^{-2}, the ionization parameter of 3 at the innermost shell of the spherical absorber decreases to $\log \xi \sim 1.8$

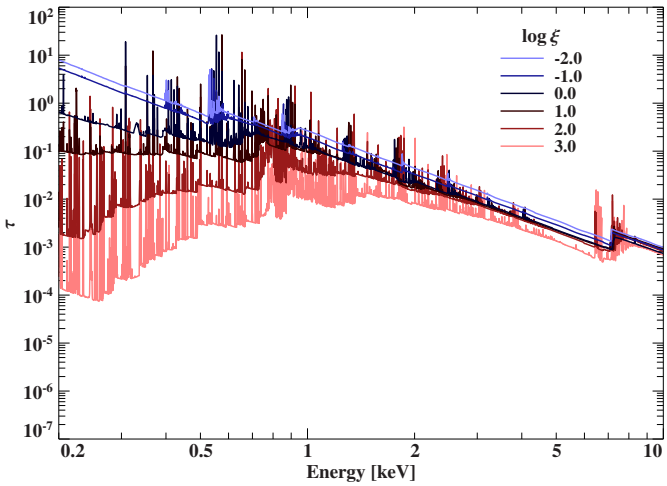

Fig. 3.9: Full XSTAR calculation of the optical depth τ of absorber of composition and incident spectrum of the warmabs for a column density of 10^{21} cm^{-2} for the same ionization parameters $\log \xi$ shown in Fig. 3.8.

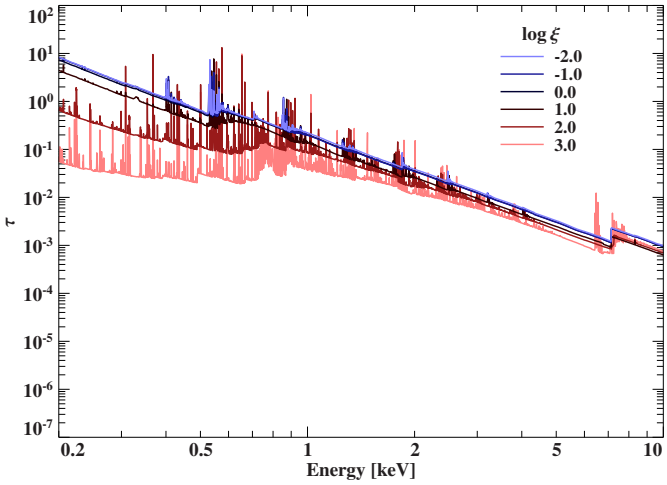

Fig. 3.10: Full XSTAR calculation of the optical depth τ of absorber of column density of 10^{21} cm^{-2} for the same ionization parameters $\log \xi$ shown in Fig. 3.8 but with an incident spectrum more appropriate for an accreting neutron star (see text for details).

along the line of sight with the lower ionized zones contributing more strongly to the optical depth.

For an illustration of the effect of the incident spectral shape, Fig. 3.10 shows an analogue XSTAR calculation as shown in Fig. 3.9 but for an incident spectrum of the form $S(E) = E^{-\Gamma} \times \exp(-E/E_{\rm fold})$ with $\Gamma = 0.5$ and $E_{\rm fold} = 15\,{\rm keV}$ which is more appropriate, e.g., for an accreting neutron star. Since the ionization parameter depends on the integrated luminosity, the main difference in the two calculations is the the amount of soft photons that are mainly responsible for high ionization states of low Z elements. Consequently, the absorber shown in 3.10 has a larger fraction of neutral or lowly ionized atoms which makes the resulting total optical depth larger.

While all these previous considerations strongly argue in favor of calculating a customized photoionization model for every use case, the technical effort is not always worthwhile. The run-time of individual ionization equilibrium calculations is very

dependent on the set of parameters, especially the column density and ionization parameter, but typical values range from several seconds to hours. It is therefore not possible to perform these calculations on-the-fly during a model fit, where a lot of model computations are required by the fit algorithm. One convenient way to speed this up is tabulating the output spectra for a defined grid of model parameters and then interpolating between the tabulated spectra which is very fast. The advantage of this approach is that the computation of the tables can be parallelized for as many cores as available. The most important limitation of table models is, however, the number and step size of the individual parameters, as the number of table entries grows linear with parameter resolution and exponential with number of parameters. Therefore, good rules-of-thumb are to keep the number of independent parameters below four to five, which is generally very few for an advanced, physically motivated model.

3.5 Density and temperature diagnostics with He-like triplets

Among the many possible ionization states of a given atom, those of the isoelectronic sequence of helium have particular diagnostic power regarding electron density and temperature of the surrounding medium. Figure 3.11 shows a simplified Grotrian diagram of the fine structure transitions $1s^2\,{}^1S_0$–$1s2p\,{}^1P_1$ (resonance, r), $1s^2\,{}^1S_0$–$1s2p\,{}^3P_{1,2}$ (intercombination, i), and $1s^2\,{}^1S_0$–$1s2s\,{}^3S_1$ (forbidden, f). Note that the transition $1s^2\,{}^1S_0$–$1s2p\,{}^3P_0$ is strictly forbidden, because both states have zero total angular momentum. The intercombination line therefore splits into only two lines which, however, cannot be resolved in astrophysical X-ray observations with instrumentation currently in operation[2]. An alternative nomenclature that is also frequently used in the literature is w for the resonance line, x and y for the two intercombination lines with upper levels $1s2p\,{}^3P_2$ and $1s2p\,{}^3P_1$, and z for the forbidden line. The first astrophysical observation of the r, i, and f triplet came from the solar corona (e.g., Gabriel & Jordan 1969a,b, 1970) and because of their sensitivity to electron density and temperature, He-like triplets have since then been widely used for plasma diagnostics of coronal plasmas (e.g., Blumenthal et al. 1972, Mewe & Schrijver 1978a,b,c, Winkler et al. 1981, Ness et al. 2002). Porquet & Dubau (2000) refined the diagnostic tools further for investigations of photoionized plasmas. The common way to parameterize the line ratios is

$$R = \frac{f}{i} \tag{3.16}$$

and

$$G = \frac{f+i}{r}\,. \tag{3.17}$$

[2]The splitting of the intercombination line has already been observed with the SXS instrument onboard the *Hitomi* satellite in the Perseus cluster (Hitomi Collaboration 2016).

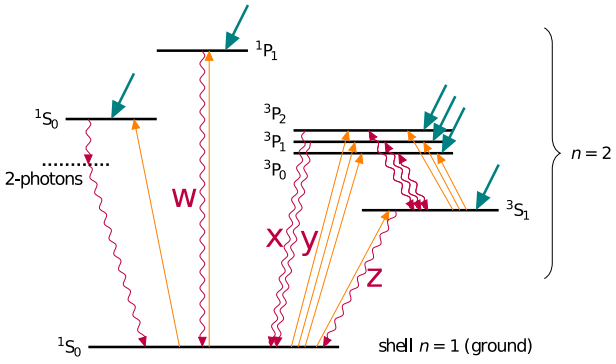

Fig. 3.11: Simplified Grotrian diagram for He-like ions. Orange and red arrows indicate collisional and radiative transitions, respectively. Thick, turquoise arrows indicate both radiative and dielectronic recombination. Modified after Hirsch (2019).

The principle idea behind this He-like triplet diagnostic is the following: The two basic processes that can populate the $n = 2$ states are collisional excitation from the ground state and recombination of an H-like ion. The rates (per ion) to populate the $^1S_0$, $^1P_1$, and $^3S_1$ states depend linearly on the electron density n_e. The $^1P_1$ state de-excites very quickly radiatively via the resonance transition and the $^1S_0$ state via two-photon decay. For the ^3P state, however, an additional population channel exists by collisional excitation from the $^3S_1$ state which has due to the forbidden radiative decay to the ground state a sufficiently long lifetime for further excitation. The important point now is that populating the ^3P state via $^3S_1$ requires either two subsequent collisions or recombination and collision, and hence depends on n_e^2, whereas population via a direct excitation or recombination depends only on n_e. The approximate dependence of R on n_e can therefore be written as

$$R(n_e) \approx \frac{\alpha_f}{\alpha_i + n_e \alpha_f \alpha_{f\to i}} , \tag{3.18}$$

where α_i and α_f are the rates to populate the ^3P and $^3S_1$ states, respectively, and $\alpha_{i\to f}$ is the collisional excitation rate $^3S_1 \to ^3P$. As an example, Fig. 3.12 shows the Mg XI triplet in a coronal plasma of $kT = 20\,\mathrm{keV}$ for two different densities. At higher densities, the $^3S_1$ gets depopulated because of collisional transitions from $^3S_1$ to ^3P that suppress the forbidden line in favor of a strong intercombination line. Note that R has only a weak dependence on temperature.

The ratio G is more sensitive to temperature. At low temperatures typical for example for photoionized plasmas, collisional excitation and dielectronic recombination to the $n = 2$ states are very inefficient because the electrons lack the necessary kinetic energy to excite a transition from the ground state to a higher state. Therefore, the population of these states happens primarily via radiative recombination. In this regime, G varies only mildly with temperature. As soon as the temperature is high enough that dielectronic recombination is possible (i.e., a significant fraction of the electrons have kinetic energies

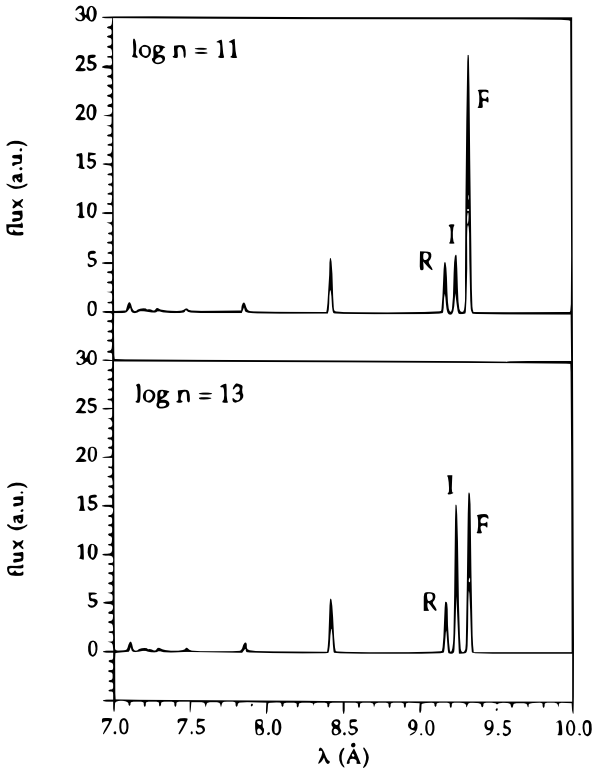

Fig. 3.12: Mg XI triplets at densities of 10^{11} cm^{-3} and 10^{13} cm^{-3} for a recombination dominated plasma with $kT = 20$ keV. Modified after Liedahl (1999).

that in addition to the potential energy of the bound state allows to excite a ground state electron to $n = 2$) dielectronic recombination and collisional excitation will dominate over radiative recombination. Dielectronic recombination and collisional excitation will, however, preferably populate the $^1P_1$ state (the dielectronic recombination rate scales linearly with the oscillator strength of the auto-excited transition, Bates & Dalgarno 1962) and thus result in very strong resonance lines. The temperature-dependence of G is therefore not as continuous as the dependence of R on n_e but rather allows to distinguish between regimes of dominant radiative recombination and dominant dielectronic recombination and collisional excitation. Since this transition happens over a small temperature range, practical temperature diagnostics benefit immensely from the presence of He-like ions of different elements. Figure 3.13 shows the fraction of electrons that can populate the $^1P_1$ via dielectronic recombination for C V, N VI, O VII, Ne IX, Mg XI, and Si XIII as a function of temperature, which can serve as a rough orientation of the temperature range that can be probed with these abundant elements. Around the temperature where a significant fraction of electrons can excite this transition, a strong resonance line is observed and G drops rapidly (compare, for example to Porquet & Dubau 2000, Fig. 7).

Detailed calculations of the density and temperature dependence of R and G of

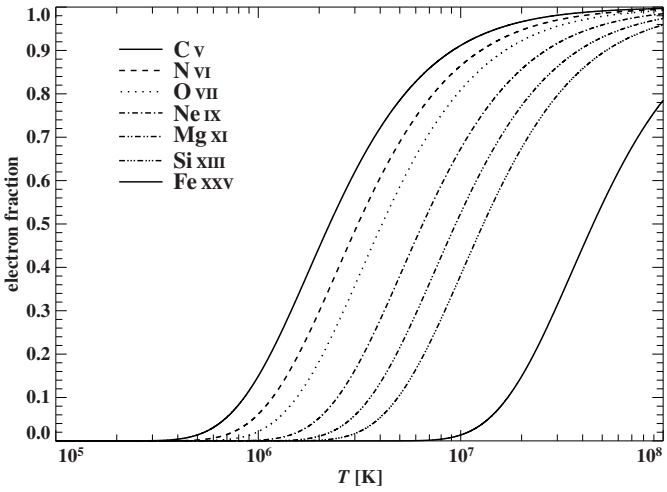

Fig. 3.13: Fraction of electrons with sufficient energy to (auto-)excite the $^1P_1$ by dielectronic recombination for a Maxwellian distribution of temperature T.

photoionized plasmas, also including collisional excitation ("hybrid plasmas") are given by Porquet & Dubau (2000) who also discuss the effect of the He-like versus H-like ion balance on the plasma diagnostic. Extensive tables of R and G for collision-dominated plasmas are given in the supplementary material of Porquet et al. (2001). Non-equilibrium plasmas are discussed, e.g., by Shapiro & Moore (1977), Mewe & Schrijver (1978b), and Liedahl (1999).

3.6 X-ray absorption and self-blanketing in dust grains

So far all considerations assumed that all elements contributing to the absorption of X-rays are in gas phase. We know from different sources of empirical evidence, such as extinction of the light of stars, that this is not the case and that in fact a large fraction of heavy metals is depleted into dust grains (see, e.g., Draine 2003a, for a review). In X-rays, one of the most impressive manifestations of dust is the observation of dust scattering halos around bright sources, i.e., the echo of X-rays scattering off a cloud of dust between the source and the observer. For illustration, one example is shown in Fig. 3.14.

Spectroscopically, dust absorption can be studied by the analysis of the X-ray absorption fine structure (XAFS), i.e., modulations of the absorption cross section just above the absorption edge. These modulations are a result of scattering of the wave function of the photo-electron by the lattice of the surrounding atoms. They are therefore very characteristic for a given chemical composition and crystalline structure of a solid state particle. An extensive review on the theory of XAFS is presented by Rehr & Albers (2000).

XAFS originating from dust absorption can be observed with grating-resolution spectroscopy around absorption edges of typical dust constituents, e.g., silicon or iron. Figure 3.15 shows an example of an observation of the Si K-edge of GX 5−1 with

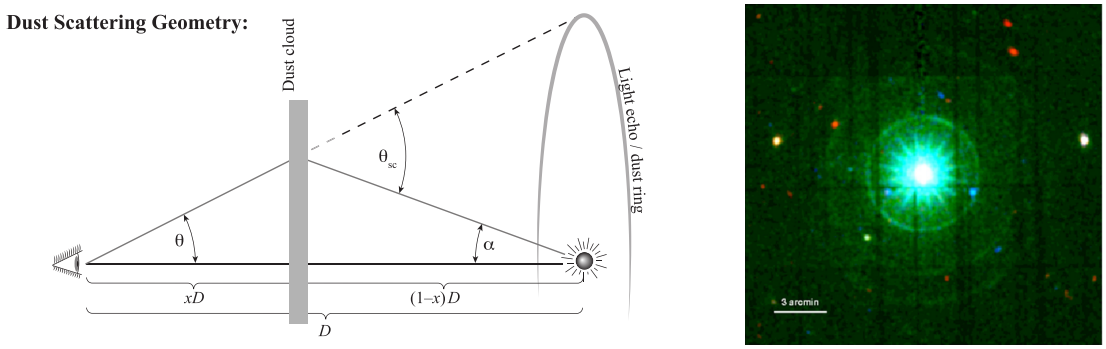

Fig. 3.14: *Left:* Schematic of the dust scattering geometry that gives rise to a halo. X-rays from a source at distance D are scattered off a dust layer at distance xD. The observed angle of the scattered X-rays is θ, while the true scattering angle is $\theta_{\rm SC}$. Modified after Heinz et al. (2016). *Right: XMM*-Newton EPIC-PN image taken after strong bursts of the X-ray pulsar 1E 1547.04−5408. Modified after Tiengo et al. (2010).

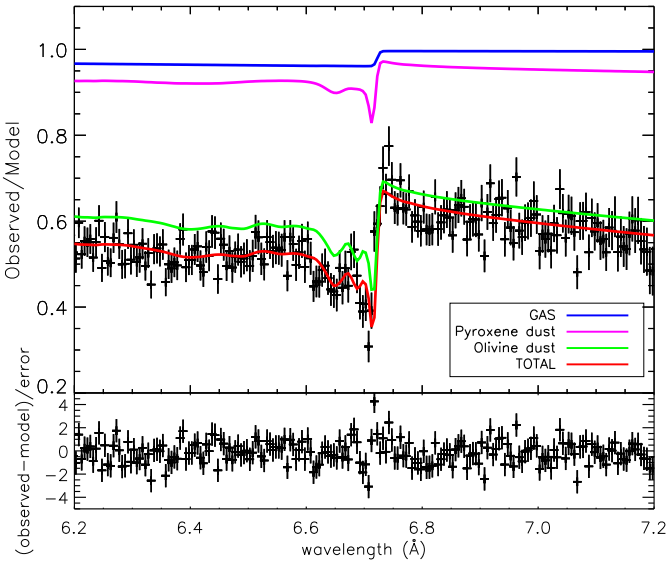

Fig. 3.15: *Chandra* HEG spectrum of GX 5−1 around the Si K-edge, modeled with an absorber with different dust species. Modified after Zeegers et al. (2017).

Chandra HEG with visible XAFS. Other examples of measurements of circumstellar and interstellar dust properties by means of high-resolution X-ray spectroscopy are presented by Costantini et al. (2012), Pinto et al. (2013), and Zeegers et al. (2019).

Another effect that is of particular importance in dust grains regarding the observed optical depth is so-called *self-blanketing* or *self-shielding* (Fireman 1974). It accounts for the fact that the atoms in the center of the dust grain are exposed to less radiation compared to if they were in gas phase. This effect is also illustrated in Fig. 3.16 and could be interpreted as a microscopic realization of partial covering. Both area elements contain the same number of absorbing particles. In the gas phase, the particles are distributed uniformly. In a dust grain, the particles in the interior are shielded in that sense, that all particles absorb the same *fraction* of the incident radiation, but since the

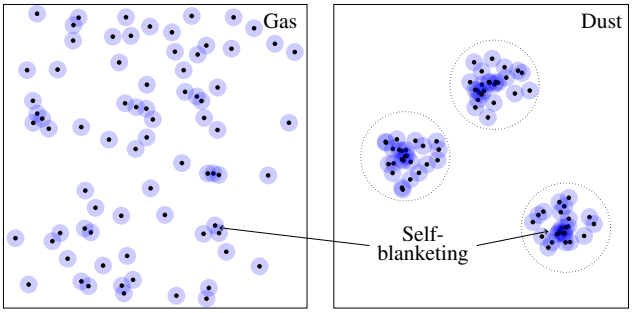

Fig. 3.16: Illustration of the effect of self-blanketing in dust grains. Blue circles indicate the cross sectional area per particle. Both unit areas contain the same number of randomly distributed particles. If the particles are confined in dust grains (dotted circles) the shielding of the particles by each other is higher than in the gas phase.

interior particles see intensity already attenuated by the outer particles, the *total* amount of absorbed intensity, and thus the equivalent optical depth, is lower.

A quantitative description of the self-blanketing factor, f, was already given by Fireman (1974). The following derivation is based on the geometrical considerations by Wilms et al. (2000), with some additional explanations that are omitted in their paper for the sake of conciseness.

In the context of dust grain absorption, the self-blanketing factor is defined as the ratio of the optical depth, τ_{grain}, of an absorber where the absorbing particles are confined in dust grains to the corresponding optical depth, τ_{gas}, of an absorber that has the same number of particles in gas phase. The grains can have arbitrary shapes but have an average column density $\langle N \rangle$ and average photoabsorption cross section $\langle \sigma \rangle$. Wilms et al. (2000) consider spherical grains, but this assumption is not necessary for the derivation of the self-blanketing factor but rather to be consistent with grain size distribution models that are needed to average over different grain sizes.

When the dust absorber has significant optical depth, the latter can be calculated as the sum of infinitesimal absorbers

$$\tau_{\mathrm{grain}} = \int_0^{\tau_{\mathrm{grain}}} \mathrm{d}\tau' \ . \tag{3.19}$$

While the last equation may appear trivial, the idea behind it is that the infinitesimal optical depth can be derived from Eq. (3.1) from the intensity absorbed in the limit of low optical depth.

Wilms et al. (2000) argue that in a dust absorber of (single-sized) grain column density, N_{grain}, geometrical cross-sectional area, σ_{geom}, and an average optical depth $\langle \tau \rangle$ of the grain, the fraction that is removed from the incident radiation is the fraction that hits a grain multiplied by the probability of this radiation getting absorbed.

$$\mathrm{d}\tau_{\mathrm{grain}} \approx \mathrm{d}N_{\mathrm{grain}} \sigma_{\mathrm{geom}} \times \left[1 - \exp\left(-\langle \tau \rangle\right)\right] \ . \tag{3.20}$$

Note that Wilms et al. (2000) carry out the integration in Eq. 3.19 immediately

implicitly assuming a dust absorber of low collective optical depth. There is, however, a subtlety to the border-line treatment of optical depths here. The entire absorber is assumed to be optically thin enough to be approximated by Eq. (3.1). However, the individual dust grains are assumed to have significant optical depth, such that the intensity absorbed by them has to be described by Eq. (3.2). This is obviously contradicting to some degree and therefore only a valid approximation as long as the collective optical depth of the dust absorber is rather low.

Bethell & Bergin (2011) refine the calculation of the self-blanketing factor for strictly spherical dust grains by averaging over the absorbed intensity per dust grain, instead of assuming an average optical depth $\langle\tau\rangle$, but this correction becomes only important for highly opaque dust grains. Bethell & Bergin (2011) evaluate that the difference in the self-blanketing between their calculation and Wilms et al. (2000) is less than 5% for optical depths up to $\tau = 10$.

The optical depth in Eq. (3.20) is now to be compared to the optical depth of a gas absorber that has the same particle column density. The optical depth of the gas τ_{gas} is related to column density of the dust grains $\langle\tau\rangle$ by the geometrical area that the dust grains cover compared to the area element of the gas absorber

$$\tau_{\mathrm{gas}} = N_{\mathrm{grains}} \sigma_{\mathrm{geom}} \langle\tau\rangle \ , \tag{3.21}$$

and therefore the self-blanketing factor

$$f = \frac{\tau_{\mathrm{grain}}}{\tau_{\mathrm{gas}}} = \frac{1 - \exp\left(-\langle\tau\rangle\right)}{\langle\tau\rangle} \ , \tag{3.22}$$

which finally recovers Eq. (A5) from Wilms et al. (2000).

In this general consideration, the grains are solely characterized by their average optical depth $\langle\tau\rangle$. Astrophysical observations, however, rather put constraints on the *grain size distribution* $\mathrm{d}n_{\mathrm{grain}}/\mathrm{d}a$ for radius a (e.g., Mathis et al. 1977, Weingartner & Draine 2001), so a common assumption is spherical grains of constant mass density such that the optical depth $\langle\tau\rangle$ becomes a function of the grain size and the total optical depth of the absorber can be obtained by integration over the grain size distribution.

3.7 Compton scattering

One fundamental interaction between a photon and an electron is the so-called Compton process, named after the American physicist Arthur Holly Compton (1892–1962). While in his original publication, Compton (1923), and in this tradition many standard physics textbooks, refer only to the energy loss of a photon when scattering off a free electron at rest, we will call any incoherent scattering of electrons with photons Compton scattering, regardless of whether the electron is at rest, free, or bound.

The energy transfer has to fulfill relativistic four-momentum conservation, so in the rest frame of the electron, the incident and scattered photon energies, E and E', respectively, are related with the scattering angle θ as

$$\frac{E'}{E} = \frac{1}{1 + \epsilon\,(1 - \cos\theta)}\,, \tag{3.23}$$

where

$$\epsilon = \frac{E}{m_\mathrm{e} c^2}$$

is the incident photon energy in units of the electron rest energy.

Equation 3.23 gives a relation between the energy transfer and the scattering angle. The differential Klein-Nishina cross section (Klein & Nishina 1929)

$$\begin{aligned}\frac{\mathrm{d}\sigma}{\mathrm{d}\Omega} &= \frac{r_\mathrm{e}^2}{2}\left[\left(\frac{E'}{E}\right)^3 + \frac{E'}{E} - \left(\frac{E'}{E'}\right)^2 \sin^2\theta\right] \\ &= \frac{r_\mathrm{e}^2}{2}\left[1 + \epsilon(1 - \cos\theta)\right]^{-2} \times \left[1 + \cos^2\theta + \frac{\epsilon^2(1 - \cos\theta)^2}{1 + \epsilon(1 - \cos\theta)}\right]\,,\end{aligned} \tag{3.24}$$

with the classical electron radius r_e, gives the probability to scatter into the solid angle element $\mathrm{d}\Omega$.

The total Klein-Nishina cross section is obtained by integrating Eq. (3.24) over 4π steradian:

$$\begin{aligned}\sigma_\mathrm{KN} &= \int_0^{2\pi} \mathrm{d}\varphi \int_{-1}^{1} \mathrm{d}(\cos\theta) \frac{\mathrm{d}\sigma}{\mathrm{d}\Omega} \\ &= 2\pi r_\mathrm{e}^2 \left[\frac{1 + \epsilon}{\epsilon^2}\left(\frac{2(1 + \epsilon)}{1 + 2\epsilon} - \frac{\ln(1 + 2\epsilon)}{\epsilon}\right) + \frac{\ln(1 + 2\epsilon)}{2\epsilon} - \frac{1 + 3\epsilon}{(1 + 2\epsilon)^2}\right]\,.\end{aligned} \tag{3.25}$$

Historically, electron-photon scattering was first studied in the framework of classical electrodynamics. The assumption of a pure wave-like nature of light makes the scattering process elastic and the cross section can be derived from a simple dipole oscillator model. The QED treatment of Compton scattering therefore includes Thomson scattering as the limit of vanishing photon mass. The total and differential Thomson cross section is directly derived from Eqs. (3.24) and (3.25) for the limit $\epsilon \to 0$:

$$\frac{\mathrm{d}\sigma_\mathrm{T}}{\mathrm{d}\Omega} = \frac{r_\mathrm{e}^2}{2}\left(1 + \cos^2\theta\right) \tag{3.26}$$

and

$$\sigma_\mathrm{T} = \frac{8\pi}{3} r_\mathrm{e}^2 = 6.653448 \times 10^{-25}\,\mathrm{cm}^2\,. \tag{3.27}$$

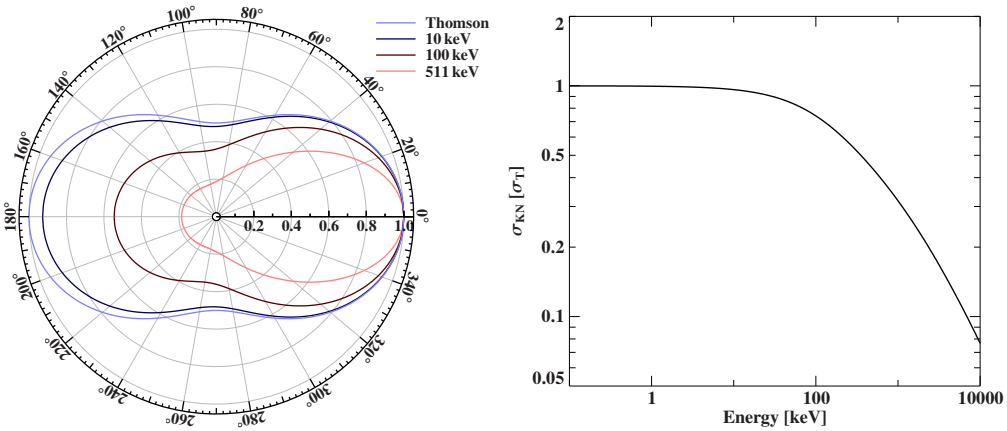

Fig. 3.17: *Left:* Differential Klein-Nishina cross section as defined in Eq. (3.24) for different incident photon energies, normalized to the Thomson cross section for forward scattering ($\theta = 0°$). The light blue line shows the Thomson approximation. *Right:* Total Klein-Nishina cross section in units of the Thomson cross section as a function of energy.

While in reality, electron-photon scattering is always an inelastic process, Thomson scattering is a valid approximation when $E \ll m_e c^2$. Figure 3.17 shows the energy-dependent differential and total Klein-Nishina cross sections for free electron scattering.

3.7.1 Compton scattering off bound electrons

Unlike optical light, coherent scattering of X-rays off electrons bound in atoms cannot be treated in Rayleigh scattering[3] approximation of polarizability of atoms, because the wavelength is of the same order of magnitude as typical atomic radii. Instead, rather than off an individual electron in the atom, the photon scatters coherently off the entire atom and the change in the differential scattering cross section compared to Thomson scattering is accounted for by the *atomic form factor* $F(\mathbf{q}, Z)$. The atomic form factor can be defined as the matrix element (e.g., Nelms & Oppenheim 1955)

$$F(\mathbf{q}, Z) = \sum_{n=1}^{Z} \langle \psi_0 | \exp(i\mathbf{q} \cdot \mathbf{r}_n) | \psi_0^* \rangle \tag{3.28}$$

with the ground state wave function, ψ_0, of an atom of atomic number Z, and the momentum transfer $\mathbf{q}$ of the photon and radius vector $\mathbf{r}_n$ of electron n. A comprehensive description of the scattering channels of hydrogen is given by Sunyaev & Churazov

[3]Some of the literature (e.g., Kane et al. 1986), especially those on detector physics, refer to the coherent scattering of X-ray photons off atoms as Rayleigh scattering if the energy dependence of the cross section is considered but the energy change of the photon is negligible. However, the historical derivation of Rayleigh scattering of optical light leading to the λ^{-4} dependence of the cross section requires λ to be much greater than the particle size.

(1996). Equivalently, the atomic form factor can also be defined as the Fourier transform of the charge density (e.g., Hubbell et al. 1975)

$$F(\mathbf{q}, Z) = \int \rho(\mathbf{r}) \exp(i\mathbf{q} \cdot \mathbf{r}) \mathrm{d}^3\mathbf{r} \,. \tag{3.29}$$

This interpretation is particularly interesting, as the angular distribution of scattered photons allows for the measurement of the spatial electron distribution (see Waseda et al. 2011, for further applications and also a detailed derivation of the atomic form factor).

The modified differential coherent scattering cross section is then given by

$$\frac{\mathrm{d}\sigma_{\mathrm{coh}}}{\mathrm{d}\Omega} = \frac{\mathrm{d}\sigma_{\mathrm{T}}}{\mathrm{d}\Omega} |F(\mathbf{q}, Z)|^2 \,, \tag{3.30}$$

and the total cross section is obtained by integration analogue to Eq. (3.25).

For incoherent scattering, a significant fraction of the photon momentum is transferred to the atom. The related energy transfer is closely connected to the photoionization of neutral gas and plasmas discussed in Sect. 3.2 and 3.4 where those types of interaction were discussed where the photon is destroyed. In an incoherent scattering interaction, the photon survives but leads to an excitation or ionization of the atom. The modification factor, often referred to as *incoherent scattering function* $S(\mathbf{q}, Z)$, is therefore given by the sum of matrix elements of all exciting or ionizing transitions (see, e.g., Hubbell et al. 1975)

$$S(\mathbf{q}, Z) = \sum_E \left| \langle \psi_E | \sum_{n=1}^{Z} \exp(i\mathbf{q} \cdot \mathbf{r_n}) | \psi_0^* \rangle \right|^2 \tag{3.31}$$

It should be noted, that exact, analytic wave functions only exist for hydrogen. The calculation of $F(\mathbf{q}, Z)$ and $S(\mathbf{q}, Z)$ for many-electron systems requires approximations and numerical methods, e.g., Hartree-Fock models. For practical usage, tabulated coherent and incoherent scattering functions for various Z and energies can be found e.g., in Hubbell et al. (1975), Hubbell & Øverbø (1979), Chantler (1995), and Chantler (2000). A recent review on photon cross sections including coherent and incoherent scattering is given by Hubbell (2006). Analogue to Eq. (3.30), the differential cross section for incoherent scattering is given by

$$\frac{\mathrm{d}\sigma_{\mathrm{incoh}}}{\mathrm{d}\Omega} = \frac{\mathrm{d}\sigma_{\mathrm{T}}}{\mathrm{d}\Omega} S(\mathbf{q}, Z) \,. \tag{3.32}$$

Figures 3.18 and 3.19 show the differential and total incoherent scattering cross sections for hydrogen and iron. Incoherent scattering in forward direction is strongly suppressed because the energy transfer is insufficient to excite or ionize the atom.

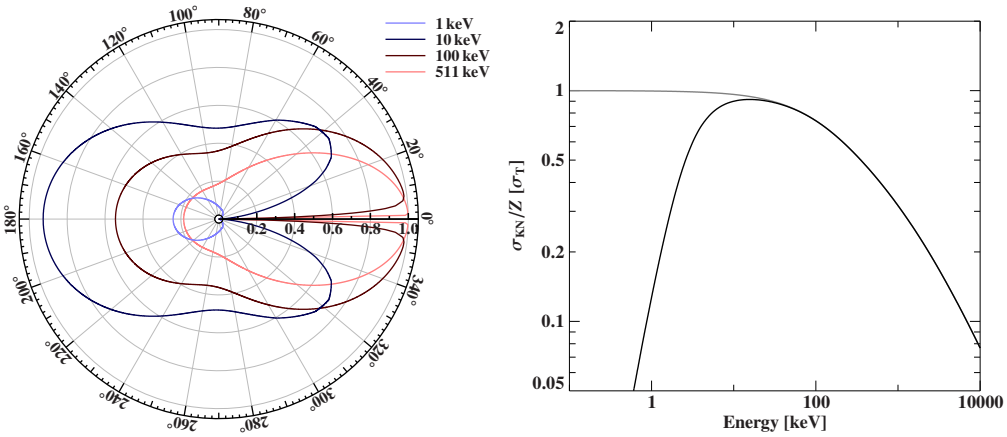

Fig. 3.18: *Left:* Differential Klein-Nishina cross section for hydrogen as defined in Eq. (3.32) with incoherent scattering factors from Hubbell et al. (1975), normalized to the Thomson cross section for forward scattering ($\theta = 0°$). *Right:* Total Klein-Nishina cross section in units of the Thomson cross section per electron as a function of energy (black). The gray line shows the Klein-Nishina cross section for a free electron.

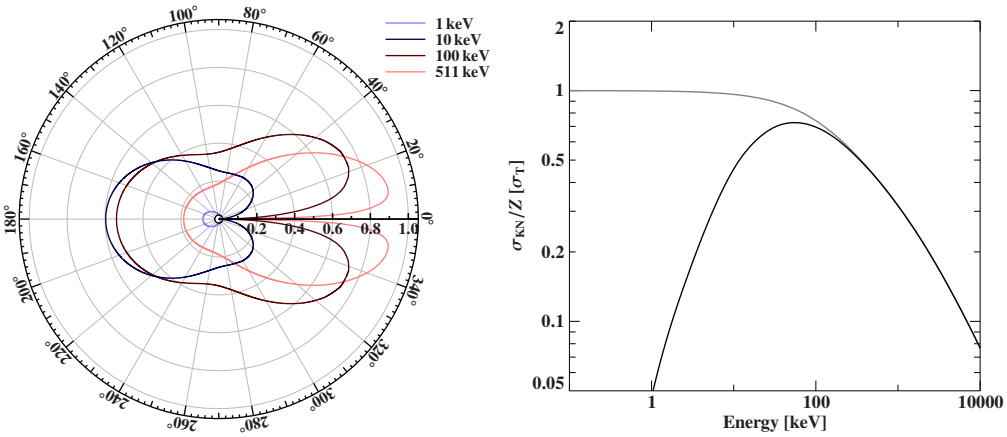

Fig. 3.19: *Left:* Differential Klein-Nishina cross section for iron as defined in Eq. (3.32) with incoherent scattering factors from Hubbell et al. (1975), normalized to the Thomson cross section for forward scattering ($\theta = 0°$). *Right:* Total Klein-Nishina cross section in units of the Thomson cross section per electron as a function of energy (black). The gray line shows the Klein-Nishina cross section for a free electron.

3.7.2 Compton shoulders of spectral lines

Compton scattering is a fundamental radiation process in various astrophysical sources and plays a fundamental role in the formation of hard X-ray continua (for example Sunyaev & Titarchuk 1980 or Titarchuk 1994 for Comptonization in hot plasmas, or Becker & Wolff 2007 for thermal and bulk Comptonization in neutron star accretion columns). What these have in common is the source photons with a continuous energy

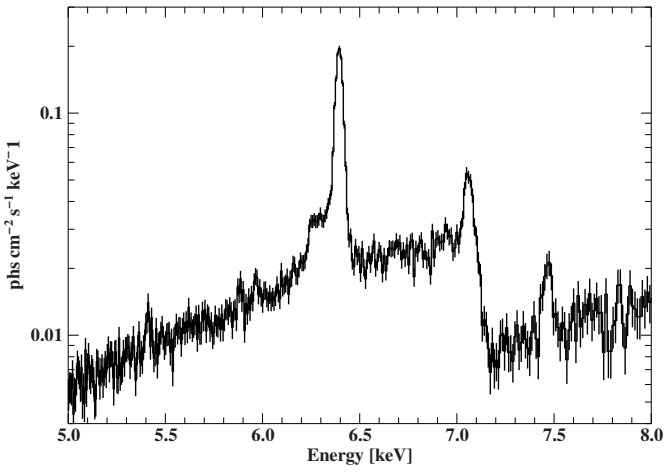

Fig. 3.20: Iron Kα fluorescence line at 6.4 keV with Compton shoulder in GX 301−2 observed with *Chandra* (ObsID 2733). Other characteristic spectral features are the iron Kβ at 7.06 keV, the iron K-shell absorption edge at 7.1 keV and the nickel Kα at 7.5 keV.

distribution (e.g., bremsstrahlung or synchrotron) gain energy in the Compton scattering with hot electrons. Another very characteristic spectral feature that originates from Compton scattering off cold electrons is the so-called *Compton shoulder* of emission lines. Here, quasi-monochromatic radiation from an atomic transition scatters off a cold absorber which leads not only to an attenuation, but also to a deformation of the incident spectral lines. The energy loss that a photon can experience in a single scattering is continuous but limited with the maximum energy transfer for the recoil scattering ($\theta = 180°$) leading to the characteristic shape of the Compton shoulder. Figure 3.20 shows a *Chandra* observation of the HMXB GX 301−2 which exhibits a very strong Compton shoulder on its Fe Kα line. This line allowed Watanabe et al. (2003) to constrain physical properties of the absorber such as electron temperature, column density, and metal abundance. Compton shoulder features are also observed in AGN; one prominent example being the Compton-thick Seyfert II core of the Circinus galaxy (Hikitani et al. 2018).

Monte Carlo simulations of Compton shoulder formation show that the ratio of the Compton shoulder with respect to the primary fluorescence line, as well as the Compton shoulder profile, are important diagnostics to study the absorbing and scattering material. Figure 3.21 shows an example of these simulations of a spherical, cold absorber from Matt (2002). In contrast to the equivalent width of the fluorescence line which is the result of the photoelectric absorption followed by radiative de-excitation, the Compton shoulder is formed from reprocessing of fluorescence photons and is therefore independent of the element abundance and incident spectral shape. Instead, the probability of the fluorescence photons to undergo subsequent Compton scattering mostly scales with the electron density, which is basically equivalent to the hydrogen density. In astrophysical plasmas of solar or ISM abundance, the electron-to-hydrogen ratio is ∼1.2, of which ∼83% come from hydrogen, ∼16% from helium, and less than 1% from metals (example calculation based on abundances from Wilms et al. 2000). The Compton shoulder flux

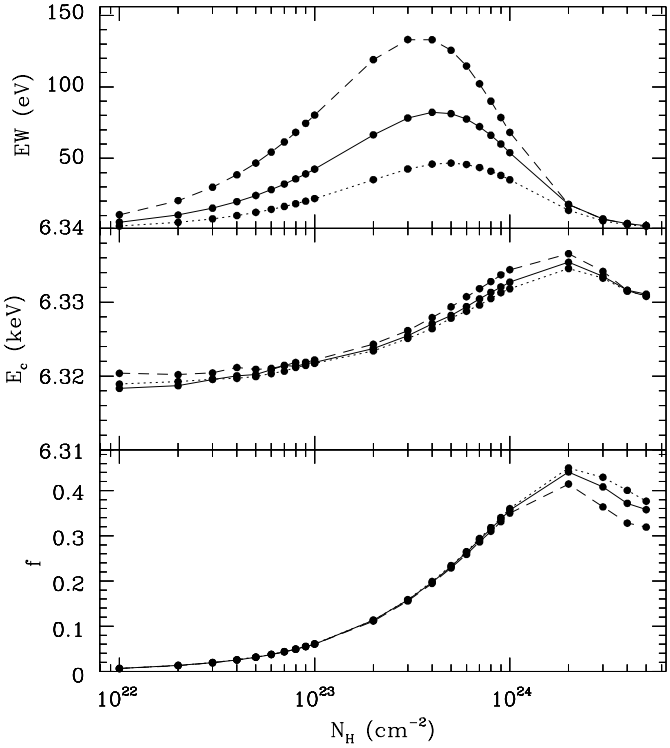

Fig. 3.21: *Top:* The equivalent width of the unscattered, narrow fluorescence line with respect to the incident continuum. *Middle and bottom:* Centroid energy and flux ratio, f, of the Compton shoulder to the unscattered line flux as a function of column density $N_{\rm H}$ for a centrally illuminated spherical distribution of cold matter. The dotted, solid and dashed lines refer to iron abundances $A_{\rm Fe}$= 0.5, 1, and 2, respectively. Modified after Matt (2002).

ratio is therefore – unlike the equivalent width of the primary fluorescence line – almost independent of the element abundance.

Der zweite denkbare Weg – Abbildung mittels Röntgenstrahlen – erscheint zunächst nicht erfolgversprechend, da brauchbare Optiken unbekannt sind; die "Unmöglichkeit einer abbildenden Optik für Röntgenstrahlen" spielt geradezu eine Rolle im festen Wissensbestand unserer Examenskandidaten.

The second possibility – imaging with X-rays – does not seem promising at first, since usable optics are unknown; the "impossibility of an imaging X-ray optic" is almost a fundamental part of knowledge of our examinees.

— Hans Wolter, 1952

4

X-ray Observatories and Instruments

This chapter gives an overview of the X-ray instruments used for the work in this thesis, *NuSTAR* and *XMM*-Newton. Very detailed information about each mission can be found in the respective instrument papers, so this is intended as a brief introduction with a focus on the technical subtleties relevant for this work. An introduction to Wolter optics can be found in Friedrich (2008). A comprehensive overview over X-ray detectors is given by Knoll (2000) and a very detailed textbook on CCDs is Janesick (2001). In order to avoid being repetitive, the interested reader is referred to the following *NuSTAR* and *XMM*-Newton related Master's and PhD theses for further technical and data extraction details. Specifically, Bhalerao (2012) gives a detailed description of the *NuSTAR* detector architecture and calibration. Kreikenbohm (2013) nicely summarizes the characteristics of the effective area, point spread function, and instrumental background of *XMM*-Newton and Hanke (2011) concisely describe basic X-ray analysis techniques such as forward folding, background handling, and gainshift corrections.

4.1 The Nuclear Spectroscopic Array (*NuSTAR*)

The Nuclear Spectroscopic Array (*NuSTAR*) is a NASA Small Explorer Mission launched on 2012 June 13. What makes this mission different from previous hard X-ray observatories is that it uses Wolter I optics up to energies of 79 keV, an energy range that has previously only been accessible with non-imaging collimators (e.g., the Proportional Counter Array, PCA, on the Rossi X-ray Timing Explorer, *RXTE*, Glasser et al. 1994) or coded masks (e.g., the BAT instrument on the Neils Gehrels *Swift* observatory or the IBIS instrument onboard *INTEGRAL*, Krimm et al. 2013 and Ubertini et al.

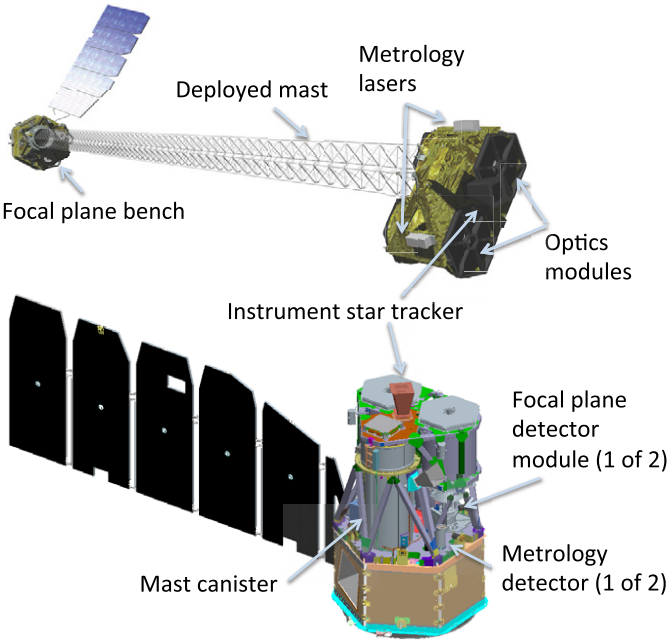

Fig. 4.1: Schematic of the *NuSTAR* observatory. Modified after Harrison et al. (2013).

2003, respectively) that allow imaging with very limited resolution. The high-resolution imaging capabilities of *NuSTAR* allow for a very high effective area and simultaneous, independent background measurements. This was achieved by a deployable mast that unfolded in space to reach a focal length of 10.1 m. The main technical description is given by Harrison et al. (2013) and details on the in-orbit calibration can be found in Madsen et al. (2015). A careful study of the *NuSTAR* background is presented in Wik et al. (2014). Bachetti et al. (2015) and Bachetti & Huppenkothen (2018) describe analysis strategies regarding instrument dead time for high-precision timing. A schematic illustration of the spacecraft is shown in Fig. 4.1.

The X-rays are focused by two identical, co-aligned optics onto two solid state CdZnTe pixel detectors (Focal Plane Modules, FPM, -A and -B) with CsI anti-coincidence shielding. Unlike classical CCDs, the pixels are read out only upon trigger which allows for incident count rates up to $\sim 10^5$ cts s^{-1} pixel^{-1} without pile-up. The event processing time, however, limits the effectively observed count rate to $\sim$400 cts s^{-1}module^{-1}. The nominal energy resolution varies from $\sim$400 eV at 10 keV to $\sim$900 eV at 68 keV. Figure 4.2 shows the effective area as well as the FWHM of the primary peak of the RMF as a proxy for the energy resolution over the usable energy range. The collecting area is highest at around 10 keV and drops rapidly beyond 78 keV. *NuSTAR*'s prime capabilities are therefore hard X-ray observations at high energy and time resolution and it has for example been particularly successful at studying CRSF sources (see, e.g., Fürst et al. 2014, Vybornov et al. 2017), ultraluminous X-ray sources (see, e.g., Bachetti et al. 2013, Walton et al. 2018), reflection, hard states and state transitions in black hole binaries (e.g., Miller et al. 2013, Xu et al. 2018, García et al. 2019) as well as hard X-ray

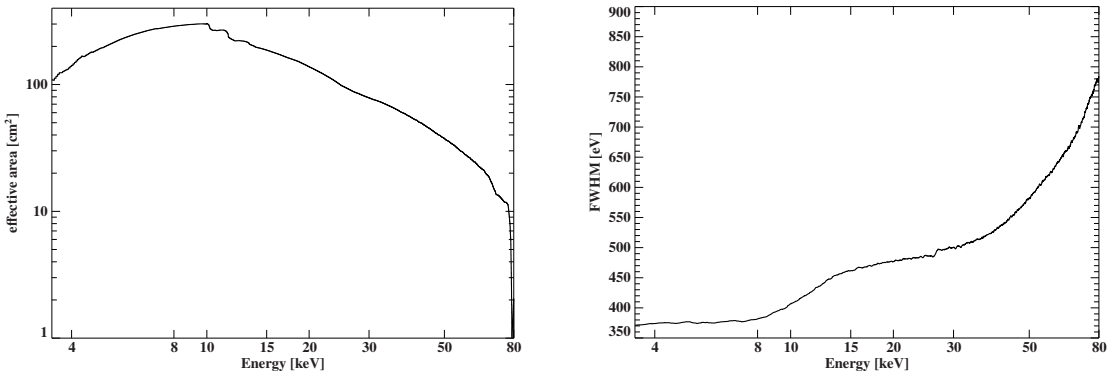

Fig. 4.2: *Left:* Effective area of a single *NuSTAR* FPM as function of energy. *Right:* FWHM of the primary peak of the RMF as indication for the energy resolution. Both plots are based on the standard default response files distributed for proposers.

emission in AGN (see, e.g., Brightman et al. 2015, Ricci et al. 2016, Lansbury et al. 2017).

As a consequence of its energy range and resolution, *NuSTAR* is less suited for direct atomic line diagnostics. Measurements of the hard X-ray continuum are, however, also crucial for photoionization and absorption diagnostics, because they require sound knowledge of the incident continuum. Therefore, the highest diagnostic power of high-resolution, soft X-ray spectrometers such as the High and Low Energy Transmission Gratings (HETG and LETG, respectively) onboard *Chandra* but also CCD-resolution spectrometers such as EPIC instruments onboard *XMM*-Newton has often been achieved by simultaneous observation with *NuSTAR* (see, e.g., Arévalo et al. 2014, Boissay-Malaquin et al. 2019, Annuar et al. 2020).

By design of the *NuSTAR* Data Analysis Software (`nustardas`), data reprocessing and extraction of standard science products is very straightforward. In the context of this thesis, the different observing modes of *NuSTAR*, however, might deserve a brief description. *NuSTAR* has six observing modes, whereas "mode" rather refers to a certain selection of attitude and instrumental parameters than different operation of the detectors (like, e.g., in the *XMM*-Newton EPIC detectors). The observing mode `SCIENCE` is the default mode for scientific analysis. The modes `OCCULTATION`, `SLEW`, and `SAA`, refer to Earth occultation, slewing of the spacecraft, and its passage through the South Atlantic Anomaly (SAA), a region of increased particle background due to the Earth's radiation belts, respectively. The `CALIBRATION` mode refers to those events recorded when the on-board calibration source was in the field of view. The second, non-standard mode to record science data is `SCIENCE_SC`. This mode also contains pointed observation without occultation, slew, or background contamination, but with poorer attitude reconstruction. The position of the optics with respect to the detector modules in the focal plane is continuously recorded by a metrology system that tracks

the spots of two IR laser on the optics bench with position sensing detectors on the focal plane bench and allows for later correction of distortions of the mast. In addition, *NuSTAR* has four star tracker units (Camera Head Units, CHU, 1–4), three mounted to the spacecraft bus (CHU 1–3) and one mounted to the optics bench (CHU 4). In the case CHU 4 cannot be used (e.g., because the sun or the moon is in the field of view), absolute pointing has to be reconstructed from the information of CHU 1–3 and the metrology system only. The accuracy of the sky coordinates reduces to $\sim 2'$ and the corresponding events are flagged as `SCIENCE_SC` mode. In principle, data taken in this mode can be used for scientific analysis although great caution and careful checking of the data products is advised as pointing uncertainties can affect PSF and vignetting corrections. Data taken in `SCIENCE_SC` can, however, also provide valuable additional exposure so its usage has to be evaluated on a case-to-case basis. Detailed instructions on how to handle `SCIENCE_SC` data are given in Sect. 6.7 of *The NuSTAR Data Analysis Software Guide*[1].

4.2 The X-ray Multi-Mirror (*XMM*)-Newton observatory

The *XMM*-Newton satellite (Jansen et al. 2001) was launched on 1999 December 10 with an Ariane V rocket by the European Space Agency. It carries three X-ray telescopes of 7.5 m focal length, consisting of 58 nested Wolter-I mirrors. The main scientific instruments are the European Photon Imaging Camera (EPIC; Strüder et al. 2001, Turner et al. 2001), the Reflection Grating Spectrometer (RGS; Brinkman et al. 1998, den Herder et al. 2001), and the Optical Monitor (OM; Mason et al. 2001). The EPIC instruments are equipped with one pn- and two MOS-type CCDs and have a usable energy range of ~0.2–10 keV. The two identical RGS consist of reflection grating stacks placed along the optical axes of two of the three Wolter I mirrors which deflect approximately half of the X-ray radiation. The dispersed spectra are recorded on nine back-illuminated CCDs and the position of a detected photon relates to its wavelength. For the design of the RGS, first and second order of the dispersed spectra overlap on the CCD; they can however be resolved by measuring the photon's energy on the CCD (simultaneously to its position). This setup allows for X-ray spectroscopy in the 0.3–2.1 keV range with an energy resolution $\Delta E/E$ of 100–500. Figure 4.3 shows the effective areas of the individual X-ray instruments on-board *XMM*-Newton.

XMM-Newton's prime capabilities are its large collecting area and the simultaneous operation of the high-resolution RGS and the medium-resolution EPIC instruments. The many scientific highlights of *XMM*-Newton's more than twenty years of operation include (among others) iron fluorescence line diagnostic (e.g., Wilms et al. 2001, Nandra et al. 2007, Hiemstra et al. 2011) and high-resolution absorption spectroscopy (e.g., Sako et al. 2001) in X-ray sources and AGN, dust absorption and scattering (e.g., Vuong

[1] `https://heasarc.gsfc.nasa.gov/docs/nustar/analysis/nustar_swguide.pdf`

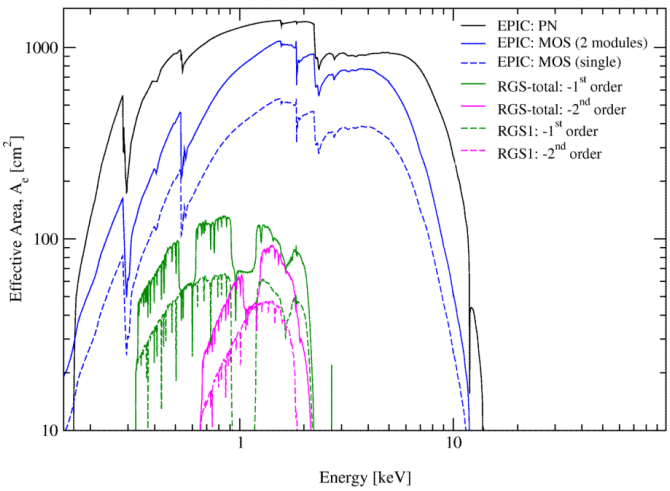

Fig. 4.3: Effective area of all *XMM*-Newton X-ray telescopes, EPIC and RGS. Modified after the *XMM*-Newton Users Handbook.

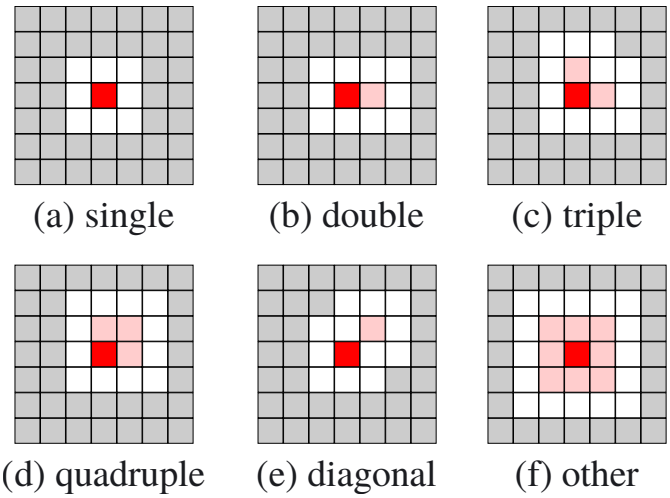

Fig. 4.4: Examples of EPIC pattern classification. The central dark red pixel contains maximum charge, light red pixels contain charge above a threshold value whereas white pixels are necessarily below this threshold. Grey pixels do not influence the pattern classification of the event. Modified after Jethwa et al. (2015).

et al. 2003, Pintore et al. 2017, Sguera et al. 2020, Psaradaki et al. 2020), but also GRB afterglows (e.g., D'Avanzo et al. 2018), Tidal Disruption Events (e.g., Lin et al. 2018), Soft Gamma Ray repeaters (e.g., Rea et al. 2010), ULXs (e.g., Pinto et al. 2016, Israel et al. 2017) and galaxy clusters (e.g., Eckert et al. 2015).

Unlike *NuSTAR*, *XMM*-Newton reads out CCD frames and is therefore more sensitive to pile-up. Pile-up refers to the effect that more than one photon deposits its energy in the same or a nearby pixel within one read-out cycle and are thus recorded as just one event with approximately the sum of individual photon energies. Since in general also charge clouds generated by a single photon often propagate into neighboring pixels, event reconstruction in the presence of pile-up is particularly difficult. How the charge cloud distributes over neighboring pixels is referred to as the *event pattern*. The classification of the event patterns of the *XMM*-Newton EPIC instruments is illustrated in Fig. 4.4.

XMM-Newton offers several observing modes to cover a wide range of observable source fluxes and mitigate pile-up effects. The general strategy is always to reduce the exposure per frame and thus the probability of more than one photon being registered in a valid pattern during the read-out cycle. The EPIC *imaging modes* are Full frame, Extended Full frame (pn only), and Large and Small Window mode, with frame times ranging from 199.1 ms to 5.7 ms for pn and 2.6 s to 0.3 s for MOS. At very high count rates, the EPIC instruments can be operated in *timing mode*, where the CCD is only read out in one dimension. As a consequence, spatial information is lost but frame times of 0.03 ms and 1.75 ms for MOS are reached. EPIC pn additionally provides a *burst mode* with 7 μs resolution, however, at the cost of very low efficiency because 97% events are discarded. Many galactic X-ray binaries regularly reach fluxes that can only be observed in timing mode.

On the user-side, pile-up effects can be reduced by excising the pixels in the core of the point spread function (PSF). Basic instructions on how to deal with potentially piled-up observations are given by the *XMM*-Newton Users Handbook[2]. A dedicated study of pile-up effects in the EPIC instruments is presented by Jethwa et al. (2015). Pile-up is a severe issue for spectral and timing analysis and observationally manifests itself as spectral hardening (because several soft photons are registered as one single hard photon), pattern degradation (i.e., an unexpected distribution of event pattern). In extreme cases, the observed flux even decreases with increasing count rate because individual photons can pile up to invalid patterns and are thus rejected. It should also be noted that pile-up can never be completely and rigorously eliminated but its effects are rather reduced to a tolerable level.

A second aspect regarding the event reconstruction in the context of variable count rates that deserves attention is correction for Charge Transfer Inefficiency (CTI)[3]. At read-out charges generated in the individual pixels are transferred by a varying electronic potential across the CCD to the read-out electronics. Due to imperfections in the semiconductor lattice, a fraction of the charge gets captured in charge traps. The charge loss therefore depends on the position of the event, but also on the count rate because charge traps tend to saturate with increasing count rate. Corrections for CTI losses are performed per default in standard data processing of EPIC data, but in some cases may suffer from calibration uncertainties of the assumed CTI model.

Due to the dispersion of the incident photons, the RGS is much less sensitive to pile-up and only observations of very bright sources might be affected. A detailed investigation of pile-up effects in the RGS is given in the *XMM*-Newton calibration

[2] https://xmm-tools.cosmos.esa.int/external/xmm_user_support/documentation/uhb/XMM_UHB.pdf

[3] Charge Transfer Efficiency (CTE) describes the same physical effect of charge loss during read-out. Some authors prefer to use CTI, others CTE; this is only a matter of personal taste, and maybe philosophy of life.

memo CAL-TN-0075-1-0[4]. CTI effects are virtually negligible since primary energy reconstruction is based on the dispersion angle and the charge cloud reconstruction is only used for order discrimination.

[4] https://xmmweb.esac.esa.int/docs/documents/CAL-TN-0075-1-0.pdf

Such extremely fine solid dust particles with a diameter of about one-hundredth of the wavelength of visual light would still be small enough to produce Rayleigh scattering. We see, thus, that our numerical results for the selective absorption cannot be traced to Rayleigh scattering by free atoms in interstellar space; they admit, however, interpretation as scattering by fine cosmic dust.

— Robert Trumpler, 1930

5

Dust and gas absorption and fluorescence in the high-mass X-ray binary IGR J16318−4848

This chapter describes the analysis of *NuSTAR* and *XMM*-Newton data of the high-mass X-ray binary IGR J16318−4848, one of the most heavily absorbed X-ray sources known, with the focus on the absorption modeling and the comparison and discussion of gas and dust absorbers. Large parts of the content of this chapter have been taken in verbatim from R. Ballhausen, M. Lorenz, F. Fürst, K. Pottschmidt, L. Corrales, J. Tomsick, M. Bissinger né Kühnel, P. Kretschmar, T. Kallman, V. Grinberg, N. Hell, I. Psadaraki, D. Rogantini, and J. Wilms, *Dust and gas absorption in the High Mass X-ray Binary IGR J16318−4848*, 2020, A&A, 641, A65, reproduced with permission © ESO. These parts are indicated by single quotes without direct reference.

5.1 Absorbed X-ray binaries and the special case of IGR J16318−4848

The majority of galactic X-ray binaries have column densities (including source-intrinsic and foreground absorption) range from 10^{19} to 10^{23} cm^{-2} The effect of these absorption columns is already far from being negligible in modern X-ray spectroscopy, at least when caring for the soft X-ray band. The optical depth shown in Fig. 3.3 corresponds to a column density of 10^{21} cm^{-2} with ISM composition which can already be considered moderately absorbed.

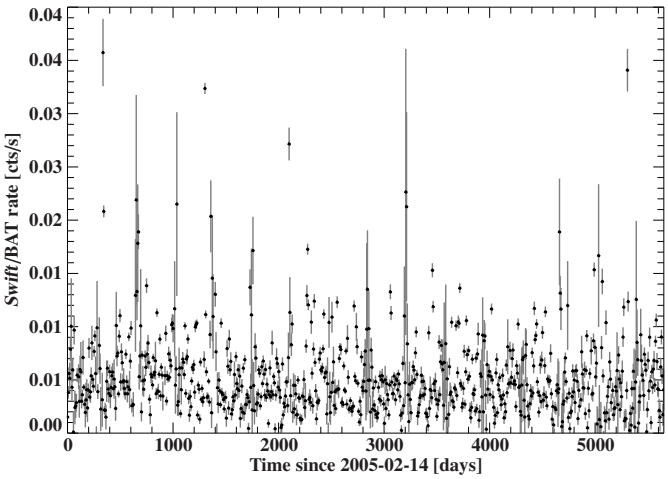

Fig. 5.1: Weekly (top) and daily (bottom) *Swift*/BAT lightcurve (Krimm et al. 2013) of IGR J16318−4848. The close-up of a four month interval shows indications of the possible 80 days orbital period.

'With a column density on the order of 10^{24} cm^{-2}, IGR J16318−4848 is one of the most strongly intrinsically absorbed X-ray sources in our Galaxy. It was discovered during routine scans of the Galactic plane by the IBIS/ISGRI instrument on board the *INTEGRAL* satellite in 2003 January (Courvoisier et al. 2003, Walter et al. 2003). A follow-up *XMM*-Newton observation in 2003 February revealed the very strong absorption and strong K-shell emission lines of Fe and Ni (Matt & Guainazzi 2003). These authors presented a detailed study of the absorbing and emitting material in the vicinity of the source, and detected a very weak Compton shoulder of the emission lines from which they concluded an anisotropy of the absorber with an average column density of a few 10^{23} cm^{-2}.'

These characteristic spectral features make IGR J16318−4848 very enigmatic. For comparison the HXMB GX 301−2 has a column density of approximately 10^{23} cm^{-2} with a strong iron line complex exhibiting a distinct Compton shoulder (Watanabe et al. 2003; see also Fig. 3.20). IGR J16318−4848 has a column density roughly a factor two higher, yet a comparably strong Compton shoulder is not observed which raises the question of how the absorbing material is different from other heavily absorbed HMXBs.

'The high absorption column and the strong fluorescence lines, which dominate the source flux below 10 keV, were confirmed in the analysis of 2006 August observations with *Suzaku* by Barragán et al. (2009). The upper limit on the strength of the Compton shoulder of the emission lines in these observations again strongly argues for an inhomogeneous and anisotropic absorber. A re-analysis of archival *ASCA* data revealed the source to be persistent (Murakami et al. 2003). Later *INTEGRAL* monitoring revealed IGR J16318−4848 to be a strongly variable hard X-ray source (Barragán et al. 2010a,b).' The variability is mostly irregular but 'Iyer & Paul (2017) propose a ∼80 d orbit based on intensity variations in the *Swift*/BAT light curve' which is shown for different time ranges in Fig. 5.1. 'A *Hitomi* observation in 2016 March constrained the ionization state of iron to be less than Fe IV and revealed line width broadening

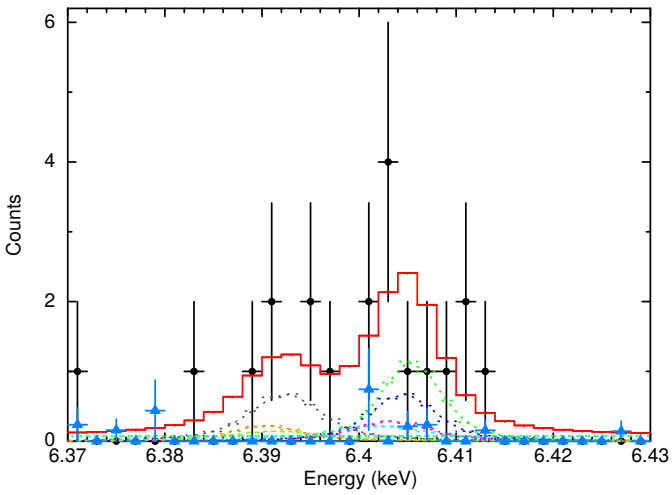

Fig. 5.2: *Hitomi* SXS spectum of the iron line complex of IGR J16318−4848 (black data points) with 2 eV binning. The model is a sum of seven Lorentzian functions and a powerlaw continuum (red solid line). Individual components are shown as dashed, colored lines. Blue filled triangles show the calculated non-X-ray background. Figure modified after Hitomi Collaboration (2018).

corresponding to 160 km s^{-1} (Hitomi Collaboration 2018).' The spectrum of the iron line complex obtained with micro-calorimeter array Soft X-ray spectrometer (SXS) is shown in Fig. 5.2. This observation, although unprecedented in spectral resolution (all previous observations of the iron line complex have been performed at CCD resolution or worse) has only ∼20 counts in total. A Compton shoulder feature might therefore likely have been escaped detection due to low statistics.

'A possible optical counterpart for IGR J16318−4848 was proposed by Foschini et al. (2003). Dedicated optical and near-infrared (NIR) observations confirmed and refined the detection of the optical companion, which Chaty & Filliatre (2004) and Filliatre & Chaty (2004) concluded was a sgB[e] star with a distance estimate ranging from 0.9 to 6.2 kpc. The infrared observations indicate that the star is probably embedded in dense and absorbing circumstellar matter. Moon et al. (2007) and Chaty & Rahoui (2012) suggest that this source-intrinsic absorber contains cold and warm dust. The interstellar absorption is two orders of magnitude lower than the circumstellar absorption (Chaty & Filliatre 2004). More recently, Fortin et al. (2020) performed stellar atmosphere and wind modeling using VLT/X-shooter observations and concluded an inclination of the system higher than 76° from broadband NIR and optical data. They also observed optical forbidden lines originating from an optically thin medium, possibly a disk wind. The nature of the compact object is still under debate (e.g., Walter et al. 2003, Barragán et al. 2009). The compact X-ray source and the sgB[e] companion place this source among the high mass X-ray binaries (HMXBs).'

5.2 Observations and data reduction

This analysis is based on observational data taken by *NuSTAR* and *XMM*-Newton. General information about these instruments is given in Chapter 4. What makes this observation particularly valuable and different from previous observational endeavors is

the simultaneous observation of the fluorescence line complex at high spectral resolution and the hard X-ray continuum that drives the fluorescence process. A similar energy coverage was previously only obtained by *Suzaku* (Barragán et al. 2009), yet at lower signal-to-noise. Here I present details of the data reduction specific to the joint *XMM*-Newton and *NuSTAR* observation.

IGR J16318−4848 was observed by *NuSTAR* on 2014 August 22 and 23 (ObsID 30001006002). 'We processed these data with the standard `NUSTARDAS` pipeline version 1.8.0 with CalDB version 20191219. The source regions were circles of 80″ radius, while the background regions were three circles of 140″ radius each, placed at the remaining corners of the field of view.

We included data taken in SCIENCE_SC mode, where the attitude reconstruction is performed only by the spacecraft star trackers and not by the star trackers on the optical module. The position reconstruction in this observing mode is less precise and it is triggered, for example when the optical module star trackers are blinded by the moon or sun.' Usually, data taken in this mode are not used for scientific analysis, as inaccuracies of the postion reconstruction might propagate to the ARF and vignetting calculations. However, 'we carefully checked that the spectral shape of the SCIENCE_SC mode data is in very good agreement with the standard SCIENCE mode data. We therefore combined the SCIENCE and SCIENCE_SC data, adding ∼8 ks more exposure per FPM to yield a total net exposure of ∼64 ks per FPM.' The additional SCIENCE_SC is most valuable for the time-resolved spectroscopy of short intervals. 'All times were barycentered with the FTOOL `barycorr`. We used the *Interactive Spectral Interpretation System* (ISIS v. 1.6.2; Houck & Denicola 2000) for all spectral and timing analyses. Uncertainties are given at the 90% confidence level for one parameter of interest unless stated otherwise.'

'*XMM*-Newton observed IGR J16318−4848 on 2014 August 22 and 23 for ∼64 ks (ObsID 0742270201), simultaneous with *NuSTAR*. Using the Science Analysis System (SAS) version 18.0.0, we extracted the EPIC-pn, -MOS1, and -MOS2 spectra and light curves following standard reprocessing and screening criteria and employing circular source and background regions of 40″ and 60″ radius, respectively.

We use single and double events for EPIC-pn and single events for EPIC-MOS for our spectral analysis to ensure the most accurate charge transfer efficiency and response calibration at low energies as required for constraining the continuum absorption and emission line profile. The loss of hard X-ray events due to the pattern restriction is tolerable because of the overlap with the high quality *NuSTAR* data. We exclude spectral channels below 3 keV where the data are strongly absorbed and the spectrum has a very low S/N. We also ignore the RGS as the energy range accessible to the RGS is also too strongly absorbed to obtain a significant S/N value.'

5.3 Time-averaged spectroscopy

‘For our spectroscopic analyses we used the 3–10 keV and 5–60 keV spectra of the *XMM*-Newton/EPIC-pn and *NuSTAR* FPMs, respectively. The *NuSTAR* FPMA and -B spectra were jointly rebinned requiring a minimum S/N of 15 and adding at least 2 and 4 channels below and above 40 keV, respectively. The *XMM*-Newton/EPIC-pn spectrum was rebinned adding at least four channels and additionally requiring a minimum S/N of 5 and 10 below and above 6 keV, respectively. We introduce a constant gainshift per instrument to account for possible remaining calibration uncertainties of the energy scale (see, e.g., Briel et al. 2005, Kitaguchi et al. 2011, for details on the charge transfer modeling in *XMM*-Newton and *NuSTAR*, respectively). This approach has proven necessary because in physically motivated photoionization models, line and edge energies are not free parameters but reference values from some corresponding atomic database. Therefore, instrument calibration uncertainties cannot be accounted for by the spectral model. Furthermore, we introduced flux cross-calibration constants with respect to *NuSTAR* FPMA.’

5.3.1 Empirical emission line modeling

Traditionally, X-ray spectra HMXBs are modeled using empirical continuum models like powerlaws with various high-energy cutoffs and, if required, additional components such as a blackbody to account for soft excesses. More sophisticated, physics-based continuum models have been published over the last few years (e.g., Becker & Wolff 2007, for highly magnetized neutron stars at high mass accretion rates) but their applications to observational data is very challenging and therefore still small in number (see Wolff et al. 2016, for one example). While absorption, fluorescence, and reflection modeling has always been closely oriented toward accurate usage of atomic reference data – certainly also because the many underlying processes can be studied in the laboratory, whereas for example Comptonization in strong magnetic fields cannot be – the systematic effect of the continuum modeling should always be considered carefully taken into account. Since the nature of the compact object in IGR J16318−4848 is not confirmed (the spectral shape suggests a neutron star but coherent pulsations have not yet been detected), there is no foundation of pushing the continuum modeling beyond an empirical description.

‘Following previous analyses (e.g., Ibarra et al. 2007, Barragán et al. 2009), we first describe the data with a power law with an exponential cutoff (called `cutoffpl` in `isis`/`xspec`) with photon index Γ and folding energy E_{fold}, accounting for photoelectric absorption with the model `tbabs` v.2 [1], parameterizing absorption using the equivalent hydrogen column density N_{H}. We used abundances and cross sections according to Asplund et al. (2009) and Verner et al. (1996), respectively. We left the iron abundance free to model the iron K-edge. The absorber is further modified by an optically thin

[1] see `http://pulsar.sternwarte.uni-erlangen.de/wilms/research/tbabs/`

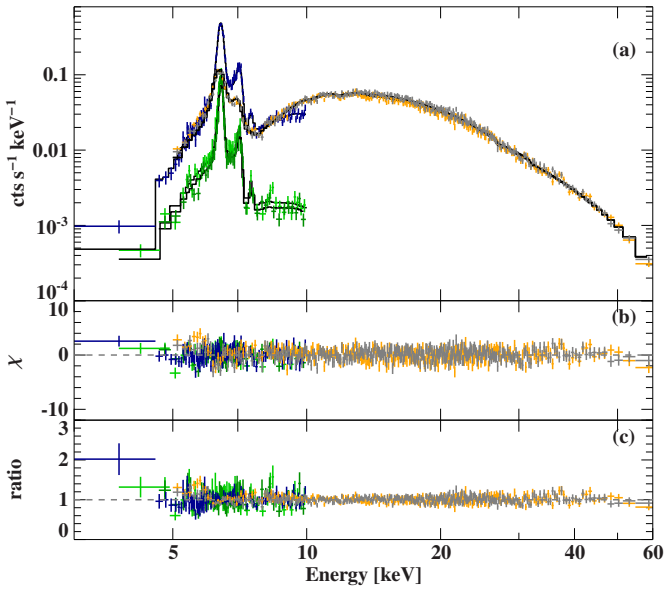

Fig. 5.3: **(a)** Time-averaged counts spectrum of IGR J16318−4848 with best-fit cutoff power-law model for *NuSTAR* FPMA (gray), FPMB (gold), *XMM*-Newton/EPIC-pn (blue), and *XMM*-Newton/EPIC-MOS1 and -MOS2 (dark and light green, respectively). **(b)** and **(c)** Residuals and ratio for the best-fit model. Modified after Ballhausen et al. (2020).

Compton scattering component (`cabs`) with the same column density as the neutral absorber. Similar to all previous observations, the spectrum shows very strong fluorescence lines of Fe Kα, Fe Kβ, and Ni Kα (e.g., Matt & Guainazzi 2003). Based on the *Hitomi* results (Hitomi Collaboration 2018), we modeled these with Gaussian emission lines and fixed the centroids at 6.404 keV, 7.058 keV, and 7.478 keV, respectively. Since the line broadening seen with *Hitomi* cannot be resolved with *XMM*-Newton or *NuSTAR*, we fixed all line widths to 3.4 eV. In `xspec`-like notation, our model is defined as

$$S(E) = \texttt{gainshift} \times \texttt{detconst} \times \texttt{tbnew} \times \texttt{cabs} \times (\texttt{cutoffpl} \times \texttt{ComptonShoulder} + 3 \times \texttt{gauss}) \,. \quad (5.1)$$

The time-averaged spectrum and best-fit model are shown in Fig. 5.3. Table 5.1 lists the best-fit parameters. The fit confirms the general results of earlier papers that the spectrum is dominated by a very strong fluorescence Fe Kα line and a strong Fe K-edge that overlays an exponentially cut off power law. The flux below 10 keV is fully dominated by the emission lines. Because the different components are treated as independent of each other, however, the physical interpretation of these parameters with respect to the absorber geometry and physics is difficult.'

5.3.2 Compton shoulder

The diagnostic power of the Compton shoulder is already discussed in Sect. 3.7.2. It originates from Compton down-scattering of fluorescence photons and its strength therefore constrains the electron density that the fluorescence photons encounter on their

Table 5.1: Best-fit parameters for the `cutoffpl` model. Modified from Ballhausen et al. (2020).

N_{H}	$(179 \pm 6) \times 10^{22}\,\mathrm{cm}^{-2}$
$a_{\mathrm{Fe}}{}^{a}$	1.07 ± 0.03
Γ	0.30 ± 0.11
E_{fold}	$14.0^{+0.8}_{-0.7}\,\mathrm{keV}$
$F_{3-50\,\mathrm{keV}}{}^{b}$	$(1.20 \pm 0.08) \times 10^{-9}\,\mathrm{erg\,s^{-1}\,cm^{-2}}$
$A_{\mathrm{Fe\,K}\alpha}{}^{c}$	$\left(6.5^{+0.8}_{-0.7}\right) \times 10^{-3}\,\mathrm{ph\,s^{-1}\,cm^{-2}}$
$A_{\mathrm{Fe\,K}\beta}{}^{c}$	$\left(6.8^{+0.8}_{-0.7}\right) \times 10^{-4}\,\mathrm{ph\,s^{-1}\,cm^{-2}}$
$A_{\mathrm{Ni\,K}\alpha}{}^{c}$	$\left(8.4^{+2.0}_{-1.7}\right) \times 10^{-4}\,\mathrm{ph\,s^{-1}\,cm^{-2}}$
f_{CS}	0.11 ± 0.04
$c_{\mathrm{FPMA}}{}^{d}$	1
$c_{\mathrm{FPMB}}{}^{d}$	1.036 ± 0.011
$c_{\mathrm{EPIC-pn}}{}^{d}$	0.908 ± 0.017
$c_{\mathrm{EPIC-MOS1}}{}^{d}$	0.94 ± 0.04
$c_{\mathrm{EPIC-MOS2}}{}^{d}$	0.93 ± 0.04
$\mathrm{EG}_{\mathrm{FPMA}}{}^{e}$	$-25 \pm 9\,\mathrm{eV}$
$\mathrm{EG}_{\mathrm{FPMB}}{}^{e}$	$-67 \pm 9\,\mathrm{eV}$
$\mathrm{EG}_{\mathrm{EPIC-pn}}{}^{e}$	$9^{+4}_{-3}\,\mathrm{eV}$
$\mathrm{EG}_{\mathrm{EPIC-MOS1}}{}^{e}$	$28^{+4}_{-5}\,\mathrm{eV}$
$\mathrm{EG}_{\mathrm{EPIC-MOS2}}{}^{e}$	$7 \pm 4\,\mathrm{eV}$
χ^2_{red} (d.o.f.)	1.20 (864)

Notes. $^{(a)}$ Relative iron abundance compared to Asplund et al. (2009). $^{(b)}$ Unabsorbed 3–50 keV flux. $^{(c)}$ Absorbed line flux. $^{(d)}$ Detector cross-calibration constant with respect to FPMA. $^{(e)}$ Additive gain shift relative to the energy grid defined by the RMF.

way to the observer, which can then be compared to the equivalent hydrogen column density and finally fluorescence line strength.

'Its possible presence in the X-ray spectrum of IGR J16318−4848 has already been discussed in previous analyses (Matt & Guainazzi 2003, Barragán et al. 2009).

In order to constrain the strength of a possible Compton shoulder, we add a Gaussian emission feature at 6.3 keV with a width of 50 eV to the model and then determined the statistical significance and flux limits of this component. Adding the Compton shoulder component only slightly decreases χ^2 from 1069.2 to 1036.4, while introducing one additional free parameter. Following Protassov et al. (2002), we estimate the significance of this putative Compton shoulder component in a Monte Carlo simulation where we simulate the X-ray spectrum without a Compton shoulder and then estimate how often

a false positive detection of a Compton shoulder is seen with a $\Delta\chi^2$ that is larger than that found in the data. We find no false positive detections of a Compton shoulder in 10^5 Monte Carlo runs (i.e., the existence of a Compton shoulder is required at least at 4.4σ confidence by the joint *NuSTAR* and *XMM*-Newton data).

We find single-parameter 90% uncertainty of the ratio of the flux of the Compton shoulder with respect to that of the Fe Kα line ($f_{\rm CS}$) of $11 \pm 4\%$. This value is to be compared with the prediction of the strength of the Compton shoulder for the transmission through a centrally illuminated spherical absorber. Specifically, for column densities of $\sim 2 \times 10^{24}$ cm^{-2} Matt (2002) estimate that the Compton shoulder ratio should be ~45% (i.e., a factor of ~3–7 higher than observed in our data). This discrepancy is in agreement with earlier measurements. To explain this discrepancy with the data, previous authors have suggested low covering fractions (Matt & Guainazzi 2003) or highly structured inhomogeneous absorbers (e.g., Barragán et al. 2009) as a possible explanation. As we show in the next section, however, both explanations are difficult to reconcile with the absorption seen in the continuum.'

5.3.3 Constraints set by photoionization

'The main inconsistency of the empirical models that we applied so far and that were also used in earlier modeling of the spectrum of IGR J16318−4848 is that absorption and fluorescence emission are treated separately; this means that the absorption model, for which $N_{\rm H}$ and some element abundances are free to vary, provides no feedback on the emission lines, which are independent, additive components. This approach is mainly due to a lack of available models for `xspec`. One of the few models that aims at self-consistent modeling of photoabsorption and fluorescence is the `xspec` model `PEXMON` (Nandra et al. 2007). This model combines in an empirical way reflection from cold matter (Magdziarz & Zdziarski 1995) with line strengths by George & Fabian (1991) and Compton shoulder simulations by Matt (2002). However, `PEXMON` assumes a pure power law as incident spectrum with photon index $1.1 < \Gamma < 2.5$, and is therefore mostly applicable to Seyfert 1 galaxies, but not necessarily to HMXBs such as IGR J16318−4848. We therefore have to perform additional checks using more physical modeling to see whether our empirical model is self-consistent.'

In this context, self-consistency is supposed to mean a comprehensive quantitative description of the absorption and fluorescence emission by the same absorbing material, combining Eqs (3.2), (3.4), and (3.6) into a radiative transport problem. We employed the photoionization code `XSTAR` (Kallman & Bautista 2001, see also Sect. 3.4 for an introduction).

'In order to model the structure and emerging spectrum of a putative photoionized plasma around IGR J16318−4848, we ran a grid of `XSTAR` simulations in the parameter range of interest for IGR J16318−4848. We used an assumed distance of 5 kpc, well within the distance estimate interval and also supported by Fortin et al. (2020) with

a corresponding source luminosity of $1.33 \times 10^{36}\,\mathrm{erg\,s^{-1}}$ in the 13.6 eV to 13.6 keV energy range. The cloud that surrounds the source is irradiated with a power law with an exponential cutoff derived from the empirical fits as the input spectrum. We caution that the derivation of the shape of the unabsorbed incident continuum depends on the choice of the iron abundance in our empirical fit. The iron abundance in our `XSTAR` simulation is therefore not allowed to vary in order to avoid inconsistencies in the model assumptions. We cannot rule out that a systematic exploration of different iron abundances along with continuum shapes could result in a better fit to the data. This is, however, beyond the scope of this work. We also note that the observational data do not completely span the energy range required by `XSTAR`, so our spectra and luminosity rely on the assumption that the spectral shape does not deviate significantly from an extrapolation below 3 keV which is, however, likely to lead to a significant ultraviolet excess. Elements included in the simulation are H, He, C, N, O, F, Ne, Mg, Si, S, Ar, Ca, Cr, Mn, Fe, Co, and Ni with solar abundances (based on Grevesse et al. 1996). Furthermore, we set the hydrogen particle number density to $6.5 \times 10^{10}\,\mathrm{cm^{-3}}$, which we estimated from the column density of the empirical fits, and the estimated size of the emission region of 3×10^{13} cm from Matt & Guainazzi (2003).

We first determine the rough model parameter range by visually comparing example `XSTAR` runs with the data, and then run a finer grid for spectral modeling. As computational constraints force us to leave some of the `XSTAR` parameters fixed in the preparation of the grid, we vary only those parameters that have the largest effect on the resulting spectral shape. Specifically, we produced table models for `xspec/isis` on a model grid where we varied the covering fraction from 0.9–1.0, N_H from $5 \times 10^{23}\,\mathrm{cm^{-2}}$ to $5 \times 10^{24}\,\mathrm{cm^{-2}}$, and the logarithm of the ionization parameter ($\log \xi$) from 0 to 5. Here, $\xi = L/(nR^2)$ (Tarter et al. 1969), where L is the source luminosity, n the particle density, and R is the absorber's distance from the source.

The choice of the limited range of covering fractions in our table model is motivated by preliminary `XSTAR` calculations where the covering fraction was varied over a range from 0.1–1.0. Figure 5.4 shows some of these spectra as an example to illustrate how the line flux with respect to the continuum depends on the covering fraction. At low covering fractions, a significant part of the incident radiation is transmitted, which dilutes the line. These early calculations show that the covering fraction has to be very close to 100% to reproduce the overall strong absorption and the strong emission lines with respect to the observed continuum. This is in contradiction to the conclusions made in earlier analyses of the X-ray spectrum of IGR J16318−4848 (e.g., Matt & Guainazzi 2003), where a lower covering fraction was inferred from the observed Compton shoulder flux and equivalent width of the Fe Kα line.'

'To compare these models with the data and explore the full parameter space, we employed Markov chain Monte Carlo (MCMC) calculations with affine-invariant ensemble sampling (see Goodman & Weare 2010, Foreman-Mackey et al. 2013, for details),

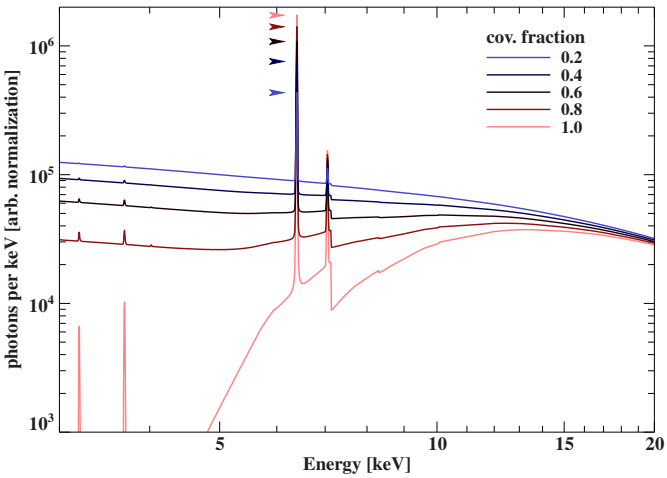

Fig. 5.4: Simulated XSTAR spectra for a wider range of covering fractions. Other model parameters are $N_{\mathrm{H}} = 10^{24}\,\mathrm{cm}^{-2}$ and $\log \xi = 1$. Vertical arrows indicate the maximum line flux for clarity. Modified after Ballhausen et al. (2020).

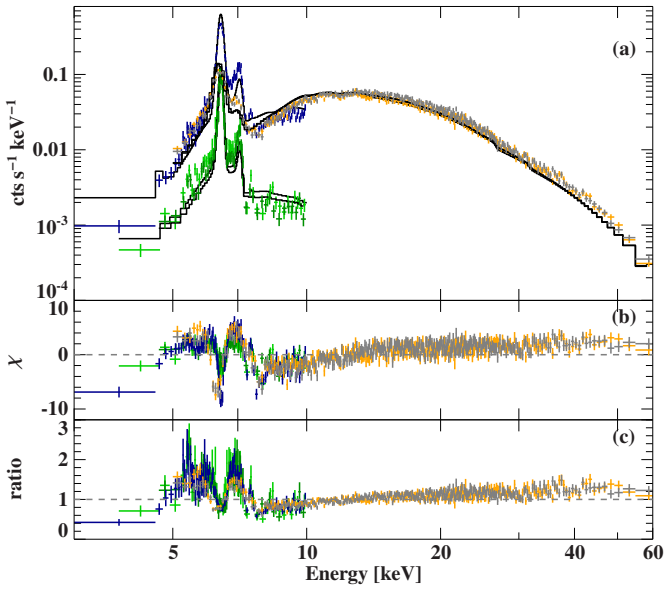

Fig. 5.5: Best fit of the single XSTAR model. Colors and panels are defined in Fig. 5.3. Modified after Ballhausen et al. (2020).

employing 300 walkers for six free parameters and 30 000 iterations. This approach is motivated by the complexity of physical photoionization models and their parameter space, where commonly used χ^2-minimization algorithms are prone to get stuck in local minima.' This applies in particular, parameters related to narrow (i.e., very localized) model components. Those can hardly be constrained with gradient methods unless the initial parameters are already very close to the final ones. For example, if the centroid energy of a narrow emission component in the fit model is far away from a line center in the data, numerical derivatives are unlikely to point the fit in the right direction. These parameters can be difficult to constrain automatically even with MCMC algorithms and require a sensible choice of initial parameters. Typical examples are red- or gainshifts or energies of narrow line features. In these cases, it might still be necessary to set initial

parameters manually or constrain those in empirical fits and fix them once it can be confirmed that they are model-independent.

'When we call a set of parameters "best fit" in the following, we refer to the most probable parameter combination unless noted otherwise. To reduce the number of free parameters, we fixed the detector flux and gainshift calibration constants to the values obtained from the empirical fits (Table 5.1). This is legitimate because these parameters are model independent and can be accurately determined from the earlier fits. Since fluorescence emission from ionization stages less than Ni IX is not included in `XSTAR`, the neutral Ni Kα fluorescence line was modeled by an additional Gaussian emission component with width fixed to 3.4 eV and energy fixed to 7.47 keV (Bearden 1967). In `xspec`-like notation, our fit model is given by

$$S(E) = \texttt{gainshift} \times \texttt{detconst} \times (\texttt{XSTAR} + \texttt{gauss}) \ . \tag{5.2}$$

Despite the large volume of parameter space covered, pure single-zone photoionization modeling fails to result in a satisfactory description of the data. Figure 5.5 shows the best fit from the MCMC. The low quality of the fit renders listing the corresponding parameters unnecessary. Although the spectral shape of the model looks similar to the data (a strong Fe line and approximately the correct continuum curvature), neither the Fe Kα/Kβ line ratio nor the depth of the iron K-edge (and possibly also at the nickel K-edge at ~8.34 keV) are described correctly. We note that the mismatch of the hard continuum in this fit is merely a normalization issue since the fit is dominated by the fluorescence lines. We note that even though numerical issues prohibit a further exploration of the parameter space, the best fit is of such low quality that it is very unlikely that opening up further parameters would yield a satisfactory description of the data.

We note, however, that there is a very clear indication from the empirical fit and from the photoionization modeling that the medium responsible for the emission of the Fe Kα emission line and for the formation of the Fe K-edge is for some reason overabundant in Fe.'

5.3.4 Dust absorption modeling

'The large mismatch between the Fe Kα line strength and the Fe K-edge depth, in combination with a very weak Compton shoulder that implies a low electron column, is difficult to reconcile with a gaseous absorber of solar abundances. In the previous section we also showed that within the constraints set by a strong Fe Kα line from neutral iron it is not possible to reconcile these observations with ionization effects. In this section, we study another possibility to explain the X-ray spectral shape: absorption of X-rays in a dust layer in the source. This approach is motivated by broadband NIR observations which suggest the presence of cold and warm dust within the binary system (Moon et al. 2007, Chaty & Rahoui 2012, Fortin et al. 2020), and by the general observation that

interstellar dust is strongly enriched in refractory elements (Dwek 2016). Since the optical observations indicate that the dusty absorber is source-intrinsic, we ignore dust scattering which gives rise, for example, to dust scattering halos when the dust is at a significant distance from the source, and treat absorption in dust only (Corrales et al. 2016).

Specifically, our dust-absorption model is a multiplicative factor of the form

$$\exp\left(-\tau_{\rm dust}\right) = \exp\left(-N_{\rm H}\sigma_{\rm dust}\right) \ , \tag{5.3}$$

where $\sigma_{\rm dust}$ is the (energy-dependent) absorption cross section per H-nucleon.

We describe the dust absorption cross section in the vicinity of the Fe K-edge using laboratory measurements by Rogantini et al. (2018) for various Fe containing minerals such as crystalline olivine ($Mg_{1.56}Fe_{0.4}Si_{0.91}O_4$), troilite (FeS), and pyrrhotite ($Fe_{0.875}S$). We present our results using the Rogantini et al. (2018) cross section for olivine for two reasons. First, the knowledge of grain size and abundance models are most reliable for silicates and graphites (see, e.g., Draine 2003a for a review, and Draine 2003b, Clayton et al. 2003, Nozawa & Fukugita 2013 for details). Second, due to the limited resolution of *NuSTAR* and *XMM*-Newton, we found that our results are insensitive to the specific choice of dust composition. Rogantini et al. (2018) assume a power-law grain size distribution after Mathis et al. (1977, hereafter MRN) and solar iron abundance according to Lodders & Palme (2009). According to their cross section normalization, there is one iron atom for each 2.5 olivine unit cells. We extrapolate these cross-sections outside of the tabulated energy range of 6.7–8.0 keV for the element composition of olivine based on the gas-phase cross sections by Verner & Yakovlev (1995).' Figure 5.6 shows the measured Rogantini et al. (2018) cross section for crystalline olivine together with the corresponding gas-phase cross section. 'This approach is justified since specific solid-state effects, i.e., X-ray absorption fine structure, mainly lead to deviations from the gas-phase cross section in areas close to the absorption edge (Lee & Ravel 2005, Lee et al. 2009).'

'We note that the total iron column along the line of sight is the most robust quantity to compare with other analyses, because it is constrained directly by the depth of the iron K-edge. For consistency with older studies, we map this quantity to the equivalent hydrogen column density assuming an iron abundance given by Asplund et al. (2009). We point out, however, that in a sgB[e] system the element abundances may depend strongly on the line of sight; in particular, heavier elements that are highly depleted into dust will accumulate in the circumstellar disk around the companion star, such that $N_{\rm H}$ determined from any fit with such a model is in all likelihood not a good estimate for the true hydrogen column.

Absorption by the iron atoms in the olivine grains will result in the emission of the Fe fluorescence line. We estimate the fluorescence line flux, $N_{{\rm ph},i}$ for $i = \alpha, \beta$, from the dust

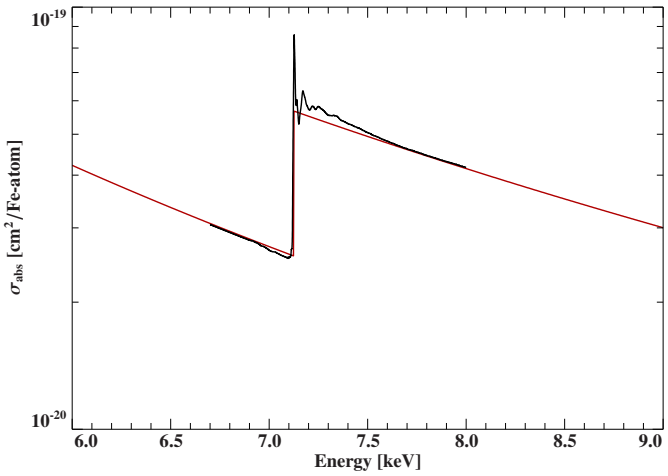

Fig. 5.6: Photoabsorption cross section per iron atom in crystalline olivine measured by Rogantini et al. (2018) (black). The red curve shows the Verner et al. (1996) cross section composed for $Mg_{1.56}Fe_{0.4}Si_{0.91}O_4$, slightly re-normalized to match the pre- and post-edge laboratory measurements.

absorber with a simple empirical model following Nagase et al. (1986, their Eq. 11),

$$N_{\mathrm{ph},i} = \gamma_i \omega_{\mathrm{K}} \int_{E_{\mathrm{K}}}^{\infty} \frac{\sigma_{\mathrm{Fe\,K}}(E)}{\sigma_{\mathrm{olivine}}(E)} N_{\mathrm{ph}}(E) \left[1 - \exp(-\tau(E))\right] \mathrm{d}E \,, \tag{5.4}$$

where $N_{\mathrm{ph}}(E)$ is the incident photon spectrum, $\omega_{\mathrm{K}} = 0.351$ is the fluorescence yield of iron (Hubbell et al. 1994), and γ_i is the branching ratio of the Kα to Kβ line. For neutral iron, as appropriate for a constituent in minerals, the intensity ratio Kβ/Kα is 0.132 (Han & Demir 2009). This quantity is expected to be at most slightly affected by solid state effects. In the Fe-band, self-absorption of Fe fluorescence photons in grains is negligible (Wilms et al. 2000, and Sect. 5.3.5).

To summarize, in order to describe the data with the dust model, we consider a pure dust absorber, which we describe in pseudo-`xspec` notation by

$$S(E) = \texttt{gainshift} \times \texttt{detconst} \times \Big(\eta \Big(\mathtt{N}_{\mathrm{ph},\alpha}(\texttt{cutoffpl}) + \mathtt{N}_{\mathrm{ph},\beta}(\texttt{cutoffpl}) \Big) + \exp\left(-\tau_{\mathrm{dust}}\right) \times (\texttt{cutoffpl} + \texttt{gauss}) \Big) \,, \tag{5.5}$$

where τ_{dust} and $\mathtt{N}_{\mathrm{ph},\alpha,\beta}$ were defined in Eq. (5.3) and Eq. (5.4), respectively. We note that in this model $\mathtt{N}_{\mathrm{ph},\alpha,\beta}$ are convolution models, since the fluorescence line strength is determined from the overall spectral shape above the Fe K-edge through Eq. (5.4). In addition to these physics-motivated components, our model includes an empirical correction factor η that accounts for the physical effects excluded in Eq. 5.4, such as self-absorption of the fluorescence radiation in the absorber, any residual effects of self-shielding by the grains, and geometrical dilution effects due to the unknown absorber geometry.

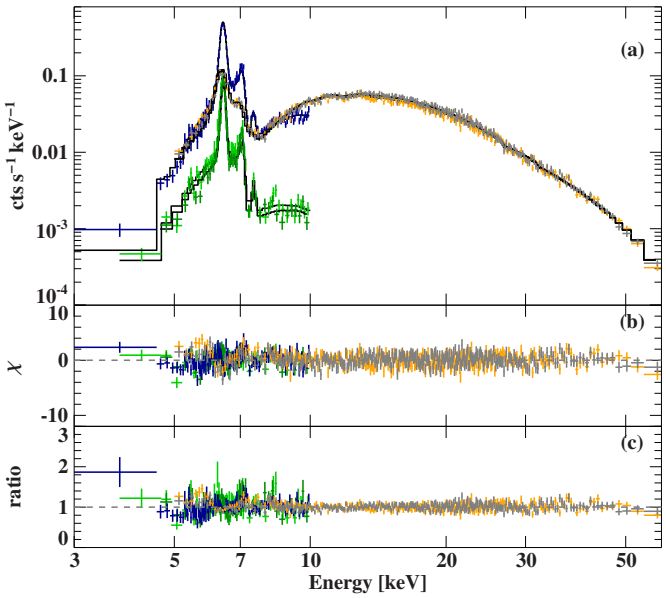

Fig. 5.7: Most probable olivine absorption and fluorescence model. Colors and panels are defined in Fig. 5.3. Modified after Ballhausen et al. (2020).

Since our olivine model does not include absorption by nickel, and thus the fluorescence yield cannot be calculated self-consistently, similar to our photoionization modeling (Sect. 5.3.3) we account for the Ni Kα line by adding a Gaussian emission line. The other fit parameters are $N_{\rm ph}$ and the spectral shape of the continuum. In Sect. 5.3.5 we check whether the results of our fits are consistent with detailed Monte Carlo simulations in which these effects are explicitly taken into account.'

'Figure 5.7 shows the spectrum with the most likely realization of the model. Even though we now have a physically much simpler model than the `XSTAR` one, the fit residuals look remarkably better than in our earlier attempts to model the spectrum. Despite the simplification of the olivine absorption model, the present fit also reproduces the Kα-to-Kβ ratio correctly. Parameter probability distributions are displayed in Fig. 5.8, and corresponding parameter values are listed in Table 5.2. Uncertainties on these parameters are obtained by numerical integration of the probability density function and thus represent the parameter range where 90% of the walkers settle.'

5.3.5 Numerical modeling of a dusty absorber: fluorescence, line strength, and Compton shoulder

'The results presented in the previous section show that a model in which the absorber purely consists of dust (i.e., a medium that is strongly enhanced in iron such as the olivine absorber used here as an example) can reproduce the observed spectral features in a quantitative way. In order to obtain a comparatively simple model that allows spectral fitting, we ignored several potentially important effects, including self-absorption of the fluorescence line emission, Compton scattering, or radiative transfer effects due to

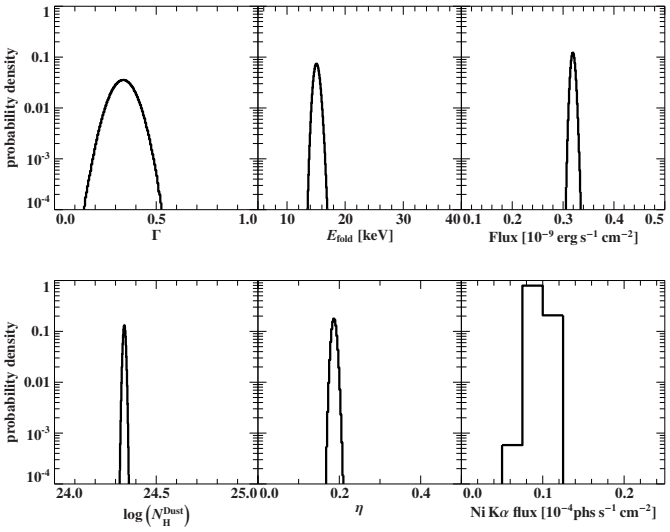

Fig. 5.8: Parameter probability distribution for the olivine absorption model including fluorescence. Additional parameters are the photon index Γ and folding energy $E_{\rm fold}$ of the continuum and the flux of the Ni Kα line (not accounted for by the dust absorption model). The column density $N_{\rm H}^{\rm Dust}$ refers to the equivalent hydrogen column density for the iron abundance of Asplund et al. (2009). Modified after Ballhausen et al. (2020).

Table 5.2: Most probable parameter values and uncertainties for the olivine absorption and fluorescence model. Modified after Ballhausen et al. (2020)

Γ	$0.34^{+0.09}_{-0.10}$
$E_{\rm fold}$	$15.0^{+0.9}_{-0.8}$ keV
$F_{3-50\,\rm keV}{}^{a}$	$(0.32 \pm 0.01) \times 10^{-9}$ erg s^{-1} cm^{-2}
$N_{\rm H}$	$221^{+5}_{-6} \times 10^{22}$ cm^{-2}
η	0.19 ± 0.01
$A_{\rm Ni\,K\alpha}{}^{b}$	$(9 \pm 2) \times 10^{-6}$ ph s^{-1} cm^{-2}

Notes. $^{(a)}$ Unabsorbed 3–50 keV flux. $^{(b)}$ Unabsorbed line flux.

the source geometry. While the fitted iron column density and the continuum shape obtained from these fits have a direct physical meaning, these effects were modeled by the introduction of the scaling parameter η in the fit model of Eq. (5.5).

Having shown that the dust absorber yields a good description of the data, in this section we refine the model further and perform direct Monte Carlo simulations of photon absorption and propagation in olivine dust grains. In order to do so we utilize the `SIXTE` software package (Dauser et al. 2019). Although this package is designed to simulate instrument effects in X-ray detectors, it contains tools that allow direct modeling of the physics of radiation propagation in any medium, including the effects of Compton scattering off bound electrons and of fluorescence.'

This approach is motivated by the idea that photoabsorption, followed by radiative de-excitation and subsequent escape of the fluorescence photon is the same process that also gives rise to the so-called *escape peak* in solid state detectors (Reed & Ware 1972). A similar analogy applies to the formation of the Compton-continuum and -edge in X-ray

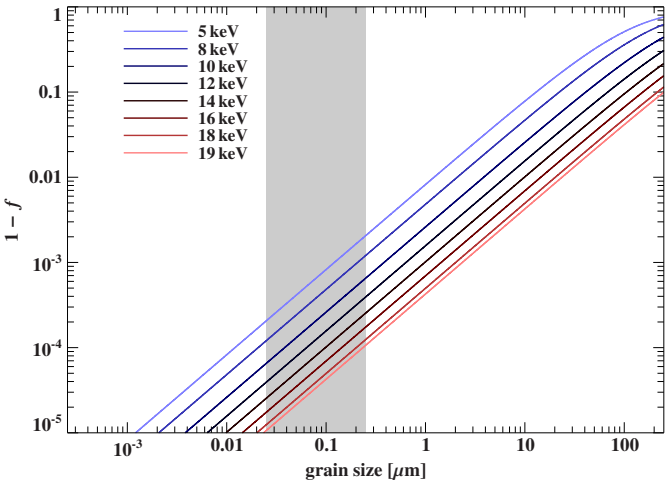

Fig. 5.9: Reduction of the optical depth due to self-blanketing effects. Modified after Ballhausen et al. (2020).

and γ-ray detectors, except that these emerge from the energy deposited on an electron (and therefore recorded) in the detector whereas the Compton shoulder of a fluorescence line in an astrophysical source characterizes the remaining energy of the photon after the scattering off an electron in the ambient medium. The necessary modifications of the `SIXTE` source code for the dust absorption and fluorescence simulations that are presented here were implemented by Maximilian Lorenz.

'In a first step we apply Eq. (A1) from Wilms et al. (2000) to calculate the optical depth of individual dust grains for iron Kα fluorescence photons in order to quantitatively confirm that we can ignore self-absorption inside a single grain. We assume a grain density ρ of 1 g cm^{-3}, resulting in a number density of 4.02×10^{21} unit cells cm^{-3}. For simplicity, we used partial photoionization cross sections by Verner et al. (1996) without fine structure. For typical grain sizes of 0.025–0.25 μm (Draine & Lee 1984) we find the optical depth of the individual grains to range from 2×10^{-4} to 2×10^{-3}. Re-absorption of the fluorescence photon only becomes dominant for grain sizes larger than $\sim$1 μm, while smaller grains are mostly transparent for photon energies below the iron K-edge. We therefore conclude that the grain size distribution has little effect on the fluorescence properties.'

As discussed in detail in Sec. 3.6, 'one significant difference between dust versus gas absorption is known as self-blanketing (Fireman 1974) where atoms in the interior of the dust grain are partially shielded by atoms on the surface. Effectively, this reduces the optical depth of a medium when its constituents are confined in dust grains compared to the same number of atoms in gas phase (assuming identical chemical composition). We calculate the self-blanketing factor f for olivine grains using Eqs. (A1) and (A5) of Wilms et al. (2000). For display purposes, the fractional reduction of the optical depth, $1 - f$, due to self-blanketing instead of f is shown in Fig. 5.9.'

'Again, self-blanketing becomes more significant with increasing grain size, but the change in optical depth is generally below 1% for the grain sizes and photon energies

considered here and therefore well below any systematic error that is introduced by our specific choice for the dust material and the unknown size distribution.

Because of the weak dependency of the results on the grain size distribution, in order to study radiative transfer effects we next simulate the emergence of fluorescence photons from spherical and slab-like absorbers of considerable optical depth. We perform simulations for a central point source embedded in a homogeneous, quasi-spherical olivine absorber, and for an infinite slab between a point source and the observer. We explicitly calculate the absorption, fluorescence, and Compton scattering of primary and fluorescence photons in this absorber.

Our implementation of Compton scattering correctly takes into account incoherent scattering from bound electrons (Hubbell et al. 1975). To estimate the scattering factor for olivine, we took the weighted mean of the constituents and obtained the energy-dependent, total Compton scattering cross section by numerical integration over all scattering angles. The incident spectrum on these clouds is fixed to a power law with exponential cutoff with the best-fit parameters obtained in the previous section (Table 5.2), while we vary the absorber's column density. Leahy & Creighton (1993, and references therein) and Matt (2002) present results of earlier simulations of fluorescence calculations and the Compton shoulder for the case of spherical and slab geometries, respectively, which used approximate photoabsorption cross sections and assumed free electrons.

The Monte Carlo simulations clearly show that the emerging flux of the Fe Kα fluorescence line is strongly geometry dependent (see Fig. 5.10). The reason is that the most probable location of the initial fluorescence event is located in the vicinity of the absorber's $\tau = 1$ surface. In the case of a slab geometry the fluorescence photons that are emitted into the hemisphere towards the observer will have to penetrate a higher optical depth than those emitted opposite the observers side (i.e., toward the point source), where in contrast to the K-edge energy, the optical depth at 6.4 keV is significantly less than 1. For a sphere, however, this asymmetry does not exist, and as a result the observable line flux for the slab geometry is a factor of 2–3 lower than for the spherical geometry.

To connect these results to the best-fit results from Sect. 5.3.4, we derive the scaling factor η included in Eq. (5.5) for both simulations by comparing the simulated fluorescence photon flux with that predicted from Eq. (5.4). Figure 5.10 shows η as obtained from our simulations for spherical and slab geometry as a function of column density.' The decrease of η with increasing column density is mainly an effect of re-absorption of the fluorescence photons by the ambient medium. With vanishing column density and spherical geometry, η approaches unity, i.e, every fluorescence photon that is generated can leave the medium and incident and fluorescence photons are emitted in the same solid angle of 4π. Note again, that η does not contain the probability to generate a fluorescence photon in the first place.

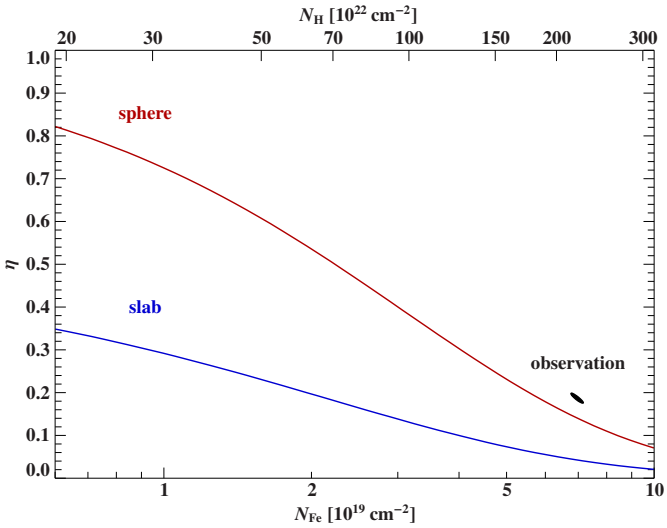

Fig. 5.10: Correction factor η for spherical and slab geometry (red and blue, respectively) as a function of column density obtained from Monte Carlo simulations. The black shaded region shows the 90% confidence contour from the MCMC spectral modeling. Modified after Ballhausen et al. (2020).

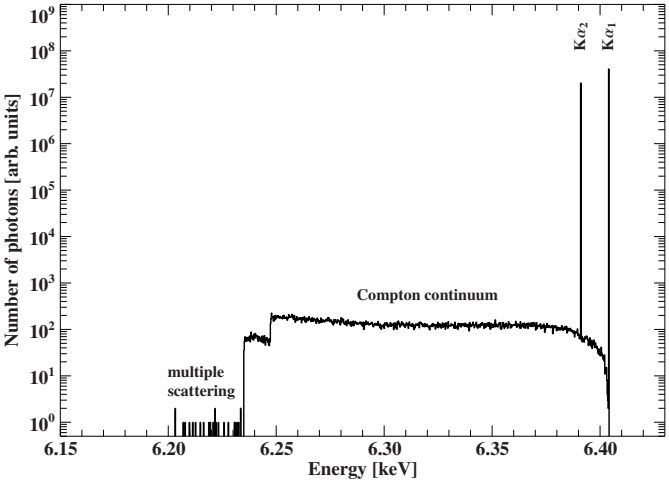

Fig. 5.11: Simulated Fe Kα line profile in an olivine absorber of Fe column density of 6×10^{19}cm^{-2}, including the Compton continuum. Modified after Ballhausen et al. (2020).

'The parameters obtained in Sect. 5.3.4 are very close to those obtained for the spherical geometry. Given the large difference in the predicted values for η between the two geometries, we conclude that a dusty geometry with a quasi-spherical absorber is qualitatively consistent with the observations, while a slab geometry is unlikely to explain the data, even if some of the assumptions of our model, such as the homogeneous distribution of dust, are relaxed.'

'Finally, as discussed above, in addition to our estimate of the primary Fe Kα fluorescence line flux, our Monte Carlo code considers Compton scattering off the electrons in the dust grains. This allows us to quantify the formation of the Compton shoulder in an absorber that consists of dust grains. Figure 5.11 shows the simulated energy distribution of the escaping photons around the Fe Kα fluorescence lines with Compton continuum for a quasi-spherical, homogeneous olivine absorber with a Fe column den-

sity $6 \times 10^{19}\mathrm{cm}^{-2}$. For the range of iron column densities considered in our simulations ($6\times10^{18}\,\mathrm{cm}^{-2} \leq N_{\mathrm{Fe}} \leq 1\times10^{20}\,\mathrm{cm}^{-2}$) we find Compton shoulder flux ratios of $\sim3\times10^{-4}$ to 2×10^{-2}, which is several orders of magnitude lower than for gas absorbers of the same iron column density with solar abundances. Among minor effects like the modification of the Compton scattering cross section for bound electrons, this is mainly because the effective electron number density per iron atom in our pure olivine dust model is roughly a factor 300 lower than the gas of solar or ISM abundances.'

5.4 Time-resolved spectral analysis

'So far, we have studied the time-averaged spectrum of IGR J16318−4848. As shown in Fig. 5.12a, however, the source is strongly variable on kilosecond timescales, which has been associated with changes in the absorber (Matt & Guainazzi 2003, Ibarra et al. 2007, Barragán et al. 2009). Here, we investigate the spectral variability with time.

No periodicity is apparent in the light curve, which is also confirmed by a search for periodicities on the cleaned, combined event data from FPMA and -B standard and SCIENCE_SC mode using epoch folding (Leahy et al. 1983) for trial periods of 1 s to 1000 s, as well as a power spectrum analysis. In order to trace spectral variability over time, we use the (H−S)/(H+S) hardness ratio. This quantity shows only moderate variability (Fig. 5.12b). To investigate their origin, we perform time-resolved spectroscopy on segments of the light curve over which the spectral shape does not vary significantly. Because the time intervals of the constant hardness ratio are likely to represent the same spectral state, we use the hardness ratio to define these time intervals using a Bayesian block analysis. We note, however, that for the given dataset the result of the Bayesian block analysis depends significantly on the `ncp_prior` parameter (for details, see Scargle et al. 2013), which controls the prior for the number of blocks and was set to 0.5. With this choice of prior, we caution that the detection of change points in the hardness ratio is only marginally significant.'

'Considering only time intervals of simultaneous *NuSTAR* and *XMM*-Newton coverage, we obtained 24 spectra of ∼0.7 ks to ∼5.3 ks net exposure, each. The EPIC-MOS spectra have insufficient S/N for splitting them up further so for the spectral analysis we used only *NuSTAR* FPMA and FPMB and *XMM*-Newton EPIC-pn spectra, which we rebinned to a minimum S/N of 5 using the same channel and energy restrictions as those used in Sect. 5.3 for the time-averaged spectrum.'

'The spectra are of insufficient quality to warrant a detailed analysis based on the dust modeling discussed above. We therefore describe the spectra using the empirical `cutoffpl` model (Sect. 5.3). An initial modeling run shows that several parameters, in particular the photon index and the folding energy of the X-ray continuum did not vary significantly over the observation (Fig. 5.13 **(b)** and **(c)**). In subsequent modeling runs we therefore forced the detector cross-calibration constants, the emission line energies,

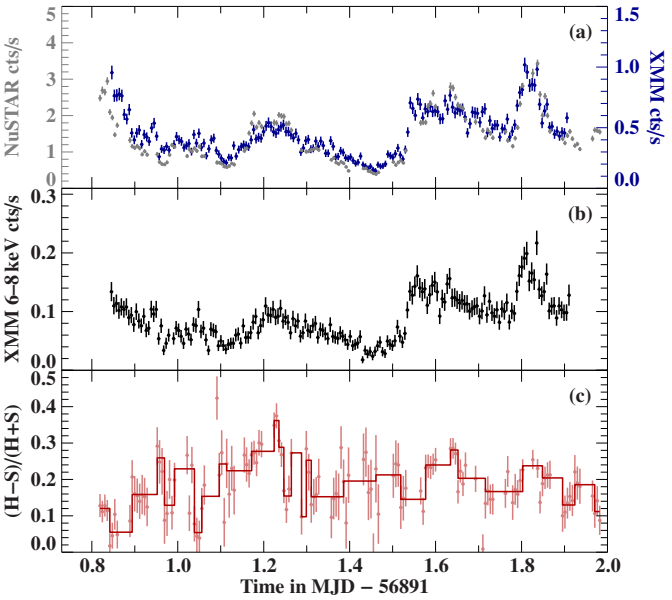

Fig. 5.12: **(a)** *NuSTAR* FPMA 3–80 keV (gray) and *XMM*-Newton EPIC-pn 0.2–15 keV (blue) light curve with 500 s time resolution. **(b)** *XMM*-Newton EPIC-pn light curve of the iron K band. **(c)** *NuSTAR* FPMA (H−S)/(H+S) hardness ratio of the 8–15 keV and 15–80 keV band. The solid line shows the result of a Bayesian block search which defines the time intervals for the time-resolved spectroscopy. Modified after Ballhausen et al. (2020).

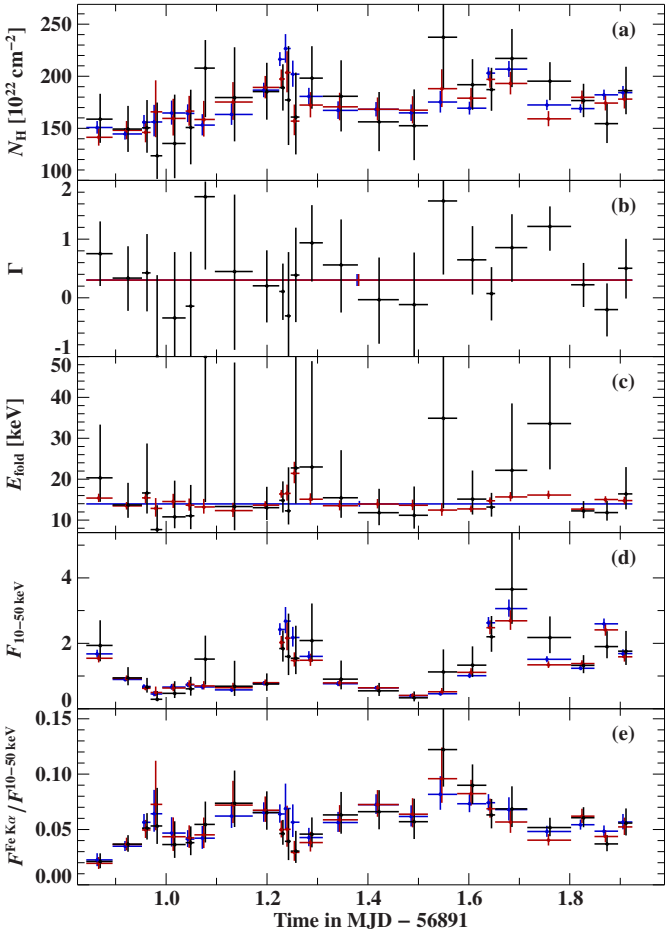

Fig. 5.13: Time-resolved spectroscopy of IGR J16318−4848. The figure shows the parameter evolution with time for the `cutoffpl` model. Panel (a) shows the equivalent hydrogen column density in units of 10^{22} cm^{-2}; panels (b) and (c) show the photon index and the folding energy in keV, respectively; panel (d) shows the unabsorbed continuum flux in units of 10^{-9} erg cm^{-2} s^{-1}; and panel (e) shows the line flux of the Fe Kα line divided by the continuum flux. Red and blue data points show fits where first Γ and then Γ and E_{fold} have been fixed, respectively. Modified after Ballhausen et al. (2020).

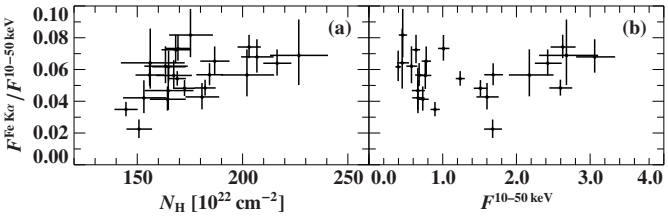

Fig. 5.14: Fe Kα flux ratio to the 10–50 keV continuum flux as function of N_{H} (a) and continuum flux (b). Modified after Ballhausen et al. (2020).

the iron abundance, the photon index (red data points in Fig 5.13), and finally also the folding energy of the continuum to be the same in all time intervals (blue data points in Fig 5.13), leaving only the continuum normalization, the column density, N_{H} and the iron line flux as free parameters. The evolution of the continuum parameters, continuum flux, and the ratio of the Fe Kα line flux to the hard continuum flux is shown in Fig. 5.13. This quantity represents information that is similar to the commonly used equivalent width, but is less affected by the continuum measurement at the line position, which is particularly difficult to constrain for this source. While the continuum flux varies by more than a factor of four throughout the observation, we find that the incident continuum shape stays constant within parameter uncertainties and that N_{H} and the Fe Kα flux ratio vary only moderately with time. We therefore consider it very unlikely that the results of our time-averaged analysis are affected by variability effects.

Finally, Fig. 5.14 shows the ratio of the Fe Kα flux to the continuum flux as a function of N_{H} and continuum flux. We find no correlation of the Fe Kα-to-continuum flux ratio with continuum flux, and only marginal variability of the Fe Kα flux with N_{H}. This behavior is in agreement with our simulations where at these optical depths of the absorber only a change in the column density by a factor of a few results in notable change in the observed fluorescence photon flux. The observed variability of N_{H} with time is, although large in absolute numbers, only ~30%.'

5.5 Discussion

We have presented a detailed analysis of the absorption and fluorescence features of the HMXB IGR J16318−4848. The main focus of this work is to investigate the possible presence of a dust absorber in order to resolve open questions raised by previous work using pure neutral gas absorption.

5.5.1 Neutral and ionized gas absorbers

'The *XMM*-Newton observations from 2003 showed already that IGR J16318−4848 is heavily absorbed with a column density on the order of 10^{24} cm^{-2}, and shows a very strong fluorescence line complex of iron and nickel. Subsequent observations were mainly modeled with an empirical cutoff power-law continuum with a neutral absorber and additional Gaussian emission lines. Recently, one of the few *Hitomi* observations

confirmed that the fluorescence lines are consistent with a neutral medium (Hitomi Collaboration 2018).

The profile of the iron Kα line is narrow, and previous authors give very low flux or only upper limits on the Compton shoulder flux, a spectral feature emerging from the reprocessing of the fluorescence photons by the Compton-thick absorber. In our empirical spectral analysis we are able to confirm this low Compton shoulder flux, the column density of $\sim 2 \times 10^{24}$ cm^{-2}, and the overall continuum shape. This empiric evidence led Matt & Guainazzi (2003) to the conclusion that the absorber is anisotropic and, more importantly, cannot have a covering fraction higher than 0.2–0.3. It is important to note that these and similar analyses by other authors treated the continuum absorption and fluorescence independently.

Aiming at a more self-consistent description of the absorbing medium we then compared the data to a grid of synthetic spectra using the photoionization code `XSTAR` for a wide range of covering fractions, ionization parameters, and column densities. Interestingly, a single gas absorber failed to provide an adequate description of the data. The Kα-to-Kβ flux ratio and the depth and structure of the absorption edge are very robust probes of the absorbing material, unlike the continuum absorption modeling process, which is systematically affected by the choice of the empirical incident continuum.

Although our fits of a single gas absorber are statistically not acceptable, they already indicate that covering fractions very close to 100% are necessary to reproduce the correct order of magnitude of continuum absorption and fluorescence line flux. This seems intuitively reasonable since at lower covering fractions significant leakage of the incident continuum will lower the line flux with respect to the continuum flux. The spectral shape below the iron K-edge is, however, completely dominated by the fluorescence lines and we do not see a significant contribution from the continuum. At the same time, high incident radiation is needed to produce the observed fluorescence flux in the first place. We therefore conclude that the covering fraction along the line of sight, despite the low Compton shoulder flux, has to be close to unity.'

5.5.2 Dust absorption and fluorescence

'To resolve the issue of the missing Compton shoulder and the very strong Fe Kα line and edge, we propose that a significant part of the X-ray absorption is due to dust and not to gas. This idea is also motivated by near IR observations of the system which suggest the presence of a significant amount of dust in the binary system (Moon et al. 2007, Chaty & Rahoui 2012). We further take into account that the dust not only contributes to the absorption, but that the physics of photo absorption also dictates that the absorber must be responsible for a part of the strong fluorescence emission line. We therefore implement a simple dust absorption model based on laboratory measurements of olivine absorption cross sections by Rogantini et al. (2018).

In our spectral modeling, we limit ourselves to an empirical estimate of the fluores-

cence yield of the dust absorber. Our dust absorption and fluorescence model assumes that the iron is confined in olivine dust grains for which both the K-edge depth and continuum absorption fit the data remarkably well, even though we note that fits with other dust models that are similarly enriched in iron might work equally well. In this fit, the total iron column is mainly constrained by the Fe K-edge depth, while the strength of the Fe Kα line encodes information about the geometry and about re-absorption probabilities of emitted photons.

In order to interpret this empirical estimate of the fluorescence yield in a physical way, we performed Monte Carlo simulations of the two extreme cases of spherical and slab absorber. We find that the spherical absorber reproduces the observed line strength well, whereas in the slab geometry too much fluorescence emission is scattered out of the line of sight to the observer.

In addition to the flux of the primary iron Kα fluorescence line, the Compton shoulder flux has raised questions about the structure and geometry of the absorber. We therefore include Compton scattering in our Monte Carlo simulation in order to compare the Compton shoulder flux ratio for a spherical dust absorber to the observational values. While the detailed value of the Compton shoulder flux ratio is still debated (e.g., Barragán et al. 2009 give only an upper limit, this work and Matt & Guainazzi 2003 find ~10%), all previous analyses agree that it is a factor of a few lower than expected from gaseous absorbers of the appropriate hydrogen column density of $\sim 2 \times 10^{24}\,\mathrm{cm}^{-2}$ (see, e.g., simulations by Matt 2002). Our simulations for a pure dust absorber produce a very weak Compton shoulder flux ratio that is only consistent with the upper limit by Barragán et al. (2009), but lower than the value of $11 \pm 4\%$ observed in our spectral analysis. This indicates that the simple picture of a pure dust absorber, while able to reproduce the absorption and primary fluorescence line correctly, is still incomplete as it does not provide an explanation of the flux of the Compton shoulder. It is, however, very plausible that the absorber also contains a gas component that has a minor effect on the total absorption, but would give rise to a Compton shoulder feature, although much weaker than if all the absorption were through gas. Comparing our observed Compton shoulder flux ration value to the simulations for spherical geometries by Matt (2002) we conclude that the hydrogen column density is on the order of $10^{23}\,\mathrm{cm}^{-2}$ assuming cold gas, similar to the average column density proposed by Matt & Guainazzi (2003). Such a low hydrogen column density cannot explain the strong continuum and iron edge absorption that can be resolved in the picture of an additional dusty absorber.

We note that these considerations assume a cold and neutral absorbing material. Scattering off a slightly warm plasma would significantly decrease the strength of the Compton shoulder (Odaka et al. 2016). Constraining the ionization state of the absorber is, however, not possible with the observations available to date since the existing *Hitomi* observation puts strong constraints only on the ionization of iron.'

5.5.3 Time-resolved spectroscopy

‘Our analysis of time-resolved spectra of constant hardness showed that the source mainly varies in flux on kilosecond timescales while the incident continuum shape shows no significant variation and the absorption column and the relative strength of the iron fluorescence line with respect to the hard continuum flux only vary moderately on longer timescales. Interestingly, the ratio of iron fluorescence line to continuum flux shows no distinct correlation with the absorption column or the flux. While the time-averaged spectrum is very nicely described by a homogeneous spherical dust absorber, the origin of the time variability remains an open question. Possible explanations include a structured and possibly anisotropic absorber, as suggested in previous works (e.g., Matt & Guainazzi 2003, Ibarra et al. 2007, Barragán et al. 2009) or a reprocessing structure with light-traveling times different from those probed in this observation.’

5.6 Conclusion

‘We presented a detailed study of the absorption and fluorescence properties, as well as the broadband spectrum and its time-variability, of the heavily absorbed HMXB IGR J16318−4848 with data taken by *NuSTAR* and *XMM*-Newton simultaneously. We showed that a single homogeneous gas absorber is not able to reproduce the observed absorption and fluorescence properties, independent of its ionization state. We also investigated the effect of a dust absorber on the observed spectrum, finding that a spherical homogeneous absorber of iron column density $N_{\mathrm{Fe}} = \sim 6\text{–}7 \times 10^{19}\,\mathrm{cm}^{-2}$ is consistent with the observations. Our time-resolved spectroscopy, however, indicates the presence of structures in the absorbing material since the absorption appears to be more variable than the incident spectrum.

In order to improve our understanding of HMXBs containing a significant amount of dust like IGR J16318−4848 we hope that our results will foster the development of more sophisticated dust absorption models that also include fluorescence processes. There are currently a few very advanced dust absorption models (e.g., `GGADT`; Hoffman & Draine 2016) used to calculate differential and total X-ray scattering cross sections for a specified grain using Anomalous Diffraction Theory, or `xscat` (Smith et al. 2016), which computes scattering cross sections for a population of dust grains as a function of the distance from the source and extraction region. However, neither of these advanced models includes treatment of the fluorescence from dust grains.

We studied the formation of a Compton shoulder with Monte Carlo simulations that are based on the best fit of our dust absorption model. The Compton shoulder flux produced by a pure dust absorber is even lower than observed in many of the earlier studies. A future step in the absorption modeling of this source will be the inclusion of an additional gas and self-consistent Compton shoulder component into the dust absorption model which is, however, beyond the scope of this work.

From an observational point of view, the *Hitomi* observation of IGR J16318−4848 is of exceptional value because it resolved the Fe Kα line with unprecedented quality and puts strong constraints on the ionization state of the absorber. We therefore expect high energy resolution instruments like the *Resolve* micro-calorimeter on board *XRISM* (Tashiro et al. 2018) to provide further insight into dust geometry and composition. Of particular interest will be any measurement of the X-ray absorption fine structure of the iron K-edge because it is a major diagnostic of the elemental composition and structure of the dust, which so far has been mainly studied through gratings observations in the L-edge band (e.g., Westphal et al. 2019) at an energy that is not accessible for IGR J16318−4848.'

There is a slight difficulty to be noted in consequence of the fact that there are two series of waves in sodium light [...] Among other substances tried in the preliminary experiments, were thallium, lithium, and hydrogen [...] It may be noted, that in the case of the red hydrogen line, the interference disappeared at about 15,000 wave-lengths, and again, at about 45,000 wave-lengths: so that the red hydrogen line must be a double line with the components about one-sixtieth as distant as the sodium lines.

— Albert A. Michelson & Edward W. Moreley, 1887

6 The accretion disk corona of Her X-1

This chapter focuses on the analysis of a set of four *XMM*-Newton observations spanning the turn-on phase of the superorbital variability of Her X-1. The observations were scheduled to reflect different perspectives of the accretion disk and its corona which are both irradiated by the accreting neutron star. A journal publication summarizing the results of this chapter is currently in preparation.

6.1 The neutron star and its disk

Her X-1 can be considered to be one of the "historic" X-ray binaries. Discovered with *UHURU* in 1972 it was the second X-ray pulsar[1] (Tananbaum et al. 1972) and the first source found to exhibit a Cyclotron Resonant Scattering Feature (CRSF) in its spectrum (Trümper et al. 1978). The binary system hosts a magnetized neutron star with a 1.24 s rotational period and an A/F-type optical companion (Crampton & Hutchings 1974). Due to the high inclination of the system of close to 90° (i.e., almost edge-on), the neutron star is eclipsed for ∼5.5 h during its 1.7 d orbit. Reynolds et al. (1997) estimate the distance of Her X-1 to be 6.6 ± 0.4 kpc.

Already at the discovery of Her X-1 and its X-ray pulsations, another, superorbital periodicity has been detected: Tananbaum et al. (1972) state, that they "have observed

[1]The first discovered X-ray pulsar was Cen X-3 (Giacconi et al. 1971). In addition, Oda et al. (1971) reported periodic pulsations in Cyg X-1 which turned out to be a black hole binary with variability on various timescales with the apparent pulsations having been an effect of red noise (see also Schreier et al. 1971). The famous Crab pulsar was detected as a very bright X-ray source already in 1964 (Bowyer et al. 1964), but pulsations had later been detected with radio observations (Staelin & Reifenstein 1968).

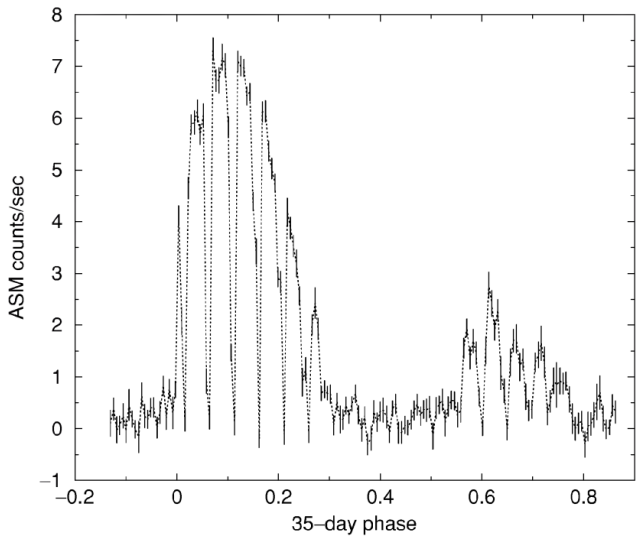

Fig. 6.1: *RXTE*/ASM average 35 d light curve of Her X-1 with main-on and short-on around phase 0.1 and 0.7, respectively. The eclipses are clearly visible as periodic dips in the light curve. Modified from Leahy (2002).

a longer-timescale cycle in which the source is bright and pulsing for approximately 9 days during which we can observe the 1.7 d occulting, followed by approximately 27 days during which the source is not detected above background on individual 20-s scans". These phases of high and low X-ray flux are commonly referred to as on-state and off-state, respectively. In particular, the on-state consists of a *main-on* and a *short-on* of ∼7 and ∼5 orbital periods duration, respectively, separated by an off-state of ∼4–5 orbital cycles (Staubert et al. 2009). Figure 6.1 shows the *RXTE*/ASM lightcurve folded on the 35 days superorbital period with clearly visible on- and off-states.

The superorbital variability is associated with a warped and tilted accretion disk that periodically blocks the line-of-sight (Gerend & Boynton 1976, Shakura et al. 1999, Wijers & Pringle 1999). The warping of the disk is supposed to be induced by coronal winds or radiation pressure (e.g., Petterson 1977b,c,a, Schandl & Meyer 1994, Schandl 1996, Maloney & Begelman 1997). The basic idea is that if the initially plain-parallel disk encounters a small deformation due to some instability it will experience an inhomogeneous irradiation by the central X-ray source. In particular, elevated parts of the disk are irradiated more strongly than those that are shadowed by the disk itself. The X-ray irradiation heats the disk locally and drives a disk wind. The repulsion of this wind then exerts a net torque on the disk that causes further warping until some equilibrium with viscous forces is reached. The properties of this disk have been studied in extensive *RXTE* monitoring campaigns (e.g., Scott & Leahy 1999, Scott et al. 2000, Leahy 2002). The warped disk is nicely reproduced by smoothed particle hydrodynamics simulations (see Fig. 6.2 and Foulkes et al. 2010).

The hard X-ray spectrum of Her X-1 has an exponentially cut-off powerlaw shape, typical for accreting neutron star binaries with a prominent CRSF around ∼35 keV (e.g., Staubert et al. 1978, Klochkov et al. 2008, Fürst et al. 2013). The soft X-ray

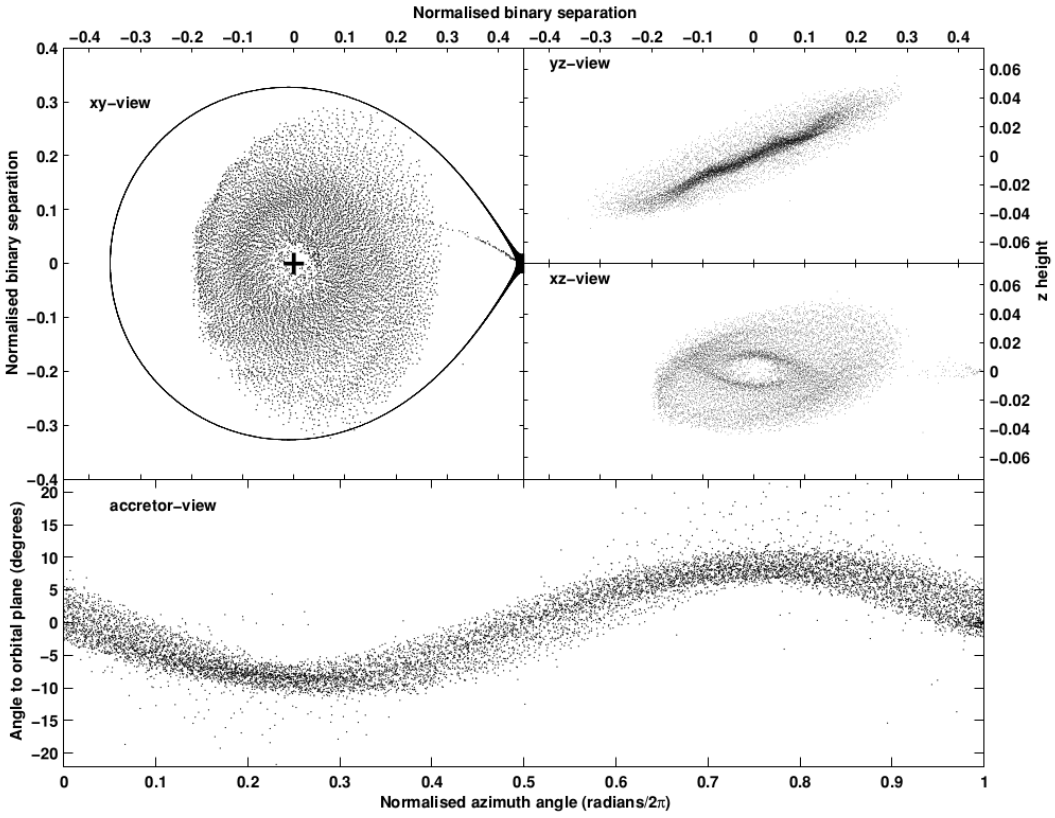

Fig. 6.2: Projection plots for smoothed particle hydrodynamics simulations for Her X-1. The *xy*-view shows the disk from above. The black cross and lobe show the position and Roche lobe of the neutron star. Modified from Foulkes et al. (2010).

spectrum is highly variable with superorbital phase and characteristically shaped by the partial covering geometry caused by the warped disk. Furthermore, it exhibits additional spectral features such as emission humps around 1 keV (e.g., McCray et al. 1982, Oosterbroek et al. 1997, Endo et al. 2000) and ~6.5 keV (e.g. Asami et al. 2014). High-resolution spectroscopy with *XMM*-Newton and *Chandra* revealed a wealth of emission lines, among them neutral and ionized Fe Kα as well as He- and H-like N, O, Ne, Mg, Si, and S (Ramsay et al. 2002, Jimenez-Garate et al. 2002a, 2005, Ji et al. 2009). These emission features have been associated with an accretion disk corona, a hot, optically thin layer sandwiching the disk. More recently, Kosec et al. (2020) report highly blueshifted emission lines and propose the presence of an ionized accretion disk wind.

This work builds on earlier *RXTE* analyses by Kuster et al. (2005) to probe the outer region of the accretion disk, this time using a series of *XMM*-Newton observations during the turn-on of the main-on when the disk gradually moves out of the line of sight

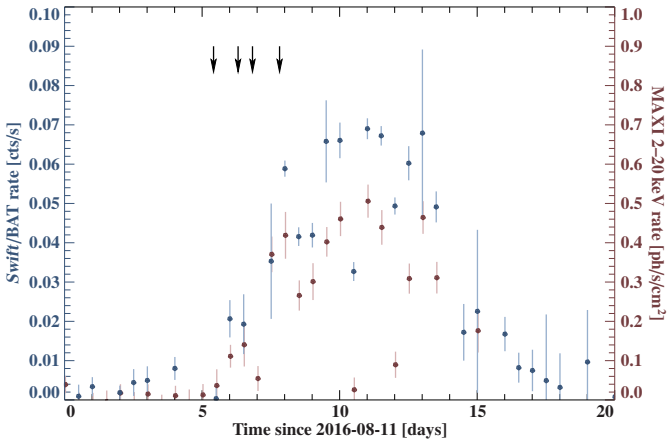

Fig. 6.3: *Swift*/BAT (blue) and MAXI (red) light curve with 0.5 d binning of the 2016 August turn-on of Her X-1. The vertical black arrows indicate the times of the *XMM*-Newton observations I–IV. Very low data points during the main-on are mostly due to eclipses.

to the neutron star. Therefore, with progressing turn-on, the line of sight passes through different zones of the accretion disk and its corona.

6.2 Data aquisition and reduction

XMM-Newton performed five observations of the 2016 August turn-on of Her X-1 at consecutive ∼0.5 day intervals. Unfortunately, the second observation was lost due to a loss of telemetry packets at the ground station. Figure 6.3 shows the *Swift*/BAT and MAXI light curves with arrows indicating the times of the successful *XMM*-Newton observations. For the sake of brevity, in the remainder of this chapter Obs. I–IV refer to ObsIDs 0783770301, 0783770501, 0783770601, and 0783770701, respectively. Note that data from Obs. II–IV have also been used by Kosec et al. (2020) for a study of fast accretion disk winds. During the first observation, EPIC-pn was operated in small window imaging mode, all later observations were performed in timing mode. During all observations, EPIC-MOS1 was operated in imaging mode and EPIC-MOS2 in timing mode. We applied standard calibration and screening criteria using SAS version 18.0.0. We exclude EPIC-MOS1 from our spectral analysis because we found it to be severely affected by pile-up. For the other instruments, source and background regions are defined as follows: For Obs. I, source and background regions of EPIC-pn are circles of 32″ radius centered on and off the source, respectively. For EPIC-pn in Obs. II–IV, we choose columns 26–47 as source region and 20 columns outside the PSF wings as background regions. For EPIC-MOS2 in Obs. I–IV, the source region are columns 282–322 and we measure the background in 10 columns at the outer regions of the detector. After inspection of the event pattern distributions and also the spectral shape for different extraction regions, we suspect only Obs. IV to be moderately affected by pile-up in EPIC-pn and -MOS2, so we exclude the three boresight columns in EPIC-pn and eight columns in -MOS2. We combine both first order spectra of RGS1 and RSG2 using the SAS tool `rgscombine`.

Furthermore, we find high variability in the light curves of some of the observations, the most extreme case is the binary eclipse during a part of Obs. III. We therefore apply additional time filtering for all instruments. The light curves of all observations with indicated time intervals used for spectral extraction are shown in Appendix B. We rebin all datasets according to the "optimal binning" scheme proposed by Kaastra & Bleeker (2016) and use C-statistics (Cash 1979). The energy ranges used for spectral fitting are 0.8–10 keV for EPIC-pn and -MOS2 and 0.3–2 keV for RGS. We further allow for an additive gainshift for EPIC-pn to account for uncertainties in the CTI correction at high count rates.

6.3 Spectral analysis

6.3.1 Continuum modeling

Both, as a baseline for our subsequent line analysis and to investigate changes in the absorber geometry with superorbital phase, we first model the continuum emission from Her X-1 over the turn-on. We follow the approach outlined by Kuster et al. (2005), where the total, observed spectrum consists of a primary (direct) component that is only absorbed by cold or at most mildly ionized material along the line-of-sight, a second component of the incident radiation that is (Thomson-)scattered by the ADC into the line-of-sight to the observer, and a third component that originated in the ADC itself. Since the accretion disk provides a rather steady accretion flow we further assume that the incident luminosity and also spectral shape do not change over the course of the turn-on and that the observed spectral variability is a result of relative changes of these individual components due to changes as the accretion disk moves out of the line of sight to the observer. A schematic illustration of the disk and its corona with the individual spectral components evolving with turn-on phase is shown in Fig. 6.4. Due to the warped shape of the outer disk, the superorbital rotation will effectively cause different viewing angles onto the disk and its corona. At the beginning of the turn-on, the warped outer rim of the accretion disk blocks the line of sight to the neutron star. Any radiation from the neutron star reaching the observer directly is therefore strongly absorbed. Radiation scattering in the accretion disk corona into the line of sight, however, will be observed with the incident spectral shape but with lower flux depending on the efficiency of the scattering. An atmospheric component, e.g., from recombination processes in the ADC will always be observed. As the turn-on progresses, the disk rim moves out of the line of sight, causing a gradual decrease of the effective absorption of the primary component. At the end of the turn-on the disk opens the line of sight to the observer. The spectrum is dominated by the primary, now unabsorbed, component. The scattered component may still be present but cannot be distinguished from the primary (and is therefore omitted in Fig. 6.4), because both have the same spectral shape. The atmospheric component may evolve moderately with turn-on phase, depending on its exact geometry.

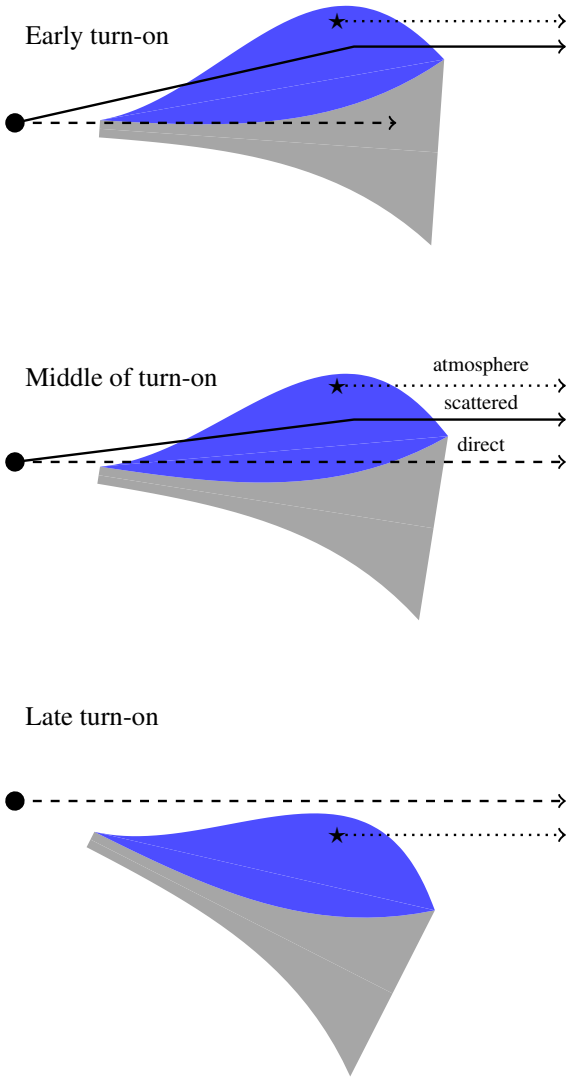

Fig. 6.4: Accretion disk (gray) and corona (blue) geometry during the turn-on adopted from Kuster et al. (2005, Fig. 2). As the turn-on progresses, the disk moves out of the line of sight, causing a relative change of the direct (dashed), scattered (solid), and atmosphere component (dotted). At the beginning of the turn-on, the neutron star is still obscured by the outer rim of the accretion disk. Incident radiation that is scattered in the ADC, as well as radiation originating in the ADC can still reach the observer. With progressing turn-on, the effective absorption by the disk decreases and the direct component becomes visible. Toward the end of the turn-on, the disk has moved out of the line of sight completely and the spectrum consists of the unabsorbed primary and the atmospheric component.

The primary and the scattered components originate from the same incident continuum but experience different absorption column densities on their way to the observer. The formation of the total spectrum therefore resembles a partial covering situation with the cross-normalization of its components being free to vary over the superorbital phase (this is connected to our assumption that the incident luminosity remains constant). We find an incident powerlaw with an additional blackbody to provide a satisfactory description of the data, as is typical for accreting neutron star binaries and an established continuum model for Her X-1 (e.g., Fürst et al. 2013, Asami et al. 2014). The third, atmospheric component mostly contributes emission features which we model with two narrow and

two broad Gaussian emission lines. In `xspec`-like notation, our complete spectral model is therefore given by

$$S(E) = \underbrace{f_{\mathrm{prim}} \times \texttt{cabs} \times \texttt{tbabs} \times \texttt{continuum}}_{\text{primary component}} + \underbrace{f_{\mathrm{scat}} \times \texttt{continuum}}_{\text{scattered component}} + \underbrace{4 \times \texttt{egauss}}_{\text{atmosphere component}} \quad ,$$

where `continuum` = `powerlaw` + `bbody` and the four Gaussians model the 1 keV hump, a broad emission component around 6.5 keV and the complex of neutral and ionized iron lines. We fit all four observations simultaneously requiring the photon index, blackbody temperature, and the center and width of the 1 keV hump to be the same in all observations. The incident flux which we assume to be constant in all observations is constrained by Obs. IV. The normalization constants of the primary and scattered component, f_{prim} and f_{scat}, therefore carry information about the relative normalization of the components with respect to each other as well as the total flux compared to Obs. IV. After several preliminary fits, we find that Obs. IV shows no significant absorption. Note that, due to the negligible absorption in Obs. IV, f_{prim} and f_{scat} are degenerate and we choose $f_{\mathrm{prim}} = 1$ by definition. We also do not find evidence for the existence of the 6.5 keV feature in Obs. I. Figure 6.5 shows the spectra of all four observations with the best-fit model, ratio, and Cash residuals.

We find a wealth of narrow lines resolved in the RGS that we do not include in our continuum model and which contributes heavily to the final C-statistic of 8158.8 for 4127 degrees of freedom (red. Cash of 1.98). The data/model ratio, however, confirms that the continuum shape is well described by our model. The best-fit parameters are listed in Table 6.1. Note that the parameters f_{prim} and f_{scat} that scale the primary and the scattered component with respect to each other and to the incident flux are, however, not representative of the spectral energy flux that each component contributes, as the flux of the primary component is reduced by the energy-dependent absorption. Figure 6.6 therefore shows the νF_ν spectral energy flux density of the primary, scattered, and atmospheric component for all observations.

6.3.2 He-like triplets

We detect strong emission lines of the He α triplets (resonance, r, intercombination, i, and forbidden line, f; see also Sect. 3.5) of N VI, O VII, and Ne IX which we model with narrow, Gaussian emission lines. We account for a possible redshift, individual for each observation but identical for each ion. We use only a narrow energy range of 100 eV around each triplet to fit the line fluxes and also leave the continuum parameters free to improve the continuum modeling locally around the triplets. Figures 6.7–6.9 show close-ups of the triplets of N VI, O VII, and Ne IX, respectively, for Obs. I–IV.

Striking at first glance is that all triplets of all observations are characterized by a very prominent intercombination line and only very weak to absent forbidden and

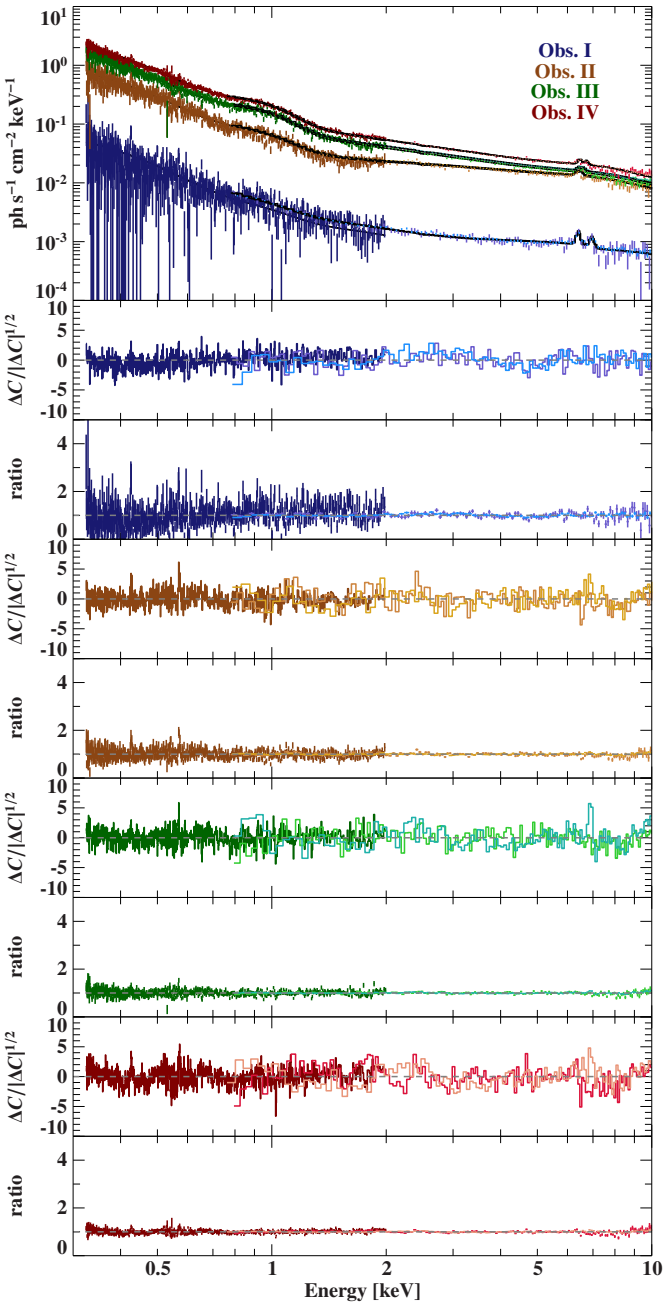

Fig. 6.5: Photon spectra of Obs. I–IV in blue, brown, green, and red, respectively, with best-fit model (black). The lower panels show Cash and ratio residuals. Light, medium and dark colors show EPIC-pn, EPIC-MOS2 and RGS data, respectively.

recombination lines. Consequently, we can only put lower and upper limits on G and R, respectively. In order to account for the statistical uncertainties of the ratios correctly in the limit of very low line fluxes, we fit R and G directly along with the absolute flux of the intercombination line. The fit parameters for R, G, and the absolute intercombination line flux are listed in Table 6.2.

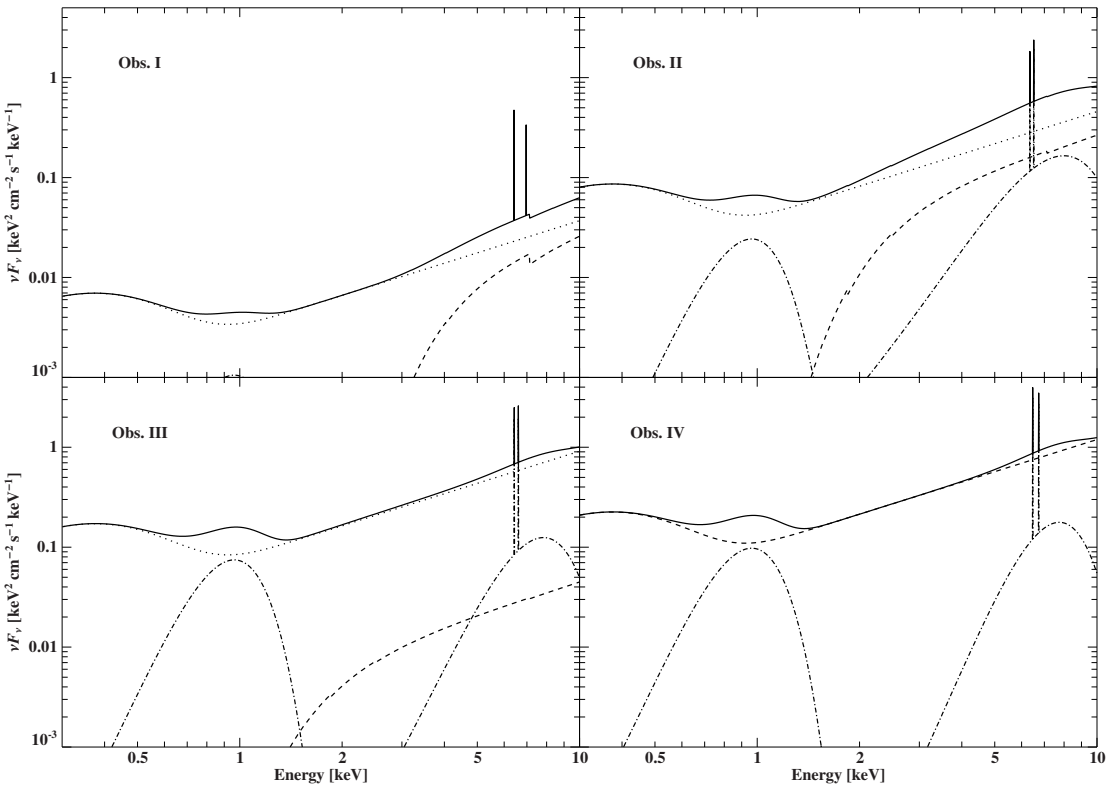

Fig. 6.6: Total νF_ν spectral energy flux density (solid line), as well as individual primary (dashed line), scattered (dotted line), and atmospheric (dotted-dashed line) component for all observations.

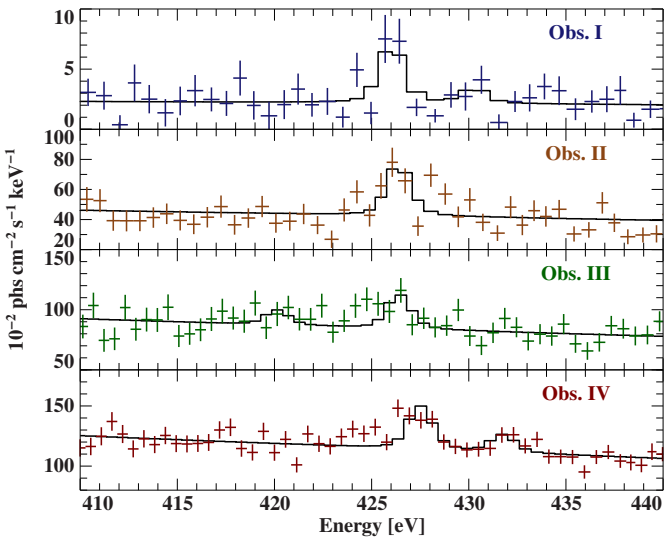

Fig. 6.7: Close-up of RGS spectrum of He-like triplet of N VI.

Table 6.1: Best-fit parameters for the continuum model. Global parameters were free during the fit but required to be the same in all observations.

Parameter	Obs. I	Obs. II	Obs. III	Obs. IV
$N_{\rm H}{}^{a}$	28^{+5}_{-4}	5.2 ± 0.5	$2.4^{+1.1}_{-0.8}$	–
$f_{\rm prim}$	$0.033^{+0.004}_{-0.003}$	0.240 ± 0.021	0.039 ± 0.011	1
$f_{\rm scat}$	0.031 ± 0.001	$0.383^{+0.006}_{-0.005}$	0.764 ± 0.008	–
$F_{\rm 1\,kev\text{-}hump}{}^{b}$	$(8.5 \pm 0.8) \times 10^{-4}$	0.020 ± 0.001	0.060 ± 0.002	0.079 ± 0.002
$F_{\rm 6.5\,kev\text{-}hump}{}^{b}$	–	0.152 ± 0.026	0.099 ± 0.012	0.133 ± 0.016
$E_{\rm 6.5\,kev\text{-}hump}{}^{c}$	–	6.88 ± 0.12	$7.12^{+0.10}_{-0.09}$	7.15 ± 0.09
$\sigma_{\rm 6.5\,kev\text{-}hump}{}^{c}$	–	$2.10^{+0.24}_{-0.23}$	$1.66^{+0.16}_{-0.15}$	$1.51^{+0.12}_{-0.13}$
$E_{\rm Fe\,I}{}^{c}$	6.41 ± 0.02	$6.34^{+0.08}_{-0.04}$	$6.42^{+0.03}_{-0.02}$	$6.47^{+0.01}_{-0.04}$
$A_{\rm Fe\,I}{}^{d}$	1.19 ± 0.15	$3.5^{+1.9}_{-1.2}$	$5.0^{+0.9}_{-0.8}$	8.4 ± 1.0
$E_{\rm Fe\,XXIV}{}^{c}$	$6.96^{+0.03}_{-0.04}$	$6.51^{+0.09}_{-0.04}$	$6.60^{+0.04}_{-0.02}$	$6.73^{+0.02}_{-0.03}$
$A_{\rm Fe\,XXIV}{}^{d}$	0.74 ± 0.15	$4.8^{+0.9}_{-1.2}$	$5.0^{+0.8}_{-0.7}$	6.7 ± 1.0
		Global parameter		
Γ		0.93 ± 0.01		
kT		0.091 ± 0.001		
$F_{\rm PL}{}^{b}$		1.293 ± 0.015		
$F_{\rm BB}{}^{b}$		0.076 ± 0.002		
$E_{\rm 1\,keV\text{-}hump}{}^{c}$		0.882 ± 0.005		
$\sigma_{\rm 1\,keV\text{-}hump}{}^{c}$		$0.1974^{+0.0028}_{-0.0027}$		
		Detector constants		
$c_{\rm MOS}$	0.978 ± 0.015	0.957 ± 0.007	0.924 ± 0.005	1.003 ± 0.005
$c_{\rm RGS}$	0.781 ± 0.021	$0.943^{+0.011}_{-0.012}$	$0.956^{+0.008}_{-0.007}$	0.991 ± 0.006
$\rm EG_{PN}{}^{e}$	4 ± 13	26 ± 6	$9.5^{+3.2}_{-3.0}$	$5.9^{+3.0}_{-2.8}$

Notes. [(a)] In $10^{22}\rm cm^{-2}$. [(b)] 3–10 keV flux in $10^{-9}\rm erg\,s^{-1}\,cm^{-2}$. [(c)] In keV. [(d)] In $10^{-4}\rm phs\,s^{-1}\,cm^{-2}$. [(e)] Additive gainshift in eV.

6.4 Discussion

6.4.1 Evolution of the continuum with turn-on phase

We find a steady decrease of $N_{\rm H}$ in the primary component with progressing turn-on phase with an overall decrease of this component with respect to the unabsorbed (i.e., scattered) one as expected for the rim of the warped accretion disk moving out of the line of sight. As Her X-1 is a frequently observed and well studied source, several analyses

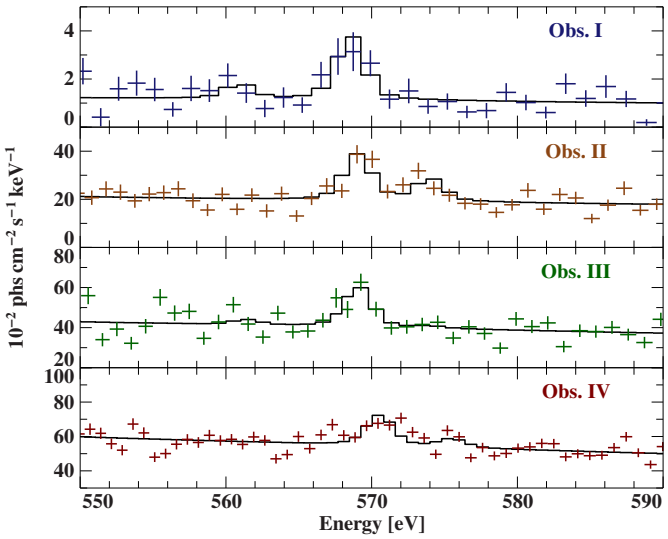

Fig. 6.8: Close up of RGS spectrum of He-like triplet of O VII.

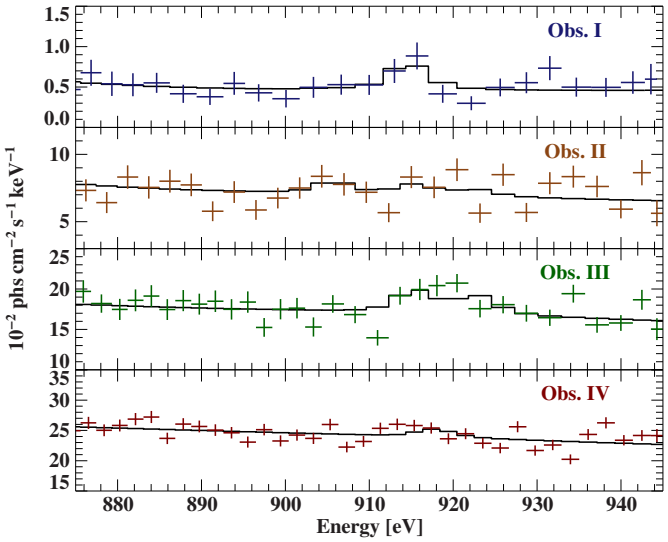

Fig. 6.9: Close up of RGS spectrum of He-like triplet of Ne IX.

of the properties of the X-ray continuum that are reported in the literature address the absorption column density at different superorbital phases. The observations used here, however, provide the first close monitoring of the turn-on in a single superorbital cycle in the soft X-ray band.

The column density in Obs. I is similar to those reported by Ji et al. (2009) during the turn-on. However, they also observe higher absorption columns during other superorbital phases. Asami et al. (2014) report a wide range of $N_{\rm H}$ values for different superorbital phases and continuum models that are, however, difficult to compare to our results. Only two of their seven observations were taken during the turn-on and those were fitted with an ionized partial covering model for a powerlaw continuum and a neutral absorber for

Table 6.2: Limits and best-fit values of R, G, the absolute flux of the intercombination line and redshift for N VI, O VII, and Ne IX.

Parameter	Obs. I	Obs. II	Obs. III	Obs. IV
$R_{\mathrm{N\,VI}}$	$5 < 10^{-5}$	$< 2 \times 10^{-4}$	$< 1 \times 10^{-3}$	$< 2 \times 10^{-4}$
$R_{\mathrm{O\,VII}}$	$8 < 10^{-5}$	$< 1 \times 10^{-4}$	$< 4 \times 10^{-4}$	$< 7 \times 10^{-5}$
$R_{\mathrm{Ne\,IX}}$	$4 < 10^{-6}$	$< 2 \times 10^{-4}$	$< 9 \times 10^{-5}$	$< 5 \times 10^{-5}$
$G_{\mathrm{N\,VI}}$	$1.4 <$	$4.0 <$	$5.9 <$	$2.4^{+2.8}_{-1.0}$
$G_{\mathrm{O\,VII}}$	$7.0 <$	$2.0^{+1.8}_{-0.8}$	$3.9 <$	$2.0 <$
$G_{\mathrm{Ne\,IX}}$	$3.9 <$	< 0.3	$1.2^{+3.5}_{-0.3}$	$1.7 <$
$A^{i\ a}_{\mathrm{N\,VI}}$	$1.0^{+0.5}_{-0.4}$	$6.8^{+2.3}_{-2.2}$	$5.7^{+2.5}_{-2.3}$	$7.3^{+1.8}_{-1.7}$
$A^{i\ a}_{\mathrm{O\,VII}}$	$0.9^{+0.4}_{-0.3}$	6.3 ± 1.6	$6.6^{+1.8}_{-1.7}$	5.7 ± 1.2
$A^{i\ a}_{\mathrm{Ne\,IX}}$	0.3 ± 0.2	$0.7^{+1.1}_{-0.8}$	$2.6^{+1.5}_{-1.1}$	1.2 ± 1.0
z^b	$\left(4^{+6}_{-5}\right) \times 10^{-4}$	$(-5 \pm 4) \times 10^{-4}$	$\left(-5^{+9}_{-6}\right) \times 10^{-4}$	$(-3.1 \pm 0.4) \times 10^{-3}$

Notes. $^{(a)}$ Photon flux of the intercombination line in 10^{-4} phs s^{-1} cm^{-2}. $^{(b)}$ Redshift.

an NPEX[2] continuum with an additional blackbody. The column density of the ionized absorber is much higher than our neutral absorber, but Asami et al. (2014) find ionization parameters of $\log \xi \sim 2.1$–2.3, which effectively make the absorber more transparent, especially at low energies. Their NPEX model does not require absorption to fit the data but very possibly there is interference of the blackbody component with the additional soft NPEX component which makes a quantitative interpretation of absorption in such a model very difficult. An interesting aspect of the wide range of observed column densities also at similar superorbital phases in the past is the indication of dynamic variability in the disk itself which we observe as short-term variability of the X-ray light curves but which is also supported by the observation of stochastic variations of the turn-on times (see, e.g., Leahy & Igna 2010).

The decomposition of the individual spectral components shown in Fig. 6.6 also shows that the broadband spectral shape of Obs. I is very similar to the incident spectrum. This indicates, as expected, the dominant role of Thomson scattering to the spectral formation at this superorbital phase, which redirects a small fraction of the incident radiation with little to no energy dependence. The high column density of $\sim 3 \times 10^{23}$ cm^{-2} effectively adds a hard excess around 4–10 keV, similar to the 6.5 keV feature in energy but different in shape.

The enigmatic broad emission features at 1 keV and 6.5 keV (we follow this terminol-

[2]The NPEX continuum model (Mihara 1995) is an empirical continuum model sometimes used for accreting neutron star. It consists of two broken powerlaws, one with a negative photon index to model a soft excess.

ogy for consistency with the literature although we observe this feature rather around ~7 keV) evolve differently over the course of the turn-on. While the centroid energies of both features are remarkably stable, the flux of the 1 keV feature increases over the turn on, whereas the 6.5 keV hump is not required in Obs. I but then its flux appears independent of the total flux in Obs. II–IV. Asami et al. (2014) discuss several possible origins of the 6.5 keV hump; unfortunately none of which offers a very plausible explanation: Line blending of different ionization states of iron, broadening by Comptonization in the ADC or Doppler at the inner accretion disk are unlikely to produce emissions features much wider than ~300 eV. Doppler broadening from the accretion flow may explain the observed width of the 6.5 keV feature but should generally result in lower fluxes.

The most debatable assumption in our spectral model is the neutral disk, as the RGS spectra also show absorption lines of highly ionized ions (see also Sect. 6.4.3). In the geometrical picture of the disk and ADC proposed here, the formation of these ionized absorption features is supposed to happen in the accretion disk atmosphere and corona while the bulk of the disk – due to its high optical depth – remains not or at most lowly ionized. Considering the unknown shape of the warped, outer rim of the accretion disk and its irradiation by the neutron star, however, a certain degree of ionization of parts of the disk with moderate optical depth cannot be excluded and in fact, an alternative explanation of the emission features that is also discussed in the literature (e.g., Asami et al. 2014) is an ionized partial covering absorber. Given the complex multi-component spectra, such an additional ionized absorption component with a large range of possible ionization states, covering fraction, abundances and geometry is, however, very difficult to constrain without additional empirical evidence or strong simplifying assumptions.

In addition to the large width of ~1.5–2 keV of the 6.5 keV feature, we observe its centroid at higher energies than Fe XXVI Lyα, thus ruling out pure ionization effects without any broadening or Doppler shifts. The absence of this component in Obs. I and its similarity in Obs. II–IV further suggests that the region of its origin may still be obscured by the accretion disk at very early phases of the turn-on but that its visibility remains rather constant later on.

The 1 keV feature has been attributed to unresolved L-shell transitions (e.g., McCray et al. 1982, Oosterbroek et al. 1997, Endo et al. 2000, Oosterbroek et al. 2000, Asami et al. 2014) although its exact nature is still under debate. A collisionally ionized plasma with temperatures around 0.5–1 keV produces a series of emission lines around 1 keV as illustrated in Fig. 6.10. While there is strong empirical evidence for the presence of a photoionization-dominated plasma in Her X-1 (e.g., Jimenez-Garate et al. 2002a), the assumption of a single ionization regime and structure is still strongly simplified and a hybrid plasma with multiple components is quite plausible. In fact, Jimenez-Garate et al. (2002b) and Jimenez-Garate et al. (2005) argue for a complex accretion and absorber geometry, consisting of the accretion disk, an accretion disk atmosphere, and the presence of both, a compact and an extended ADC.

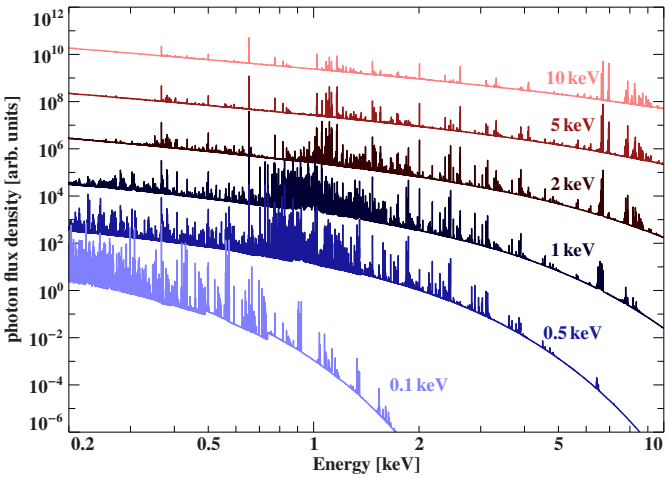

Fig. 6.10: Evaluations of the collisional plasma model `APEC` (Smith et al. 2001) for different plasma temperatures.

Interestingly, we find that the centroid energy and width of the 1 keV feature are so stable that they can be kept constant throughout all observations; only its flux increases steadily with progressing turn-on phase. This behavior indicates a region of origin independent of the turn-on but affected by obscuration by the outer region of the accretion disk. Although we label this component as "atmospheric" in our schematic depiction of the continuum formation, it may also well be connected to the inner region of the accretion disk or the accretion flow. An origin in the extended ADC is rather unlikely since it is supposed to cover quite a large solid angle and thus not vary strongly with disk precession.

6.4.2 Interpretation of He-like triplets

Her X-1 is a well-studied source and previous observations with *XMM*-Newton and *Chandra* have already provided evidence of emission lines from He-like triplets. The strongest He α triplets are generally observed during off-states and are therefore associated with an ADC. During short- and main-on, the emission lines tend to be overshone by the continuum and less resolved (e.g., Jimenez-Garate et al. 2002a). In agreement with previous observations (e.g., Ji et al. 2009), we also find that the He-like triplets are characterized by strong intercombination lines and very weak forbidden and resonance lines. For some elements and observations, only upper limits on the line fluxes can be given. Note that while the flux ratios R and G of these lines are generally reliable probes of plasma properties, density estimates are based on the assumption that there is only a weak UV field, such that photo-excitation of $^3S_1 \rightarrow ^3 P_{1,2}$, competing with collisional excitation, is negligible. Estimates of the UV luminosity of Her X-1 are presented by various authors (e.g., Vrtilek et al. 1994, Anderson et al. 1994, Boroson et al. 1997, 2000) and Jimenez-Garate et al. (2002a) estimate the distance from the central source at which UV photoexcitation to $^3P_{1,2}$ balances radiative de-excitation of the $^3S_1$ state

(i.e., formation of the forbidden line) to be of the order of $\sim 10^{11}$–10^{12} cm (depending on the ion). The weak forbidden lines, and consequently low values of R that we observe throughout all our observations therefore generally indicate electron densities larger than 10^{13} cm^{-3} or distances closer than a few times 10^{11} cm of the line forming region to the UV source.

The weak resonance line, however, is not expected from recombination processes alone. In photoionized plasmas with temperatures insufficient for efficient collisional excitation and di-electronic recombination, the $^1P_1$ state, as well as the $^3P_{1,2}$ and $^3S_1$ states are populated predominantly by radiative recombination which is rather insensitive to the plasma temperature. Porquet & Dubau (2000) find that in this regime G is ~4.5–5 for N VI, O VII, and Ne IX. Only at temperatures of 10^5–10^6 K and higher, G decreases significantly because of competing di-electronic recombination and collisional excitation. However, G is never expected to be much greater than ~5 because of a certain minimal population of $^1P_1$ compared to the other states according to their statistical weights and photoionization cross sections.

The weak resonance line in Her X-1 is therefore most likely rather an effect of the ADC geometry than of plasma properties (Jimenez-Garate et al. 2005, see also Wojdowski et al. 2003 for discussions of an enhancement of the resonance line in Cen X-3 due to scattering). The oscillator strength of the resonance transition is orders of magnitudes higher than those of the intercombination and forbidden transitions, rendering resonance line photons also subject to significant scattering by radiative excitation and subsequent de-excitation. In a spherical symmetric plasma which is a standard assumption in model calculations of R and G, resonant scattering, even if occurring frequently, has no net effect. In a highly asymmetrical geometry, however, scattering of resonance line photons may become important even if the plasma is optically thin for continuum photons. In particular, in an ADC that is still thin compared to its radius and that is observed nearly edge-on, a significant amount of resonance line photos may be scattered out of the line of sight because of the higher optical depth in the accretion disk plane. Interpreting G values as measure of temperature might therefore be misleading in an accretion disk geometry.

6.4.3 Further plasma diagnostics

Since geometrical effects limit the physical interpretation of R and G, additional diagnostic parameters are required for constraining physical properties of the accretion disk, its atmosphere and its corona. As an alternative to using G, temperature estimates can also be inferred from Radiative Recombination Continua (RRCs) where the relative width $\Delta E/E \approx kT/I$, in the limit $kT \ll I$, where I is the ionization potential of the recombining ion (Liedahl & Paerels 1996). Jimenez-Garate et al. (2002a) and Jimenez-Garate et al. (2005), employ this relationship and derive plasma temperatures of ~2–6 eV of the RRCs of N VII and O VII. Furthermore, information about the density is also encoded in

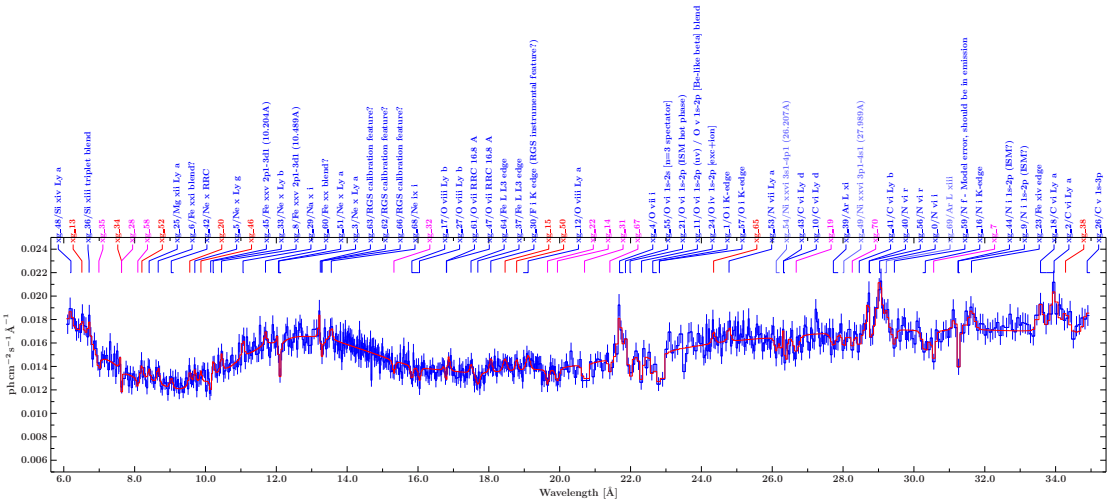

Fig. 6.11: Preliminary line identification in the RGS spectrum of Obs. IV (J. Wilms & M.A. Nowak, priv. comm.).

the ionization structure, as the ionization parameter ξ is a function of luminosity, density and geometry (i.e., size of the irradiated plasma, see also Eq. 3.15). The ultimate, though very challenging, goal therefore has to be a self-consistent modeling of the ionization structure and ADC geometry, based on the continuum absorption and the many individual absorption and emission lines. Figure 6.11 shows an automated line search based purely on statistical criteria with a preliminary identification of most probable transitions for Obs. IV (J. Wilms & M.A. Nowak, priv. comm.).

Condoning the caveats outlined in Sect. 3.4.1 we attempt to reproduce the series of absorption lines of Obs. IV shown in Fig. 6.11 with the `warmabs` model where we choose ion populations for a density of $10^{12}\,\mathrm{cm}^{-3}$ as best estimate from the weak forbidden lines in the He-like triplets. Even after extensive fitting we do not find a satisfactory global description of the majority of absorption lines with a single `warmabs` absorber. We illustrate this on the example of absorption lines of H-like ions of oxygen and neon (see Fig. 6.12). The O VIII Lyα line is very weak while the Ne X Lyα is quite prominent. Since H-like ionization states of oxygen are already produced at slightly lower values of $\log\xi$ compared to neon, the absence of the O VIII Lyα absorption line indicates an ionization balance toward full ionization of oxygen and therefore qualitatively rather puts a lower limit on $\log\xi$. However, due to their proximity in Z, oxygen and neon still have similar ionization thresholds (see, e.g., Hanke 2011, Fig. 1.15, for an illustration of the ionization balance in the `warmabs` model as a function of $\log\xi$) and we do not find a single $\log\xi$ that sufficiently produces Ne X while at the same time depleting O VIII.

The failure of the `warmabs` model is therefore by no means unexpected nor does it limit the physical interpretation of the absorption spectra. It is rather a confirmation of the picture of a complex absorber with several components of different ionization

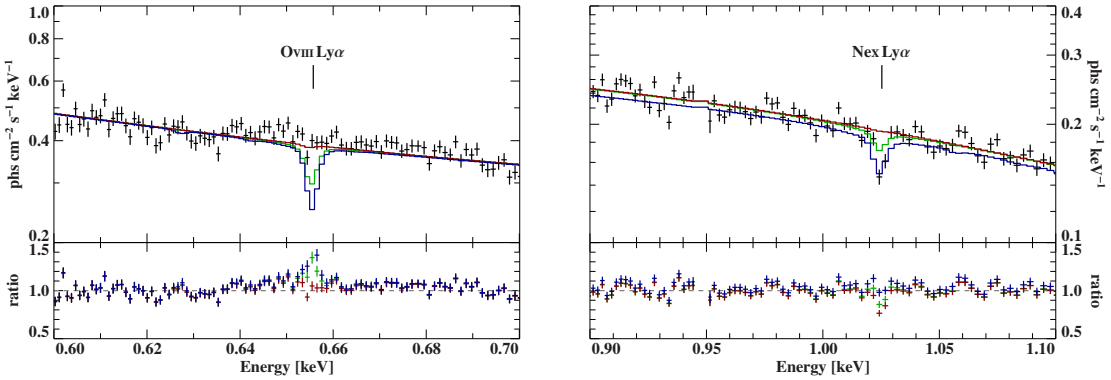

Fig. 6.12: RGS spectrum of Obs. IV with a `warmabs` model with $N_{\rm H} = 10^{24}$ cm^2 and $\log \xi = 3.5$ (blue), $\log \xi = 4$ (green) and $\log \xi = 5$ (red). The lower ionized model reproduces the Ne x Lyα absorption line, but also a strong O VIII line which is not observed. At even higher ionization parameters, a large fraction of oxygen gets fully ionized and the model line gets weaker. This model, however, also under-predicts the neon absorption line. The intermediately ionized model reproduces neither of the lines correctly.

parameters, or an ionization gradient, with both scenarios likely to occur in Her X-1 but not accounted for by standard, pre-calculated ionization models.

6.5 Conclusions

We have presented the spectral analysis of a series of *XMM*-Newton observations densely monitoring the turn-on phase in Her X-1. Unfortunately, the second of the originally performed five observations which covered the crucial moment of the accretion disk opening up the line of sight to the observer was lost during downlink. In the remaining four observations we studied the evolution of the continuum but also characteristic atomic lines.

We observe a complex, multi-component continuum whose temporal evolution is well described by the varying superposition of a strongly absorbed and an unabsorbed component that is consistent with the picture of the accretion disk moving out of the line of sight. Additionally observed spectral components are two broad emission features around ~1 keV and ~6.5–7 keV, respectively. While unresolved iron L-shell transitions offer a qualitative explanation of the ~1 keV feature that is also frequently discussed in the literature, the origin of the ~6.5 keV feature remains more enigmatic. Several possible mechanisms are discussed, e.g, by Asami et al. (2014) but none of which is strikingly convincing. While we find that with this empirical emission feature, a neutral absorber modeling the disk provides a satisfactory description of the observed spectra, there are also clear signatures of ionized absorption lines in the RGS spectra. Even mild ionization will have a significant effect on the continuum absorption that, despite the challenges of fitting ionized absorption, certainly deserves further exploration.

In addition to the continuum evolution, we observe, among other characteristic atomic

features, He α triplet lines of N VI, O VII, and Ne IX in the RGS spectra. In agreement with previous observations, the triplet lines are characterized by a prominent intercombination line and very weak resonance and forbidden lines. The line ratios of these triplets, in general good indicators of density and temperature, are only of limited diagnostic power in Her X-1 because of the asymmetrical absorber geometry and possible UV field contamination. Reliable constraints of plasma properties therefore require the careful consideration of the collective ensemble of absorption and fluorescence lines that already indicate a multi-component or structured plasma. The presence or absence of atomic lines of elements of similar Z, for example, that would otherwise be expected to form at similar conditions or the fact that the He α triplets are generally observed in emission while the Lyα lines of the same elements are in absorption. As expected, single ionized absorption models therefore fail to provide an adequate description of the atomic lines. A next step will have to be to construct a plasma model with multiple components of different ionization parameters, or an internal ionization structure including geometrical effects due to the anisotropy of the plasma. Additional observable quantities like differential emission measures (e.g., Ji et al. 2009) or line ratios of different ionization states may help in constraining the wide parameter space of any advanced ionized absorption model.

Essentially, all models are wrong, but some are useful.

— George Box, 1987

7 Conclusions & Outlook

This thesis presents results of the spectroscopic analysis of IGR J16318−4848 and Her X-1 with a focus on the absorption and reprocessing of the X-ray radiation generated by direct mass accretion by the circumstellar and circumbinary material. Despite both being X-ray binaries with (probable) neutron star accretors, the two sources show very different behavior regarding their X-ray absorption and fluorescence.

In IGR J16318−4848 we aim for a self-consistent model of the absorption and fluorescence processes, which is certainly the ultimate goal in all spectroscopic analyses, but is not yet always feasible because of limited technical and observational resources. We find that some open questions regarding the structure and geometry of the absorber that have been actively debated in the literature since the discovery of the source are possibly resolved by an iron-rich dust absorber accounting for most of the X-ray absorption but also fluorescence. This picture reconciles X-ray and IR observations, but also provides a consistent description of the X-ray absorption edges and fluorescence lines. Furthermore, a dust absorber is likely going to have a different electron-to-metals ratio compared to gas absorbers with typical cosmic abundances, therefore causing different deformation of the fluorescence lines due to Compton scattering. With these results shedding new light on this extraordinary X-ray binary, many open questions still remain: What is the chemical composition and structure of the dust? Does dust in binaries show similar properties as dust in the ISM? How does dust form and survive under these extreme conditions? Traditionally, dust signatures are studied by means of X-ray absorption fine structure modulations around atomic absorption edges, typically the Si K-edge at ∼1.8 keV, or the Fe L-edge around ∼0.7 keV because these can be observed with excellent spectral resolution with current grating spectrometers. However,

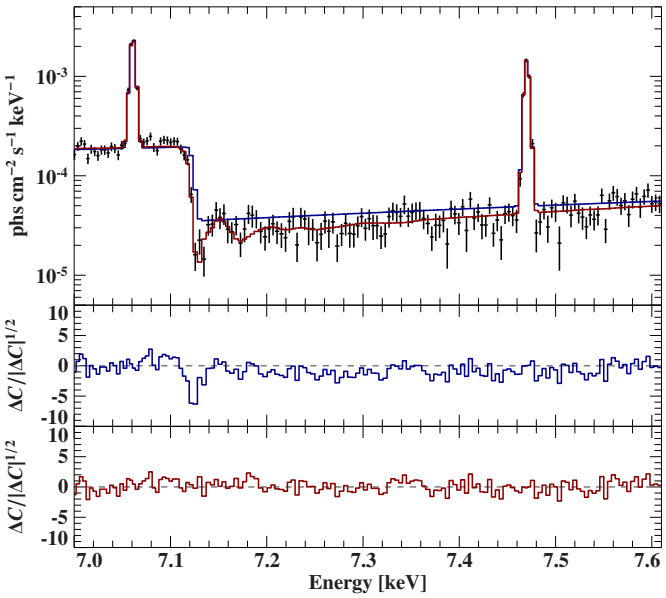

Fig. 7.1: Simulation of a 500 ks *XRISM*/Resolve observation of IGR J16318−4848 based on the spectral model and parameters of Table 5.2. The blue and red residuals correspond to the fit with a pure gas and olivine dust absorber, respectively. The *Hitomi* observation shown in Fig. 5.2, which resolved the Fe K emission lines, was acquired in ∼70 ks with an off-axis pointing of 5′.

in IGR J16318−4848, neither of these features are accessible because of the strong absorption that barely yields any signal below 3 keV.

The outstanding energy resolution of micro-calorimeter observatories has already been demonstrated by *Hitomi*. The upcoming launches of *XRISM* (XRISM Science Team 2020) in 2022 and *Athena* (Nandra et al. 2013, Meidinger et al. 2018, Barret et al. 2018) in the early 2030s will reveal a completely new perspective on atomic processes in many different kinds of X-ray sources. With an expected energy resolution of 5–7 eV, the Resolve instrument onboard *XRISM* will also be able to resolve X-ray absorption fine structure (XAFS) around the Fe K-edge (see, e.g., Lee et al. 2009, for a study of the capabilities of the micro-calorimeter instrument onboard *Suzaku* regarding XAFS), so we may expect constraints on dust composition and crystalline structure, not only in IGR J16318−4848 but also in other X-ray binaries and obscured AGN over the next couple of years. For illustration, Fig. 7.1 shows a simulation of 500 ks observation of IGR J16318−4848 based on the results presented in Chapter 5. The XAFS specific to crystalline olivine is clearly resolved, although requiring higher exposure times than previous observations at CCD resolution.

Future micro-calorimeter missions will also be capable of resolving the Heα triplet of Fe xxv, including the splitting of the intercombination line ($^3P_1$ and $^3P_2$), as was impressively demonstrated by *Hitomi*. Figure 7.2 shows simulation of a 50 ks *XRISM* observation of the Fe xxv Heα triplet for the line and continuum fluxes of Her X-1 Obs. IV which again illustrates the resolving power of *XRISM*. Line ratios of the He-like iron triplets will allow for complementary diagnostics, because the collisional excitation or di-electronic recombination via the resonant transition require much higher plasma temperatures compared to low-Z elements, e.g., N, O, and Ne. Hence, the

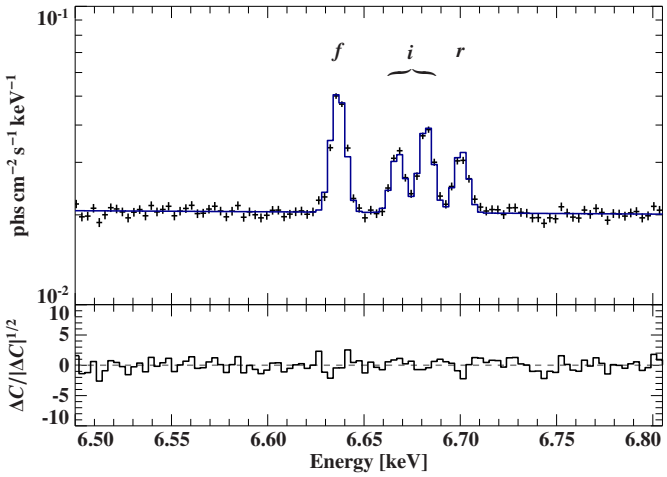

Fig. 7.2: Simulation of a 50 ks *XRISM* observation of the Fe xxv He α triplet for the spectral parameters of Her X-1 Obs. IV. Since this complex could not be resolved yet the simulation assumes $G = 4$ and $R = 1$. Note that this simulation does not account for possible pile-up.

G ratio is sensitive to a temperature range above 10^7 K. While this is an additional powerful temperature diagnostic in general, the interpretation of G in Her X-1 will still be ambiguous because of resonant scattering effects induced by the asymmetric plasma geometry. The separation of the $^3P_{1,2}$ and $^3S_1$ states is ~30 eV in Fe xxv, making R less susceptible to UV photoexcitation.

Her X-1 has an almost fifty year long history of X-ray observations with almost every X-ray satellite. Yet, the Time Allocation Committee of *XMM*-Newton alone awarded again a total of 380 ks – so more than four days – of exposure time in AO19, performed in 2020 August to study the vertical structure of disk winds in Her X-1, acknowledging the scientific value of this famous source. Apart from the continuous completion of the data archive with current X-ray missions and the new complementary observational perspectives we may expect from future observatories like *XRISM*, long-term modeling efforts will have to focus on the construction of self-consistent plasma models of the accretion disk, its atmosphere and its corona. Foundations of such a comprehensive model are already outlined by Jimenez-Garate et al. (2002b). Powerful photoionization and collisional ionization models are already available and successfully applied to astrophysical systems of sufficiently spherical symmetry. On the other hand, geometrical effects of reprocessing of X-ray radiation by an ionized medium have been, and are still, extensively studied in the context of accretion disk reflection, mostly in AGN and black hole binaries. These techniques provide the tools to study ionization processes, structure and geometry in Her X-1 and many other X-ray binaries. Although the construction of such advanced models and comparison to observational data is by its nature highly challenging, with the joint effort of observers and modelers, the future looks very bright in X-rays!

A

Abundance tables

Table A.1: Relative XSTAR abundances as used in version 2.53. For comparison, also other abundance tables used by common X-ray spectral analysis packages are listed.

Element	XSTAR	Grevesse et al. (1996)	Wilms et al. (2000)	Lodders & Palme (2009)
H	$\mathbf{1.00 \times 10^{+00}}$	$1.00 \times 10^{+00}$	$1.00 \times 10^{+00}$	$1.00 \times 10^{+00}$
He	$\mathbf{1.00 \times 10^{-01}}$	9.77×10^{-02}	9.77×10^{-02}	8.51×10^{-02}
Li	$\mathbf{1.00 \times 10^{-10}}$	1.45×10^{-11}	$0.00 \times 10^{+00}$	1.91×10^{-09}
Be	$\mathbf{1.00 \times 10^{-10}}$	1.41×10^{-11}	$0.00 \times 10^{+00}$	2.09×10^{-11}
B	$\mathbf{1.00 \times 10^{-10}}$	3.98×10^{-10}	$0.00 \times 10^{+00}$	6.46×10^{-10}
C	$\mathbf{3.70 \times 10^{-04}}$	3.55×10^{-04}	2.40×10^{-04}	2.45×10^{-04}
N	$\mathbf{1.10 \times 10^{-04}}$	9.33×10^{-05}	7.59×10^{-05}	7.24×10^{-05}
O	$\mathbf{6.80 \times 10^{-04}}$	7.41×10^{-04}	4.90×10^{-04}	5.37×10^{-04}
F	$\mathbf{3.98 \times 10^{-08}}$	3.63×10^{-08}	$0.00 \times 10^{+00}$	2.75×10^{-08}
Ne	$\mathbf{2.80 \times 10^{-05}}$	1.20×10^{-04}	8.71×10^{-05}	1.12×10^{-04}
Na	$\mathbf{1.78 \times 10^{-06}}$	2.14×10^{-06}	1.45×10^{-06}	1.95×10^{-06}
Mg	$\mathbf{3.50 \times 10^{-05}}$	3.80×10^{-05}	2.51×10^{-05}	3.47×10^{-05}
Al	$\mathbf{2.45 \times 10^{-06}}$	2.95×10^{-06}	2.14×10^{-06}	2.88×10^{-06}
Si	$\mathbf{3.50 \times 10^{-05}}$	3.55×10^{-05}	1.86×10^{-05}	3.39×10^{-05}
P	$\mathbf{3.31 \times 10^{-07}}$	2.82×10^{-07}	2.63×10^{-07}	2.82×10^{-07}
S	$\mathbf{1.60 \times 10^{-05}}$	2.14×10^{-05}	1.23×10^{-05}	1.45×10^{-05}
Cl	$\mathbf{3.98 \times 10^{-07}}$	3.16×10^{-07}	1.32×10^{-07}	1.78×10^{-07}
Ar	$\mathbf{4.50 \times 10^{-06}}$	3.31×10^{-06}	2.57×10^{-06}	3.16×10^{-06}
K	$\mathbf{8.91 \times 10^{-08}}$	1.32×10^{-07}	$0.00 \times 10^{+00}$	1.29×10^{-07}
Ca	$\mathbf{2.10 \times 10^{-06}}$	2.29×10^{-06}	1.58×10^{-06}	2.04×10^{-06}
Sc	$\mathbf{1.66 \times 10^{-09}}$	1.48×10^{-09}	$0.00 \times 10^{+00}$	1.17×10^{-09}
Ti	$\mathbf{1.35 \times 10^{-07}}$	1.05×10^{-07}	6.46×10^{-08}	8.51×10^{-08}
V	$\mathbf{2.51 \times 10^{-08}}$	1.00×10^{-08}	$0.00 \times 10^{+00}$	9.77×10^{-09}
Cr	$\mathbf{7.08 \times 10^{-07}}$	4.68×10^{-07}	3.24×10^{-07}	4.47×10^{-07}
Mn	$\mathbf{2.51 \times 10^{-07}}$	2.45×10^{-07}	2.19×10^{-07}	3.16×10^{-07}
Fe	$\mathbf{2.50 \times 10^{-05}}$	3.16×10^{-05}	2.69×10^{-05}	2.88×10^{-05}
Co	$\mathbf{1.26 \times 10^{-07}}$	8.32×10^{-08}	8.32×10^{-08}	7.94×10^{-08}
Ni	$\mathbf{2.00 \times 10^{-06}}$	1.78×10^{-06}	1.12×10^{-06}	1.66×10^{-06}
Cu	$\mathbf{3.16 \times 10^{-08}}$	1.62×10^{-08}	$0.00 \times 10^{+00}$	1.86×10^{-08}
Zn	$\mathbf{1.58 \times 10^{-08}}$	3.98×10^{-08}	$0.00 \times 10^{+00}$	4.47×10^{-08}

B

Light curves and Good Time Intervals of *XMM*-Newton Obs. I–IV

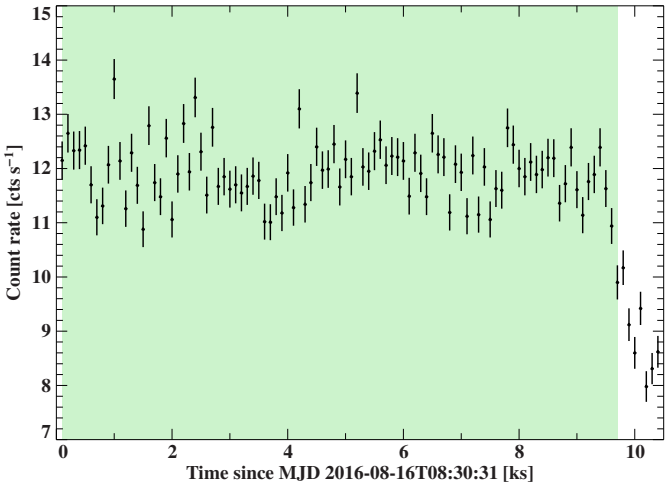

Fig. B.1: *XMM*-Newton EPIC-pn light curve of Obs. I. The green shaded region marks the time interval used for the spectral analysis in Chapter 6.

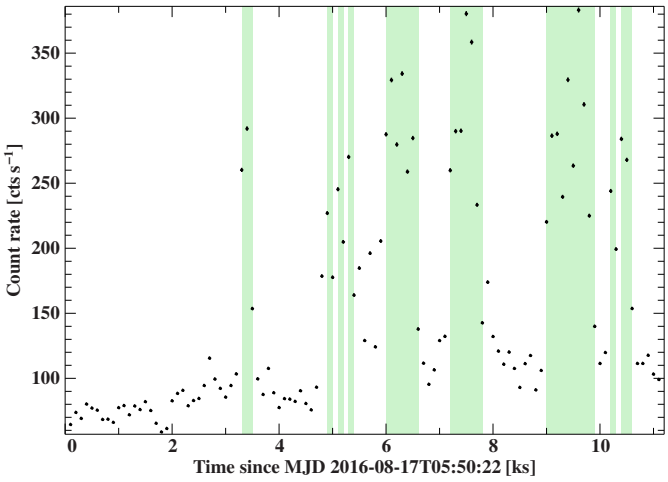

Fig. B.2: *XMM*-Newton EPIC-pn light curve of Obs. II. The green shaded region marks the time interval used for the spectral analysis in Chapter 6.

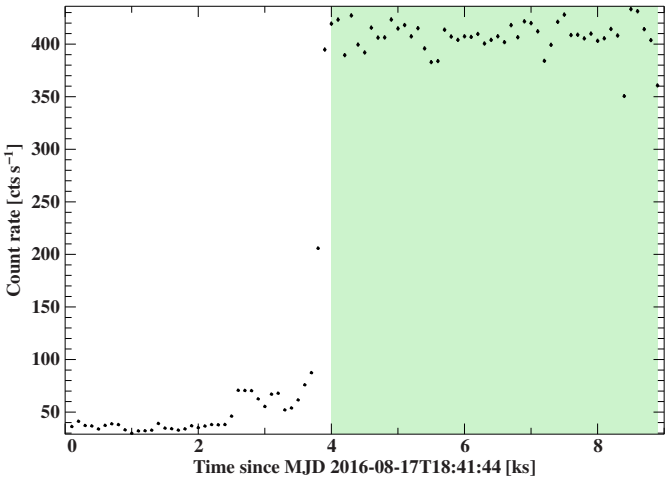

Fig. B.3: *XMM*-Newton EPIC-pn light curve of Obs. III. The green shaded region marks the time interval used for the spectral analysis in Chapter 6.

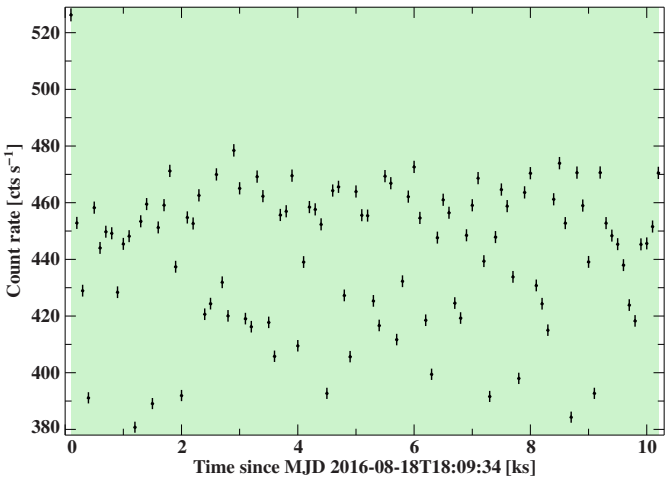

Fig. B.4: *XMM*-Newton EPIC-pn light curve of Obs. IV. The green shaded region marks the time interval used for the spectral analysis in Chapter 6.

References

Anderson S.F., Wachter S., Margon B., et al., 1994, ApJ 436, 319

Annuar A., Alexander D.M., Gandhi P., et al., 2020, MNRAS 497, 229

Arévalo P., Bauer F.E., Puccetti S., et al., 2014, ApJ 791, 81

Asami F., Enoto T., Iwakiri W., et al., 2014, PASJ 66, 44

Asplund M., Grevesse N., Sauval A.J., Scott P., 2009, ARA&A 47, 481

Auger P., 1926, Annales de Physique 10, 183

Bachetti M., Harrison F.A., Cook R., et al., 2015, ApJ 800, 109

Bachetti M., Huppenkothen D., 2018, ApJ 853, L21

Bachetti M., Rana V., Walton D.J., et al., 2013, ApJ 778, 163

Ballhausen R., Lorenz M., Fürst F., et al., 2020, A&A 641, A65

Ballhausen R., Pottschmidt K., Fürst F., et al., 2017, A&A 608, A105

Bambynek W., Crasemann B., Fink R.W., et al., 1972, Rev. Mod. Phys. 44, 716

Barragán L., Wilms J., Kreykenbohm I., et al., 2010a, In: 8th INTEGRAL Workshop "The Restless Gamma-ray Univers". PoS (INTEGRAL 2010), p. 135

Barragán L., Wilms J., Pottschmidt K., et al., 2010b, In: Comastri A., Cappi M., Angelini L. (eds.) X-ray Astronomy 2009: Present Status, Multi-Wavelength Approach and Future Perspectives. AIP Conf. Ser. 1248, p. 139

Barragán L., Wilms J., Pottschmidt K., et al., 2009, A&A 508, 1275

Barret D., Lam Trong T., den Herder J.W., et al., 2018, In: den Herder, J.-W., Nikzad, S., Nakazawa, K. (eds.) Space Telescopes and Instrumentation 2018: Ultraviolet to Gamma Ray, Proc. SPIE 10699, 1G

Basko M.M., Sunyaev R.A., 1975, A&A 42, 311

Bates D.R., Dalgarno A., 1962, Electronic Recombination. In: Bates D.R. (ed.) Atomic and Molecular Processes, Vol. 13. Academic Press, Inc., New York, p.245

Baum W.A., Johnson F.S., Oberly J.J., et al., 1946, Phys. Rev. 70, 781

Bearden J.A., 1967, Rev. Mod. Phys. 39, 78

Becker P.A., Wolff M.T., 2007, ApJ 654, 435

Bethell T.J., Bergin E.A., 2011, ApJ 740, 7

Bhalerao V., 2012, Ph.D. thesis, California Institute of Technology

Bildsten L., 2000, In: Holt S.S., Zhang W.W. (eds.) COSMIC EXPLOSIONS: Tenth Astrophysics Conference. AIP Conf. Ser. 522, p.359

Blum J.L., Miller J.M., Fabian A.C., et al., 2009, ApJ 706, 60

Blumenthal G.R., Drake G.W.F., Tucker W.H., 1972, ApJ 172, 205

Boissay-Malaquin R., Danehkar A., Marshall H.L., Nowak M.A., 2019, ApJ 873, 29

Bolton C.T., 1972, Nature 235, 271

Bondi H., Hoyle F., 1944, MNRAS 104, 273

Boroson B., Blair W.P., Davidsen A.F., et al., 1997, ApJ 491, 903

Boroson B., Kallman T., Vrtilek S.D., et al., 2000, ApJ 529, 414

Bowyer S., Byram E.T., Chubb T.A., Friedman H., 1964, Science 146, 912

Briel U.G., Burwitz V., Dennerl K., et al., 2005, In: Siegmund O.H.W. (ed.) Proc. SPIE, Vol. 5898. Society of Photo-Optical Instrumentation Engineers (SPIE) Conference Series, p.194

Brightman M., Baloković M., Stern D., et al., 2015, ApJ 805, 41

Brinkman A., Aarts H., den Boggende A., et al., 1998, In: Science with XMM., p. 2

Cash W., 1979, ApJ 228, 939

Chantler C., 1995, J. Phys. Chem. Ref. Data 24, 71

Chantler C., 2000, J. Phys. Chem. Ref. Data 29, 597

Chaty S., Filliatre P., 2004, In: Schoenfelder V., Lichti G., Winkler C. (eds.) 5th INTEGRAL Workshop on the INTEGRAL Universe. ESA Special Publication 552, p. 365

Chaty S., Rahoui F., 2012, ApJ 751, 150

Clayton G.C., Wolff M.J., Sofia U.J., et al., 2003, ApJ 588, 871

Compton A.H., 1923, Physical Review 21, 483

Corrales L.R., García J., Wilms J., Baganoff F., 2016, MNRAS 458, 1345

Costantini E., Pinto C., Kaastra J.S., et al., 2012, A&A 539, A32

Courvoisier T.J.L., Walter R., Rodriguez J., et al., 2003, IAU Circ. 8063

Crampton D., Hutchings J.B., 1974, ApJ 191, 483

Dauser T., Falkner S., Lorenz M., et al., 2019, A&A 630, A66

Dauser T., Garcia J., Parker M.L., et al., 2014, MNRAS 444, L100

Dauser T., Garcia J., Wilms J., et al., 2013, MNRAS 430, 1694

Dauser T., Wilms J., Reynolds C.S., Brenneman L.W., 2010, MNRAS 409, 1534

D'Avanzo P., Campana S., Salafia O.S., et al., 2018, A&A 613, L1

Davis S.W., Laor A., 2011, ApJ 728, 98

Debnath D., Chakrabarti S.K., Nandi A., Mand al S., 2008, Bulletin of the Astronomical Society of India 36, 151

den Herder J.W., Brinkman A.C., Kahn S.M., et al., 2001, A&A 365, L7

Dershem E., Schein M., 1931, Phys. Rev. 37, 1238

Draine B.T., 2003a, ARA&A 41, 241

Draine B.T., 2003b, ApJ 598, 1026

Draine B.T., Lee H.M., 1984, ApJ 285, 89

Dwek E., 2016, ApJ 825, 136

Eckert D., Jauzac M., Shan H., et al., 2015, Nature 528, 105

Edgar R., 2004, New A Rev. 48, 843

El Mellah I., Sundqvist J.O., Keppens R., 2018, MNRAS 475, 3240

Endo T., Nagase F., Mihara T., 2000, Publications of the Astronomical Society of Japan 52, 223

Fabian A.C., Rees M.J., Stella L., White N.E., 1989, MNRAS 238, 729

Fender R.P., Belloni T.M., Gallo E., 2004, MNRAS 355, 1105

Fender R.P., Homan J., Belloni T.M., 2009, MNRAS 396, 1370

Ferland G.J., Chatzikos M., Guzmán F., et al., 2017, Rev. Mexicana Astron. Astrofis. 53, 385

Filliatre P., Chaty S., 2004, ApJ 616, 469

Fireman E.L., 1974, ApJ 187, 57

Foreman-Mackey D., Hogg D.W., Lang D., Goodman J., 2013, PASP 125, 306

Fortin F., Chaty S., Sander A., 2020, ApJ 894, 86

Foschini L., Rodriguez J., Walter R., 2003, IAU Circ. 8076

Foulkes S.B., Haswell C.A., Murray J.R., 2010, MNRAS 401, 1275

Frank J., King A., Raine D., 2002, Accretion Power in Astrophysics, Cambridge University Press, Cambridge, 3rd edition

Friedman H., 1959, J. Geophys. Res. 64, 1751

Friedrich P., 2008, The Universe in X-Rays, Ch. 6, p.41, Springer-Verlag Berlin Heidelberg

Fürst F., Grefenstette B.W., Staubert R., et al., 2013, ApJ 779, 69

Fürst F., Pottschmidt K., Wilms J., et al., 2014, ApJ 780, 133

Gabriel A.H., Jordan C., 1969a, MNRAS 145, 241

Gabriel A.H., Jordan C., 1969b, Nature 221, 947

Gabriel A.H., Jordan C., 1970, Physics Letters A 32, 166

Galloway D.K., Muno M.P., Hartman J.M., et al., 2008, ApJS 179, 360

García J., Dauser T., Lohfink A., et al., 2014, ApJ 782, 76

García J., Dauser T., Reynolds C.S., et al., 2013, ApJ 768, 146

García J., Kallman T.R., 2010, ApJ 718, 695

García J., Kallman T.R., Mushotzky R.F., 2011, ApJ 731, 131

García J.A., Tomsick J.A., Sridhar N., et al., 2019, ApJ 885, 48

George I.M., Fabian A.C., 1991, MNRAS 249, 352

Gerend D., Boynton P.E., 1976, ApJ 209, 562

Giacconi R., Gursky H., Kellogg E., et al., 1971, ApJ 167, L67

Giacconi R., Gursky H., Paolini F.R., Rossi B.B., 1962, Phys. Rev. Lett. 9, 439

Glasser C.A., Odell C.E., Seufert S.E., 1994, IEEE Transactions on Nuclear Science 41, 1343

Goodman J., Weare J., 2010, Comm. Appl. Math. Comp. Sci. 5, 65

Grevesse N., Noels A., Sauval A.J., 1996, In: Holt S.S., Sonneborn G. (eds.) Cosmic Abundances, Vol. 99. ASP Conf. Ser., p. 117

Grinberg V., Hell N., El Mellah I., et al., 2017, A&A 608, A143

Gruzinov A.V., 1998, ApJ 501, 787

Halpern J.P., Grindlay J.E., 1980, ApJ 242, 1041

Han I., Demir L., 2009, Phys. Rev. A 80, 052503

Hanke M., 2011, Ph.D. thesis, Universität Erlangen-Nürnberg

Harrison F.A., Craig W.W., Christensen F.E., et al., 2013, ApJ 770, 103

Heintz W.D., 1978, Double stars, Vol. 15, D. Reidel Publishing Company

Heinz S., Corrales L., Smith R., et al., 2016, ApJ 825, 15

Hewlett C.W., 1921, Phys. Rev. 17, 284

Hiemstra B., Méndez M., Done C., et al., 2011, MNRAS 411, 137

Hikitani M., Ohno M., Fukazawa Y., et al., 2018, ApJ 867, 80

Hilditch R.W., 2001, An Introduction to Close Binary Stars, Cambridge University Press, Cambridge

Hirsch M., 2019, Ph.D. thesis, Friedrich-Alexander-Universität Erlangen-Nürnberg (FAU)

Hirsch M., Hell N., Grinberg V., et al., 2019, A&A 626, A64

Hitomi Collaboration 2016, Nature 535, 117

Hitomi Collaboration 2018, PASJ 70, 17

Hoffman J., Draine B.T., 2016, ApJ 817, 139

Houck J.C., Denicola L.A., 2000, In: Manset N., Veillet C., Crabtree D. (eds.) Astronomical Data Analysis Software and Systems IX, Vol. 216. ASP Conf. Ser., p. 591

Hoyle F., Lyttleton R.A., 1939, Proceedings of the Cambridge Philosophical Society 35, 405

Hubbell J., 2006, Physics in Medicine and Biology 51, R245

Hubbell J., Øverbø I., 1979, Journal of Physical and Chemical Reference Data 8, 69

Hubbell J.H., Trehan P.N., Singh N., et al., 1994, Journal of Physical and Chemical Reference Data 23, 339

Hubbell J.H., Veigele W.J., Briggs E.A., et al., 1975, Journal of Physical and Chemical Reference Data 4, 471

Ibarra A., Matt G., Guainazzi M., et al., 2007, A&A 465, 501

Icke V., 1976, In: Eggleton P., Mitton S., Whelan J. (eds.) Structure and Evolution of Close Binary Systems, Vol. 73., p. 267

Israel G.L., Papitto A., Esposito P., et al., 2017, MNRAS 466, L48

Iyer N., Paul B., 2017, MNRAS 471, 355

Jacobs V.L., Davis J., Rogerson J.E., Blaha M., 1979, ApJ 230, 627

Janesick J., 2001, Scientific Charge-coupled Devices, Press Monograph Series, SPIE Press, Bellingham, Washington

Jansen F., Lumb D., Altieri B., et al., 2001, A&A 365, L1

Jethwa P., Saxton R., Guainazzi M., et al., 2015, A&A 581, A104

Ji L., Schulz N., Nowak M., et al., 2009, ApJ 700, 977

Jimenez-Garate M.A., Hailey C.J., den Herder J.W., et al., 2002a, ApJ 578, 391

Jimenez-Garate M.A., Raymond J.C., Liedahl D.A., 2002b, ApJ 581, 1297

Jimenez-Garate M.A., Raymond J.C., Liedahl D.A., Hailey C.J., 2005, ApJ 625, 931

Kaastra J.S., Bleeker J.A.M., 2016, A&A 587, A151

Kallman T., Bautista M., 2001, ApJS 133, 221

Kane P.P., Kissel L., Pratt R.H., Roy S.C., 1986 140, 75

King A.L., Miller J.M., Raymond J., et al., 2015, ApJ 813, L37

Kitaguchi T., Grefenstette B.W., Harrison F.A., et al., 2011, In: Siegmund O.H. (ed.) UV, X-Ray, and Gamma-Ray Space Instrumentation for Astronomy XVII, Proc. SPIE 8145, 79

Klein O., Nishina T., 1929, Zeitschrift für Physik 52, 853

Klochkov D., Staubert R., Postnov K., et al., 2008, A&A 482, 907

Knoll G.F., 2000, Radiation Detection and Measurement, John Wiley & Sons, Inc., New York/Chichester/Weinheim/Brisbane/Toronto/Singapore

Ko Y.K., Kallman T.R., 1991, ApJ 374, 721

Ko Y.K., Kallman T.R., 1994, ApJ 431, 273

Kosec P., Fabian A.C., Pinto C., et al., 2020, MNRAS 491, 3730

Kreikenbohm A., 2013, *Master's thesis*, Universität Würzburg

Krimm H.A., Holland S.T., Corbet R.H.D., et al., 2013, ApJS 209, 14

Kurtz H., 1928, Annalen der Physik 390, 529

Kuster M., Wilms J., Staubert R., et al., 2005, A&A 443, 753

Lansbury G.B., Alexander D.M., Aird J., et al., 2017, ApJ 846, 20

Leahy D.A., 2002, MNRAS 334, 847

Leahy D.A., Creighton J., 1993, MNRAS 263, 314

Leahy D.A., Darbro W., Elsner R.F., et al., 1983, ApJ 266, 160

Leahy D.A., Igna C.D., 2010, ApJ 713, 318

Lee J.C., Ravel B., 2005, ApJ 622, 970

Lee J.C., Xiang J., Ravel B., et al., 2009, ApJ 702, 970

Lee J.C., Xiang J., Ravel B., et al., 2009, ApJ 702, 970

Levich E.V., Syunyaev R.A., 1971, Soviet Ast. 15, 363

Liedahl D.A., 1999, The X-Ray Spectral Properties of Photoionized Plasma and Transient Plasmas, Vol. 520, p. 189

Liedahl D.A., Paerels F., 1996, ApJ 468, L33

Lin D., Strader J., Carrasco E.R., et al., 2018, Nature Astronomy 2, 656

Lodders K., Palme H., 2009, Meteoritics and Planetary Science Supplement 72, 5154

Lyubarskii Y.É., 1986, Astrophysics 25, 577

Madsen K.K., Harrison F.A., Markwardt C.B., et al., 2015, ApJS 220, 8

Magdziarz P., Zdziarski A.A., 1995, MNRAS 273, 837

Maloney P.R., Begelman M.C., 1997, ApJ 491, L43

Manousakis A., 2011, Ph.D. thesis, University of Geneva ID: unige:18752

Martínez-Núñez S., Kretschmar P., Bozzo E., et al., 2017, Space Sci. Rev. 212, 59

Mason K.O., Breeveld A., Much R., et al., 2001, A&A 365, L36

Mathis J.S., Rumpl W., Nordsieck K.H., 1977, ApJ 217, 425

Matt G., 2002, MNRAS 337, 147

Matt G., Guainazzi M., 2003, MNRAS 341, L13

McCray R.A., Shull J.M., Boynton P.E., et al., 1982, ApJ 262, 301

Meidinger N., Nandra K., Plattner M., 2018, In: den Herder, J.-W., Nikzad, S., Nakazawa, K. (eds.) Space Telescopes and Instrumentation 2018: Ultraviolet to Gamma Ray, Proc. SPIE 10699, 312

Meitner L., 1922, Zeitschrift für Physik 9, 131

Mewe R., 1999, Atomic Physics of Hot Plasmas, Vol. 520, p. 109

Mewe R., Schrijver J., 1978a, A&A 65, 99

Mewe R., Schrijver J., 1978b, A&A 65, 115

Mewe R., Schrijver J., 1978c, A&AS 33, 311

Meyer F., Meyer-Hofmeister E., 1982, A&A 106, 34

Mihalas D., 1978, Stellar atmospheres, W. H. Freeman, San Francisco, 2nd edition

Mihara T., 1995, Ph.D. thesis, Univerity of Tokyo

Miller J.M., Fabian A.C., Reynolds C.S., et al., 2004, ApJ 606, L131

Miller J.M., Parker M.L., Fürst F., et al., 2013, ApJ 775, L45

Milne E.A., 1924, Philosophical Magazine 47, 209

Moon D.S., Kaplan D.L., Reach W.T., et al., 2007, ApJ 671, L53

Müller E.A.W., 1935, ZAp 10, 52

Murakami H., Dotani T., Wijnands R., 2003, IAU Circ. 8070

Nagase F., Hayakawa S., Sato N., et al., 1986, PASJ 38, 547

Nandra K., Barret D., Barcons X., et al., 2013, arXiv e-prints arXiv:1306.2307

Nandra K., O'Neill P.M., George I.M., Reeves J.N., 2007, MNRAS 382, 194

Nelms A.T., Oppenheim I., 1955, J. Res. Natl. Bur. Stand. 55, 53

Ness J.U., Schmitt J.H.M.M., Burwitz V., et al., 2002, A&A 394, 911

Niemela V., 2001, In: Revista Mexicana de Astronomia y Astrofisica Conference Series, Vol. 11., p.23

Nozawa T., Fukugita M., 2013, ApJ 770, 27

Oda M., Gorenstein P., Gursky H., et al., 1971, ApJ 166, L1

Odaka H., Yoneda H., Takahashi T., Fabian A., 2016, MNRAS 462, 2366

Oosterbroek T., Parmar A.N., Dal Fiume D., et al., 2000, A&A 353, 575

Oosterbroek T., Parmar A.N., Martin D.D.E., Lammers U., 1997, A&A 327, 215

Osterbrock D.E., 1989, Astrophysics of gaseous nebulae and active galactic nuclei, University Science Books, Mill Valley, California

Petterson J.A., 1977a, ApJ 218, 783

Petterson J.A., 1977b, ApJ 214, 550

Petterson J.A., 1977c, ApJ 216, 827

Pinto C., Kaastra J.S., Costantini E., de Vries C., 2013, A&A 551, A25

Pinto C., Middleton M.J., Fabian A.C., 2016, Nature 533, 64

Pintore F., Tiengo A., Mereghetti S., et al., 2017, MNRAS 472, 1465

Porquet D., Dubau J., 2000, A&AS 143, 495

Porquet D., Mewe R., Dubau J., et al., 2001, A&A 376, 1113

Postnov K.A., Gornostaev M.I., Klochkov D., et al., 2015, MNRAS 452, 1601

Pringle J.E., 1981, ARA&A 19, 137

Protassov R., van Dyk D.A., Connors A., et al., 2002, ApJ 571, 545

Psaradaki I., Costantini E., Mehdipour M., et al., 2020, A&A 642, A208

Ramsay G., Zane S., Jimenez-Garate M.A., et al., 2002, MNRAS 337, 1185

Raymond J.C., 1993, ApJ 412, 267

Rea N., Esposito P., Turolla R., et al., 2010, Science 330, 944

Reed S.J.B., Ware N.G., 1972, Journal of Physics E: Scientific Instruments 5, 582

Rehr J.J., Albers R.C., 2000, Rev. Mod. Phys. 72, 621

Reig P., 2011, Ap&SS 332, 1

Remillard R.A., McClintock J.E., 2006, ARA&A 44, 49

Reynolds A.P., Quaintrell H., Still M.D., et al., 1997, MNRAS 288, 43

Ricci C., Bauer F.E., Treister E., et al., 2016, ApJ 819, 4

Rogantini D., Costantini E., Zeegers S.T., et al., 2018, A&A 609, A22

Röntgen W.C., 1895, Aus den Sitzungsberichten der Würzburger Physik.-medic. Gesellschaft Würzburg 137–147

Röntgen W.C., 1896, Aus den Sitzungsberichten der Würzburger Physik.-medic. Gesellschaft Würzburg 12–17

Röntgen W.C., 1897, Aus den Sitzungsber. der k. preuss. Akad. der Wissensch. zu Berlin 18–37

Ross R.R., Fabian A.C., 1993, MNRAS 261, 74

Ross R.R., Fabian A.C., 2005, MNRAS 358, 211

Ross R.R., Fabian A.C., Young A.J., 1999, MNRAS 306, 461

Rutledge R.E., Bildsten L., Brown E.F., et al., 1999, ApJ 514, 945

Rybicki G.B., Lightman A.P., 1986, Radiative Processes in Astrophysics, John Wiley & Sons, Inc., New York/Chichester/Weinheim/Brisbane/Toronto/Singapore

Sako M., Kahn S.M., Behar E., et al., 2001, A&A 365, L168

Scargle J.D., Norris J.P., Jackson B., Chiang J., 2013, ApJ 764, 167

Schandl S., 1996, A&A 307, 95

Schandl S., Meyer F., 1994, A&A 289, 149

Schreier E., Giacconi R., Gursky H., et al., 1972a, ApJ 178, L71

Schreier E., Gursky H., Kellogg E., et al., 1971, ApJ 170, L21

Schreier E., Levinson R., Gursky H., et al., 1972b, ApJ 172, L79

Schulz N.S., Huenemoerder D.P., Ji L., et al., 2009, ApJ 692, L80

Scott D.M., Leahy D.A., 1999, ApJ 510, 974

Scott D.M., Leahy D.A., Wilson R.B., 2000, ApJ 539, 392

Sguera V., Tiengo A., Sidoli L., Bird A.J., 2020, ApJ 900, 22

Shakura N.I., Postnov K.A., Kochetkova A.Y., et al., 2015, Astronomy Reports 59, 645

Shakura N.I., Prokhorov M.E., Postnov K.A., Ketsaris N.A., 1999, A&A 348, 917

Shakura N.I., Sunyaev R.A., 1973, A&A 500, 33

Shapiro P.R., Moore R.T., 1977, ApJ 217, 621

Shapiro S.L., Lightman A.P., Eardley D.M., 1976, ApJ 204, 187

Shklovsky I.S., 1967, ApJ 148, L1

Shore B.W., 1969, ApJ 158, 1205

Smith R.K., Brickhouse N.S., Liedahl D.A., Raymond J.C., 2001, ApJ 556, L91

Smith R.K., Valencic L.A., Corrales L., 2016, ApJ 818, 143

Spencer R.G., 1931, Phys. Rev. 38, 1932

Spruit H., 2014, Accretion disks. In: González Martínez-País I., Shahbaz T., Casares Velázquez J. (eds.) Accretion Processes in Astrophysics. XXI Canary Islands Winter School of Astrophysics. Cambridge University Press, Cambridge, p.1

Staelin D.H., Reifenstein, Edward C. I., 1968, Science 162, 1481

Staubert R., Kendziorra E., Pietsch W., et al., 1978, ApJ 225, L113

Staubert R., Klochkov D., Wilms J., 2009, A&A 500, 883

Stobbe M., 1930, Annalen der Physik 399, 661

Strüder L., Briel U., Dennerl K., et al., 2001, A&A 365, L18

Sunyaev R.A., Churazov E.M., 1996, Astronomy Letters 22, 648

Sunyaev R.A., Titarchuk L.G., 1980, A&A 500, 167

Tananbaum H., Gursky H., Kellogg E.M., et al., 1972, ApJ 174, L143

Tarter C.B., Tucker W.H., Salpeter E.E., 1969, ApJ 156, 943

Tashiro M., Maejima H., Toda K., et al., 2018, In: den Herder, J.-W., Nikzad, S., Nakazawa, K. (eds.) Space Telescopes and

Instrumentation 2018: Ultraviolet to Gamma Ray, Proc. SPIE 10699, 22

Tauris T.M., van den Heuvel E.P.J., 2006, Formation and evolution of compact stellar X-ray sources. In: Lewin W., van der Klis M. (eds.) Compact Stellar X-ray Sources. Cambridge University Press, Cambridge, Ch. 16, p.623

Thorne K.S., 1974, ApJ 191, 507

Tiengo A., Vianello G., Esposito P., et al., 2010, ApJ 710, 227

Titarchuk L., 1994, ApJ 434, 570

Trümper J., Pietsch W., Reppin C., et al., 1978, ApJ 219, L105

Tsygankov S.S., Doroshenko V., Mushtukov A.e.A., et al., 2019a, MNRAS 487, L30

Tsygankov S.S., Rouco Escorial A., Suleimanov V.F., et al., 2019b, MNRAS 483, L144

Turlione A., Aguilera D.N., Pons J.A., 2015, A&A 577, A5

Turner M.J.L., Abbey A., Arnaud M., et al., 2001, A&A 365, L27

Ubertini P., Lebrun F., Di Cocco G., et al., 2003, A&A 411, L131

Verner D.A., Ferland G.J., Korista K.T., Yakovlev D.G., 1996, ApJ 465, 487

Verner D.A., Yakovlev D.G., 1995 109, 125

Verner D.A., Yakovlev D.G., Band I.M., Trzhaskovskaya M.B., 1993, Atomic Data and Nuclear Data Tables 55, 233

Vrtilek S.D., Mihara T., Primini F.A., et al., 1994, ApJ 436, L9

Vuong M.H., Montmerle T., Grosso N., et al., 2003, A&A 408, 581

Vybornov V., Klochkov D., Gornostaev M., et al., 2017, A&A 601, A126

Walter R., Rodriguez J., Foschini L., et al., 2003, A&A 411, L427

Walton D.J., Fürst F., Heida M., et al., 2018, ApJ 856, 128

Waseda Y., Matsubara E., Shinoda K., 2011, X-Ray Diffraction Crystallography, Springer, Berlin, Heidelberg

Watanabe S., Sako M., Ishida M., et al., 2003, ApJ 597, L37

Weingartner J.C., Draine B.T., 2001, ApJ 548, 296

West B.F., Wolfram K.D., Becker P.A., 2017a, ApJ 835, 129

West B.F., Wolfram K.D., Becker P.A., 2017b, ApJ 835, 130

Westphal A.J., Butterworth A.L., Tomsick J.A., Gainsforth Z., 2019, ApJ 872, 66

White N.E., Becker R.H., Boldt E.A., et al., 1981, ApJ 247, 994

White N.E., Holt S.S., 1982, ApJ 257, 318

Wijers R.A.M.J., Pringle J.E., 1999, MNRAS 308, 207

Wijnands R., Degenaar N., Page D., 2017, Journal of Astrophysics and Astronomy 38, 49

Wik D.R., Hornstrup A., Molendi S., et al., 2014, ApJ 792, 48

Wilms J., Allen A., McCray R., 2000, ApJ 542, 914

Wilms J., Pottschmidt K., Pooley G.G., et al., 2007, ApJ 663, L97

Wilms J., Reynolds C.S., Begelman M.C., et al., 2001, MNRAS 328, L27

Winkler P.F., Clark G.W., Markert T.H., et al., 1981, ApJ 245, 574

Wojdowski P.S., Liedahl D.A., Sako M., et al., 2003, ApJ 582, 959

Wolff M.T., Becker P.A., Gottlieb A.M., et al., 2016, ApJ 831, 194

XRISM Science Team 2020, arXiv e-prints arXiv:2003.04962

Xu Y., Harrison F.A., García J.A., et al., 2018, ApJ 852, L34

Zeegers S.T., Costantini E., de Vries C.P., et al., 2017, A&A 599, A117

Zeegers S.T., Costantini E., Rogantini D., et al., 2019, A&A 627, A16

Ziolkowski J., 2002, Mem. Soc. Astron. Italiana 73, 1038

Acknowledgments

They say, roads were made for journeys, not for destinations. With this thesis and also a chapter of my life coming to an end I am now only left with thanking all the amazing people that helped and supported me along this way.

First and foremost I want to take this opportunity to thank Jörn Wilms for giving me the opportunity to do a PhD project in his group. I am particularly grateful for his sensitive balance between gentle pressure to finish papers and projects in time and the liberty to peruse own projects just out of interest and curiosity. I first met Jörn in his undergraduate lecture *X-ray astronomy I* in 2012, and rather ironically after the very hour he taught photoionization balance calculations, I walked up front and asked for a Bachelor's project, not at all imagining where this would lead to (although the Bachelor's project was on a completely different topic).

The Remeis observatory is a wonderful place to work, remote of the rest of the university and with people being more like family than colleagues. This unique atmosphere would never be possible without our directors Jörn Wilms, Manami Sasaki, and Uli Heber whose "management" of the observatory may be better described as parental care.

Without Edith Day I am afraid I would have tripped over contract extensions and missing "Betreuungsvereinbarungen" so a big thank you for steering my PhD around bureaucratic shoals.

A special thank you goes to the admins of the computing cluster of the observatory who invest uncountable hours, also on weekends and evenings, to keep servers and desktop machines running day and night, software up to date, or assist the more or less experienced user with their individual problems. In particular the people without whom the computing infrastructure would break down in no time are Ingo Kreykenbohm, Philipp Weber, Jakob Stierhof, Thomas Dauser, Jonathan Knies, Maximilian Lorenz and former members Matthias Kühnel and Fritz Schwarm.

Matthias Kühnel, Fritz Schwarm, and Sebastian Falkner were also the people who introduced me into X-ray data analysis, magnetized neutron stars in general and CRSF and pulse profile formation in particular and I owe a great deal of my fascination for these sources to them. I have also received tremendous scientific input from the XMAG collaboration. I want to thank Katja Pottschmidt for so many valuable discussions and feedback on data analysis questions and papers, but also for showing me around GSFC and inviting me to Thanksgiving dinner in 2016.

The people who actively work on X-ray binaries have always formed sub-group at the observatory, owing to the variety of research activities carried out here. I enjoyed many fruitful and productive discussions with Ekaterina Sokolova-Lapa, Philipp Thalhammer, Katrin Berger, and former members Matthias Kühnel, Sebastian Müller, Fritz Schwarm, Sebastian Falkner, and Maria Hirsch.

My experience in X-ray spectroscopy, dust physics and plamsa diagnostics has increased immensely by long lasting collaborations and extensive discussions with Maria Chicharro, Manuel Castro, Natalie Hell, Victoria Grinberg, Javier García and Lía Corrales. On this occasion, I also want to thank Maurice Leutenegger to let me join two of his beamtimes, once at BESSY II in Berlin and once at PETRA III to gain a completely new and fascinating insight in laboratory astrophysics.

I have now spent nearly five years in my office and many people came and went. Those who made the time there most enjoyable were Thorsten Brandt, Maria Hirsch, Stefan Lickleder, Alexander Reichel, and Dominic Bernreuther.

Over the past years, many of my colleagues have become close friends and I can look back at countless unforgettable moments, some of which belong to my fondest memories. Although this recollection is by no means complete I want to thank my dear friends Eugenia Fink for being the intelligence agency of the observatory, the initiative of buying the first ever swimming pool, organizing more parties than I can count and supplying me with her delicious homemade pastries, Eva Ziegerer for meaningful glances, movie nights, and heaps of candy, Mina Gräfe for many years of moral support, our motorcycle lessons, and picknicking on the Via Appia, Katya Sokolova-Lapa for tons of Italian antipasti, endless laughter about our first attempt to get on skis, and teaching me to order beer in Russian, Simon Kreuzer for his legendary brewery hiking trips, barbecues, and dubious game nights, Maximilian Lorenz for his expertise in excellent food, my first pool billard lesson, and the “brown challenge”, Jakob Stierhof for his never-ending patience in trying to teach me card game and an amazing roadtrip through Utah, Natalie Hell, a walking encyclopedia of atomic physics but also a great connaisseuse of board games, and Victoria Grinberg for many interesting discussions on stellar winds and black hole binaries, valuable advice regarding science and career but also for a funny day exploring multi-national food on the Wiener Naschmarkt.

A huge thank you from me and probably every other reader for taking the burden of proofreading this thesis goes to Mina Gräfe, Katya Sokolova-Lapa, Jakob Stierhof, Maximilian Lorenz, Simon Kreuzer & Amy Joyce.

Last but not least I want to thank my family and friends for their overwhelming and unfailing support all these years!